Development of red fluorescent protein-based calcium ion and glutamate indicators

by

Jiahui Wu

A thesis submitted in partial fulfillment of the requirements for the degree of

Doctor of Philosophy

Department of Chemistry
University of Alberta

Abstract

The discovery and subsequent applications of fluorescent proteins (FPs) launched a new era for live cell fluorescence imaging. The design and developments of FP-based indicators have further solidified the versatility of FPs and rendered them as indispensable tools in life science research now more than ever. Despite the tremendous developments and efforts invested in the field of FP-based indicators, there remain numerous opportunities in engineering indicators with improved or novel properties for studying biological processes *in vivo*. In this thesis we describe our efforts in developing a series of FP-based calcium ion (Ca^{2+}) and glutamate indicators with various colors and useful spectral properties as versatile tools for interrogating cell signaling in cell biology.

In this thesis, we first describe our efforts in employing protein engineering to expand the color palette of genetically encoded Ca^{2+} indicators to include intensiometric orange, improved red and ratiometric red fluorescent variants. We demonstrate these new indicators' utility by performing Ca^{2+} imaging in cultured human cell lines, slice culture of developing mouse neocortex, organotypic hippocampal slice cultures and the visual system of albino tadpoles.

Using our intensiometric red Ca^{2+} indicators, R-GECO1 and R-GECO1.2, as templates, we further engineered a series of low affinity R-GECOs with dissociation constants (K_ds) ranging from 12 μM to more than 540 μM. We demonstrate that these indicators can be used to image cell compartments with high Ca^{2+} concentration or with a broad range of Ca^{2+} change, such as the endoplasmic reticulum (ER) and mitochondria. We also demonstrate these new red Ca^{2+} indicators with low affinities can be used to monitor ER and

mitochondrial Ca^{2+} in combination with a green fluorescent protein (GFP)-based reporter.

We also report in this thesis the development, optimization and characterization of the first red fluorescent protein (RFP)-based glutamate indicator, GltR1. We demonstrate GltR1 can detect glutamate changes on the surface of cultured human cells, as well as the glutamate dynamics during spontaneous activities of dissociated rat hippocampal neurons.

Preface

In Chapter 1 of this thesis, Figures 1.7, 1.9, 1.11 and 1.13 were adapted from the following publication: S. C. Alford, J. Wu, Y. Zhao, R. E. Campbell, and T. Knöpfel, “Optogenetic reporters”. *Biol. Cell*., 105, 14–29 (2013).

Chapter 2 has been published as J. Wu, L. Liu, T. Matsuda, Y. Zhao, A. Rebane, M. Drobizhev, Y-F. Chang, S. Araki, Y. Arai, K. March, T. E. Hughes, K. Sagou, T. Miyata, T. Nagai, W-h. Li, R. E. Campbell, “Improved orange and red Ca^{2+} indicators and photophysical considerations for optogenetic applications”, *ACS Chem. Neurosci*., 4, 963–972 (2013). I performed directed evolution and the majority of the characterization of O-GECO1, R-GECO1.2 and CAR-GECO1. L.L. performed imaging and optogenetic activation in INS-1 cells. T. Matsuda and Y.-F.C. performed imaging and optogenetic activation in neurons. Y.Z. performed kinetic characterization. A.R. and M.D. acquired the 2-photon spectra. S.A. imaged Ca^{2+} dynamics in HeLa cells. Y.A. developed the microscope for optogenetic activation and imaging. K.M. and T.E.H. performed imaging and optogenetic activation with the short wavelength opsin. K.S. performed electroporation of mouse embryos. T. Miyata prepared brain slices from transfected mouse embryo and processed imaging data. R.E.C., W.-H.L, and T.N. directed research, devised experiments, and wrote the manuscript.

A version of Chapter 3 has been submitted for publication as J. Wu, A. S. Abdelfattah, L. S. Miraucourt, E. Kutsarova, A. Ruangkittisakul, H. Zhou, K. Ballanyi, G. Wicks, M. Drobizhev, A. Rebane, E. S. Ruthazer, and R. E. Campbell, “A long Stokes shift red fluorescent protein Ca^{2+} indicator for 2-photon and ratiometric imaging”. I performed rational design, directed evolution, the

majority of in vitro characterization and imaging in HeLa cells and dissociated neurons. A.S.A. performed culture, electroporation, field stimulation, 1-photon and 2-photon imaging of organotypic slices. E.K. performed imaging of Xenopus *ex vivo* brain preparation and L.S.M. performed *in vivo* imaging of visually evoked responses. A.R. performed rat hippocampus dissection and provided support regarding 1- and 2-photon imaging. H.Z. performed protein purification and measured extinction coefficient and quantum yield. G.W., M.D. and A.R. acquired the 2-photon spectra. R.E.C., K.B. and E.S.R. directed research, devised experiments. A.S.A., E.S.R., R.E.C. and I wrote the manuscript.

A version of Chapter 4 has been accepted for publication as J. Wu, D. L. Prole, Y. Shen, Z. Lin, A. Gnanasekaran, Y. Liu, L. Chen, H. Zhou, S. R. W. Chen, Y. M. Usachev, C. W. Taylor and R. E. Campbell, "Red fluorescent genetically encoded Ca^{2+} indicators for use in mitochondria and endoplasmic reticulum", *Biochem. J.* Immediate Publication, doi:10.1042/BJ20140931, (2014). I was responsible for the rational design of LAR-GECO1 and 1.2, directed evolution of LAR-GECO1.2 and HeLa cells imaging of ER-LAR-GECO1 and GCaMP3. D.L.P. performed imaging of ER-LAR-GECO1 in conjunction with ER-GFP, CatchER, ER-GAP1 and Cyto-G-GECO1.1. Y.S performed directed evolution of LAR-GECO1. Z.L. and A.G. carried out simultaneous measurements of cytosolic and mitochondrial Ca^{2+} in neurons. Y.L. performed imaging of LAR-GECO1 and D1ER in HEK-293 cells. L.C. and H.Z. performed protein purification and in vitro characterization. R.E.C., Y.M.U., D.L.P., C.W.T., S.R.W.C. and I directed research and devised experiments. D.L.P., Y.M.U., C.W.T, R.E.C. and I wrote the manuscript.

Table of Contents

Abstract ii
Preface iv
List of Tables x
List of Figures xi
List of Abbreviations xiv
Chapter 1 General introduction 1
1.1 Overview and premise 2
1.2 Fluorescent proteins 4
1.2.1 Natural sources 4
1.2.2 Primary sequence and three-dimensional structure 5
1.2.3 Chromophore formation 6
1.2.4 Engineered FP variants 10
1.2.4.1 Engineered FPs with fast folding and maturation 11
1.2.4.2 Engineered FPs with monomeric property 11
1.2.4.3 Engineered FPs with different hues 13
1.2.4.4 Engineered FPs with other favorable or novel properties 17
1.2.5 Applications of FPs 17
1.3 Genetically encoded FP-based biosensors 18
1.3.1 FRET-based biosensors 19
1.3.2 Single FP-based biosensors 22
1.3.3 BiFC-based biosensors 26
1.4 Protein engineering 28
1.5 The scope of the thesis 31
Chapter 2 Development of orange and red Ca^{2+} indicators 34
2.1 Introduction 35
2.2 Results and discussion 37
2.2.1 Directed evolution of red Ca^{2+} indicators 37
2.2.2 Development of improved orange and red Ca^{2+} indicators 38
2.2.3 *In vitro* characterization 42
2.2.4 Characterization in live cells 44
2.2.5 Photoactivation in orange and red Ca^{2+} indicators 46

2.2.6 Characterization of photoactivation 53
2.2.7 A proposed model for photoactivation 61
2.3 Conclusion 64
2.4 Materials and methods 64
2.4.1 General methods and materials 64
2.4.2 Generation of improved GECOs variants 65
2.4.3 Screening of gene libraries 66
2.4.4 Characterization of orange and red Ca^{2+} indicators 67
2.4.5 *In vitro* characterization of photoactivation 70
2.4.6 Construction of mammalian expression plasmids 71
2.4.7 HeLa cell culture and imaging 72
2.4.8 Ca^{2+} imaging of R-GECO1.2 and ChR2 activation in INS-1 cells 73
2.4.9 Light driven Gq activation 74
2.4.10 Ca^{2+} imaging with ChR2 activation in mice brain slices 75
Chapter 3 Development of a long Stokes shift red fluorescent protein Ca^{2+} indicator for 2-photon and ratiometric imaging 77
3.1 Introduction 78
3.2 Results and discussion 80
3.2.1 Initial engineering of REX-GECO0.1 80
3.2.2 Rational design and directed evolution of REX-GECO0.1 for improved function 83
3.2.3 *In vitro* characterization of REX-GECOs 85
3.2.4 Live cell performance of REX-GECO1 with 1-photon and 2-photon excitation 89
3.2.5 REX-GECO1 for dual color imaging in rat hippocampal organotypic slice cultures 96
3.2.6 REX-GECO1 for *in vivo* imaging 98
3.3 Conclusion 101
3.4 Materials and methods 102
3.4.1 Engineering and screening of REX-GECO 102
3.4.2 Characterization of REX-GECO1 103
3.4.3 Plasmids for mammalian cell imaging 105
3.4.4 Cell culture 106
3.4.5 Transfection of rat hippocampal organotypic brain slices 106

3.4.6 Microscopes for fluorescence imaging 108
3.4.7 Imaging of rat organotypic hippocampal slices 108
3.4.8 REX-GECOs *in vivo* 110
Chapter 4 Red fluorescent genetically encoded Ca^{2+} indicators with low affinities for use in mitochondria and endoplasmic reticulum 113
4.1 Introduction 114
4.2 Results and discussion 117
4.2.1 Engineering of LAR-GECO1 and LAR-GECO1.2 117
4.2.2 Engineering of non-cp LAR-GECOs 122
4.2.3 *In vitro* characterization 127
4.2.4 Dual-color ER and cytosolic Ca^{2+} imaging using LAR-GECO1 131
4.2.5 Imaging LAR-GECO1.2 in mitochondria of neurons 132
4.2.6 Detecting store overload-induced Ca^{2+} release using LAR-GECO3 . 135
4.3 Conclusion 136
4.4 Materials and methods 137
4.4.1 Engineering of LAR-GECOs 137
4.4.2 *In vitro* characterization 138
4.4.3 Dual-color ER and cytosolic Ca^{2+} imaging using LAR-GECO1 139
4.4.4 Imaging LAR-GECO1.2 in mitochondria of neurons 139
4.4.5 Imaging LAR-GECO3 in the ER of HEK-293 141
Chapter 5 Development of a red fluorescent probe for glutamate detection 142
5.1 Introduction 143
5.2 Results and discussion 145
5.2.1 Initial engineering of GltR0.1 145
5.2.2 Directed evolution of GltR0.1 for improved function 147
5.2.3 *In vitro* characterization of GltR1 149
5.2.4 Live cells performance of GltR1 152
5.3 Conclusion 153
5.4 Materials and methods 154
5.4.1 Engineering of GltR1 154
5.4.2 *In vitro* characterization of GltR1 155

5.4.3 Live cell imaging of GltR1 in HEK-293 cells and dissociated hippocampal neurons 156
Chapter 6 Conclusions and future directions 159
6.1 Summary of the thesis 160
6.2 Future directions 163
6.2.1 Optimization of the GECOs 163
6.2.2 Optimization of GltR1 164
References 165

List of Tables

Table 2.1. Properties of new GECOs described in this work. 38

Table 2.2. List of substitutions for new GECOs described in this work. Residues are numbered as described in Figure 2.4..... 40

Table 2.3. Systematic characterization of the Ca^{2+}-dependent fluorescence of GECOs in HeLa cells..... 46

Table 2.4. Kinetic characterization of photoactivation in GECOs and RCaMP1.07. 57

Table 3.1. List of substitutions for new GECOs described in this work. Residues are numbered as described in Figure 3.2..... 85

Table 3.2. Properties of new GECOs described in this work..... 86

Table 3.3. Systematic characterization of the Ca^{2+}-dependent fluorescence of REX-GECO1 in HeLa cells with 1-photon (1P) and 2-photon (2P) excitation.. ... 91

Table 4.1. List of substitutions for new GECOs described in this work. Residues are numbered as described in Figure 4.2..... 121

Table 4.2. Properties of new GECOs described in this work. 121

Table 4.3. Mutations introduced into non-cp LAR-GECO1. Residues are numbered as described in Figure 4.4..... 124

Table 4.4. List of substitutions for new GECOs described in this work. Residues are numbered as described in Figure 4.4..... 127

Table 5.1 Substitutions for GltR1 described in this work. Residues are numbered as described in Figure 5.1. 149

Table 5.2. Properties of GltR1. 150

List of Figures

Figure 1.1. Schematic representation of a FP reporter fusion. 3
Figure 1.2. Three-dementional structure of avGFP. 6
Figure 1.3. Chromophore formation mechanism of GFP. 8
Figure 1.4. Chromophore formation mechanism of DsRed. 9
Figure 1.5. *E/Z* isomers of FP chromophore. 10
Figure 1.6. Tetrameric structure of DsRed (PDB ID 1GGX). 13
Figure 1.7. Representative chromophores for various FP color classes. 14
Figure 1.8. Proton relay of mKeima. Shown are chromophore and the residues involved in ESPT. 16
Figure 1.9. FRET-based FP biosensor designs. 20
Figure 1.10. Schematic representation of the first type of single FP-based biosensors. 24
Figure 1.11. Schematic representation of the second type of single FP-based biosensors. 25
Figure 1.12. Circularly permutation of FP. 25
Figure 1.13. Bimolecular fluorescence complementation strategy. 27
Figure 1.14. Schematic representation of a typical directed evolution process. 29
Figure 2.1. Schematic of the system for image-based screening of *E. coli* colonies. 36
Figure 2.2. Schematic representation, excitation and emission of R-GECO1. 37
Figure 2.3. Characterization of improved indicators. 39
Figure 2.4. Sequence alignment of R-GECO1, R-GECO1.2, CAR-GECO1, and O-GECO1. 41
Figure 2.5. Spectral characterization of O-GECO1, CAR-GECO1 and R-GECO1.2. 43
Figure 2.6. Representative intensity vs. time traces for HeLa cells transfected with: (A) O-GECO1; (B) CAR-GECO1; and (C) R-GECO1.2. 45
Figure 2.7. Characterization of plasma membrane targeted Lyn-R-GECO1.2. 48
Figure 2.8. Imaging ChR2-induced Ca^{2+} transients in INS-1 cells. 50
Figure 2.9. Fluorescence traces vs. time for optogenetic activation (440 nm) of HEK293 cells co-transfected with Zebrafish blue opsin, a hybrid Gq/t α subunit, and R-GECO1. 50

Figure 2.10. Confocal imaging of ChR2(T159C)-induced Ca^{2+} elevations in mouse neocortical slice culture. 52

Figure 2.11. ChR2(T159C)-EGFP is activated by 405 nm illumination, but not by 561 nm illumination. 53

Figure 2.12. Reversible photoactivation of Ca^{2+} indicators during 405 nm illumination. 55

Figure 2.13. Characterization of RCaMP1.07 and R-GECO1 photoactivation. 56

Figure 2.14. Averaged absorbance vs. time traces during photoactivation and recovery in the dark. 58

Figure 2.15. pH dependence of photoactivation of Ca^{2+} indicators. 59

Figure 2.16. Change of absorbance for Ca^{2+} indicators in the Ca^{2+}-free state as a function of illumination power (100% = 150 mW). 60

Figure 2.17. Proposed mechanism of photoactivation in red fluorescent GECOs. 62

Figure 2.18. Characterization of R-GECO1-M223Q photoactivation. 63

Figure 3.1. Structure of R-GECO1 and screening scheme for REX-GECO 82

Figure 3.2. Sequence alignment of R-GECO1, REX-GECO0.9 and REX-GECO1. 83

Figure 3.3. Structural model and excitation, emission spectra of REX-GECO1 85

Figure 3.4. Characterization of REX-GECO0.9 and REX-GECO1. 87

Figure 3.5. Characterization of REX-GECO0.9 and REX-GECO1 photoactivation. 88

Figure 3.6. Imaging REX-GECO1 with 1-photon and 2-photon excitation. 90

Figure 3.7. Confocal imaging of REX-GECO1 in neurons and glial cells in organotypic brain slices. 92

Figure 3.8. Confocal imaging of REX-GECO1 controlled by human synapsin I promoter and cytomegalovirus (CMV) promoter in rat hippocampal brain slices. 93

Figure 3.9. 1-photon confocal dual-color imaging of REX-GECO1 co-expressed with a green glutamate indicator (iGluSnFR) in organotypic rat hippocampal slices. 95

Figure 3.10. 2-photon dual-color imaging of neurons co-expressing REX-GECO1 and iGluSnFR in organotypic rat hippocampal brain slices. 97

Figure 3.11. *Ex vivo* and *in vivo* 2-photon microscopy of REX-GECO responses to pharmacological and visual stimulation in the retinotectal system of Xenopus laevis tadpoles. 100

Figure 4.1. Strategies and dissociation constant for LAR-GECO1 and LAR-GECO1.2. 118

Figure 4.2. Sequence alignment of R-GECO1, LAR-GECO1, R-GECO1.2 and LAR-GECO1.2. 120
Figure 4.3. Strategies and dissociation constant for LAR-GECO2, LAR-GECO3, and LAR-GECO4. 123
Figure 4.4. Sequence alignment of non-cp LAR-GECO1, LAR-GECO2, LAR-GECO3, and LAR-GECO4. 126
Figure 4.5. Characterization of LAR-GECO1 and LAR-GECO1.2. 128
Figure 4.6. Characterization of LAR-GECO2, LAR-GECO3, and LAR-GECO4. 129
Figure 4.7. Dual-color imaging of cytosolic and ER luminal Ca^{2+} using ER-LAR-GECO1 and Cyto-GCaMP3. 132
Figure 4.8. LAR-GECO1.2 for imaging mitochondrial Ca^{2+} in DRG and hippocampal neurons. 134
Figure 4.9. LAR-GECO3 in RyR2-expressing HEK-293 cells. 136
Figure 5.1. Sequence alignment of iGluSnFR, cp-RFP (from R-GECO1) and GltR1. 146
Figure 5.2. Emission spectra of GltR0.1 from bacterial protein extract with or without 2 mM glutamate. 147
Figure 5.3. Normalized excitation and emission spectra of GltR1 with or without 2 mM glutamate. 149
Figure 5.4. Fluorescence intensities of GltR1 with (pink) and without (grey) glutamate as a function of pH. 151
Figure 5.5. Normalized fluorescence intensity of GltR1 as a function of different concentrations of analytes 151
Figure 5.6. Performance of GltR1 expressed on the surface of HEK-293 cells. 152
Figure 5.7. Detection of spontaneous glutamate dynamics on the surface of dissociated rat hippocampal neurons. 153

List of Abbreviations

Å	Angstrom
Asp	Aspartate
ATP	Adenosine triphosphate
Arg	Arginine
avGFP	*Aequorea victoria* GFP
BFP	Blue fluorescent protein
BiFC	Bimolecular fluorescence complementation
C. elegans	*Caenorhabditis elegans*
CaM	Calmodulin
cm	Centimeter
CFP	Cyan fluorescent protein
cpFP	Circularly permuted fluorescent protein
DMEM	Dulbecco's modified eagle media
DNA	Deoxyribonucleic acid
dNTPs	Deoxynucleotide triphosphates
DsRed	*Discosoma species* Red fluorescent protein
ε	Extinction coefficient
E. coli	*Escherichia coli*
EDTA	Ethylenediaminetetraacetic acid
EGTA	Ethylene glycol-bis(2-aminoethylether)-*N,N,N′,N′*-tetraacetic acid
eGFP	Enhanced green fluorescent protein
ER	Endoplasmic reticulum

ESPT	Excited state proton transfer
FP	Fluorescent protein
FRET	Förster resonance energy transfer
GFP	Green fluorescent protein
Gln	Glutamine
Glu	Glutamate
Gly	Glycine
GECO	Genetically encoded Ca^{2+} indicators for optical imaging
His	Histidine
Ile	Isoleucine
kDa	Kilodalton
K_d	Dissociation constant
mL	Milliliter
ng	Nanogram
NIR	Near-infrared
n_H	Hill coefficient
nm	Nanometer
nM	Nanomolar
NTA	Nitrilotriacetic acid
PBS	Phosphate buffered saline
PCR	Polymerase chain reaction
POI	Protein of interest
RET	Resonance energy transfer
RFP	Red fluorescent protein

Ser	Serine
SR	Sarcoplasmic reticulum
Tyr	Tyrosine
µg	Microgram
µM	Micromolar
YFP	Yellow fluorescent protein

Chapter 1 General introduction[1]

[1] Figures 1.7, 1.9, 1.11 and 1.13 in this chapter were adapted from the following publication: S. C. Alford, J. Wu, Y. Zhao, R. E. Campbell, and T. Knöpfel, “Optogenetic reporters”. *Biol. Cell*., 105, 14–29 (2013).

1.1 Overview and premise

Fluorescence microscopy is an indispensable technology for life science research. One of the defining features of fluorescence microscopy is its ability to visualize the localization and real time dynamics of low concentrations of fluorescent molecules. As a critical component in fluorescence microscopy, molecules with genetically encodable fluorescence are the workhorses of live cell imaging. These genetically encoded fluorescent molecules have revolutionized the field of cell biology by enabling novel approaches to study protein localization, enzymatic activity and dynamic changes in the concentration of signalling molecules.

Among all the fluorescent molecules, fluorescent proteins (FPs) have been proven to be one of the most useful tools in fluorescence microscopy, especially in the area of live cell imaging. FPs can be defined as a class of homologous proteins that can be excited and will subsequently emit visible light. Since FPs are genetically encoded fluorophores, they can be delivered into living organisms by the introduction of their corresponding genes. As a result, FPs enable imaging in living cells with minimal invasiveness. Furthermore, FPs usually serve as a 'marker' for studying the location or even function of a protein-of-interest. In this case, a FP is tethered to a protein-of-interest by means of genetic manipulation where the gene of the FP is fused to the gene of the protein-of-interest. Expression of this chimeric gene leads to the production of a FP tethering to the protein-of-interest (Figure 1.1).

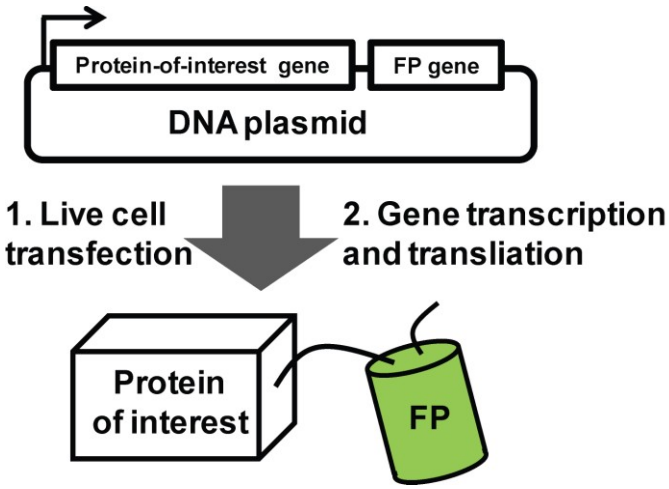

Figure 1.1. Schematic representation of a FP reporter fusion.

Besides serving as a fluorescent 'marker', FPs have also been engineered into FP-based indicators for sensing various analytes. The term 'FP-based indicators' used here can be defined as a chimeric protein consists of one of more FPs that will respond to an analyte by changing its optical signal. Numerous efforts invested in this field have lead to the development of FP-based indicators for numerous signaling molecules in cell biology, such as calcium ion (Ca^{2+}) (*1*–*3*), proton (H^{+}) (*4*), chloride ion (Cl^{-}) (*5*–*7*), glutamate (Glu) (*8*, *9*) and adenosine triphosphate (ATP) (*10*, *11*).

In this thesis, I will describe our successful efforts in developing a series of FP-based Ca^{2+} and glutamate indicators with various colors and useful spectral properties. In the remainder of this introductory chapter, I will present a brief overview of several relevant topics including the discovery and subsequent developments and applications of FPs, FP-based indicators and the strategies used for protein engineering.

1.2 Fluorescent proteins

1.2.1 Natural sources

Green fluorescent protein (GFP) was first discovered in jellyfish, *Aequorea victoria*, by Dr. Osamu Shimomura in 1962 during his study on a protein, Aequorin, in this marine organism (*12*). In his paper, Dr. Shimomura documented "…on gentle mechanical stimulation, a greenish luminescence arises…" from these jellyfish (*12*). Following its discovery, GFP did not gain instant popularity until 1992, when Dr. Douglas Prasher first cloned and sequenced the gene of GFP (*13*), followed by later efforts in 1994, when Dr. Martin Chalfie first expressed GFP in *Escherichia coli* and *Caenorhabditis elegans* (*14*).

Despite the revolutionary discovery and growing popularity of GFP, the increasing demand for additional FP variants with new properties had prompted researchers to start new FP gene hunt in other marine organisms. These efforts led to the finding of GFP homologues in reef coral with fluorescent hues range from cyan to red (*15*). Among these new FPs, the most popular variant, *Discosoma sp.* Red fluorescent protein (DsRed) (*15*), and its derivatives (*16*) have proved to be indispensable molecular tools in fluorescent imaging. Continuous efforts had led to the discovery of various GFP homologues in lancelet and copepod crustacean (*17–20*). Together, these 'glowing' genes from nature comprise the FP toolbox that launched the era of fluorescent live cell imaging.

1.2.2 Primary sequence and three-dimensional structure

As Dr. Douglas Prasher first cloned and sequenced *Aequorea victoria* GFP (avGFP), it revealed this protein's complete primary sequence of 238 amino acids with a molecular mass of ~27 kDa (*13*). Among the primary sequence of avGFP, a tripeptide, namely Ser65-Tyr66-Gly67, is self-sufficient to post-translationally form an intrinsic chromophore that gives rise to the unique fluorogenic property (*21*, *22*). Although homologues of GFP with different hues were later engineered by mutational studies (*23*, *24*), and discovered in reef coral (*15*), Tyr66 and Gly67 have been shown to be highly conserved among FPs from different organisms (*25*).

The unique fluorogenic property of FPs will not be fully appreciated without the understanding of its three-dimensional structure. To bridge this gap, two groups independently reported the X-ray crystal structure of avGFP in 1996 (*26*, *27*). These X-ray crystal structures revealed that avGFP adopts a cylinder shape by eleven β strands wrapped around a central helix. Owing to its unique structure, this eleven-stranded cylindrical protein fold is often referred to as β-can or β-barrel. This β-barrel is ~42 Å in height and ~24 Å in diameter (*27*) (Figure 1.2A). The chromophore, formed by the Ser65-Tyr66-Gly67 tripeptide, is in the middle of the central helix and is located near the center of the β-barrel, protected by the eleven β strands from the exposure to the surrounding solvents (Figure 1.2B). As the toolbox of FPs expanded, later studies showed that FPs from reef coral also share a similar eleven-stranded β-barrel structure (*15*, *28*).

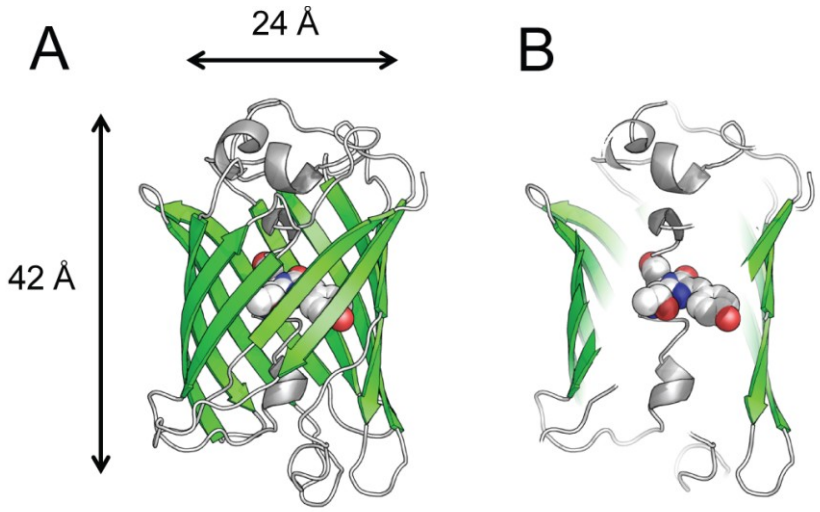

Figure 1.2. Three-dimensional structure of avGFP. (A) A cartoon representation of avGFP (PDB ID 1EMA) (*27*) with the chromophore shown in space-filling representation with carbon, nitrogen and oxygen atoms colored as white, blue and red, respectively. (B) The same representation as (A) but with the protein sliced through the middle to reveal the chromophore.

1.2.3 Chromophore formation

The fluorogenic property of FPs is attributed to their autogenic formation of a visible wavelength chromophore within the β-barrel. In avGFP and GFP-like proteins, a tripeptide, Ser65-Tyr66-Gly67 (in GFP-like proteins, it could be other residues in position 65), spontaneously undergo post-translational modification to form the fluorescent chromophore (*21*, *22*). However, this process is only spontaneous when the tripeptide is in a folded β-barrel protein structure where it is protected from solvents and constrained to a proper conformation (*29*). Given the importance of the chromophore to FPs, its formation mechanism remains

elusive due to different yet conflicting evidence suggested by different reports (*30*–*36*).

Our current understanding suggests the formation of the avGFP (and GFP-like proteins) chromophore must involve three key steps: (1) cyclization, (2) oxidation, and (3) dehydration. However, the order of this three-step reaction remains an open question. An early proposed mechanism suggests the chromophore formation process occurs following the order of cyclization-dehydration-oxidation (*23*). Specifically, the amide nitrogen in Gly67 attacks the carbonyl from Ser65, forming a 5-membered ring intermediate. This intermediate then undergoes oxidation (*37*), followed by dehydration to form the phenol chromophore. The phenol chromophore then loses a proton to form the anionic chromophore. The green fluorescence in avGFP is attributed to both the phenol and anionic forms of the chromophore. Although this mechanism is supported by previous studies (*32*, *36*, *38*), increasing evidence suggests the formation of avGFP's chromophore occurs in the order of cyclization-oxidation-dehydration (*35*) (Figure 1.3).

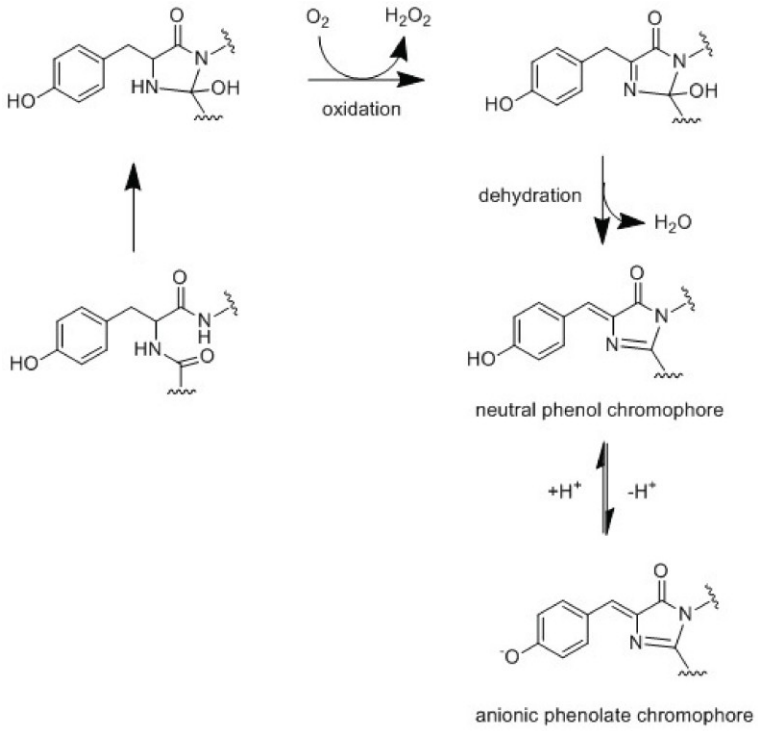

Figure 1.3. Chromophore formation mechanism of GFP.

Similar to avGFP, red fluorescent protein, DsRed, from reef coral forms its chromophore from a tripeptide, Gln65-Tyr66-Gly67, in the folded β-barrel protein. Interestingly, during the maturation of the red fluorescent DsRed, green fluorescence was first observed then declined (*39*). This led to a proposed mechanism whereby a green fluorescent chromophore structure was the precursor of the red form (*39*, *40*). However, later studies suggest that the amount of green fluorescent chromophore does not decrease (*41*, *42*). The observed green fluorescence decline is due to intramolecular Förster resonance energy transfer (FRET) in the tetrameric DsRed (*39*, *43*).

More recent studies suggest a new mechanism that reconciles the somewhat conflicting observations of DsRed chromophore formation process

from the previous studies (*37*). In this mechanism, the formation of a DsRed chromophore starts on the cyclization step as in avGFP to form a 5-membered ring intermediate. Instead of undergoing the next step on the avGFP pathway, this 5-membered ring intermediate equilibrates with a cyclic imine, which then undergoes irreversible hydroxylation and dehydration to form the phenol form of the red chromophore (Figure 1.4). This phenol chromophore undergoes deprotonation to form the anionic form of the chromophore that gives rise to the characteristic red fluorescence of DsRed (Figure 1.4).

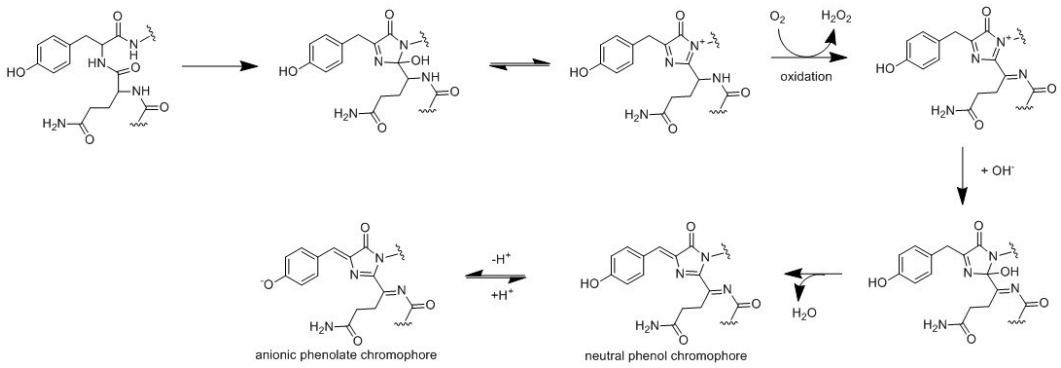

Figure 1.4. Chromophore formation mechanism of DsRed.

Another feature of a FP chromophore is its *E*/*Z* stereoisomeric property. There are two possible isomers of the oxidized tyrosyl α-β bond in a FP chromophore. In principle, a FP's chromophore can exist in either the *Z* configuration or the *E* configuration depending on its adjacent environment. In practice, most FP discovered in nature or engineered in the laboratory exists as a *Z* stereoisomer (*44*) as shown in (Figure 1.5). There are only a few examples of FP that have a *E* configuration (*45*, *46*). Interestingly, studies have shown some

FPs' chromophore can undergo photoisomerization between an *E* isomer and a *Z* isomer (*47*).

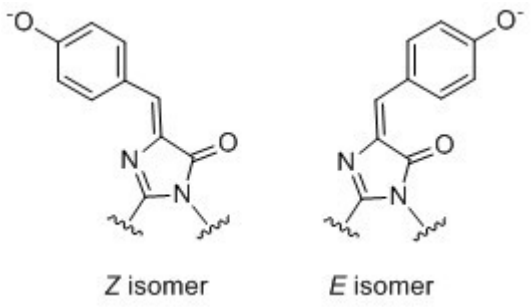

Figure 1.5. *E/Z* isomers of FP chromophore.

1.2.4 Engineered FP variants

Given most naturally occurring FPs were discovered in organisms from the ocean, millions of years of evolution has rendered them to be optimal under such environment. Some of this optimization could even hamper the application of FPs in cell biology. One of such examples is the rate of protein folding and chromophore maturation of FPs. Since most FPs were optimized for their native environment with temperature much lower than 37 °C, expressing them in living cells with ~37 °C could be detrimental for their protein folding and chromophore maturation. Moreover, most FPs discovered in nature exhibited certain degrees of oligomerization. Many natural FPs are obligate oligomers (often tetramers), which severely limits their usefulness in imaging and tracking proteins of interest in living cells. In addition, despite the availability of the naturally occurring green fluorescent avGFP and red fluorescent DsRed, FPs with other favourable

properties such as expended range of hues, higher photostability and enhanced quantum yield are still in great demand. To fix the inherent problems and expand the versatility of the FP toolbox, numerous efforts were invested into engineering different FP variants.

1.2.4.1 Engineered FPs with fast folding and maturation

The application of FPs in live cell imaging has been hampered by their slow protein folding and chromophore maturation (*39*). The protein folding and maturation efficiency of FPs are temperature-dependent. This phenomenon seems likely to come from the evolutionary adaptations of FPs to their natural habitats. In the case of avGFP, it exhibits the maximal folding efficiency under room temperature (~22 °C), whereas for most FPs from reef coral, they display better protein folding and faster chromophore maturation at higher temperatures (≥ 30 °C). To fully realize the potential of FPs, extensive efforts had been invested to enhance their folding and maturation efficiency under 37 °C for live cell imaging (*48*–*50*). In one example, the slow folding problem of DsRed was addressed by random and directed mutagenesis (*49*). The resulting fast maturing variant, named as DsRed.T1, displays a ~15-fold increase of folding and maturation efficiency compared with its progenitor, DsRed, from reef coral (*49*).

1.2.4.2 Engineered FPs with monomeric property

Besides slow folding and maturation under 37 °C, another drawback of the naturally occurring FPs is their tendency to oligomerization. When fused to a protein-of-interest for imaging, FPs with self-associating property will perturb the proper localization and normal dynamics of this protein. In the X-ray crystal structure, avGFP exists as a dimer with multiple hydrophilic interactions at the interface (*26*). Indeed, various studies showed that avGFP is a weak dimer with a

dissociation constant (K_d) of 60-100 μM (*51–53*). Fortunately, introduction of a single mutation Ala206 to Lys can abolish this dimeric tendency in avGFP (*52*).

Other than avGFP, this oligomerization tendency also persists in Anthozoan FPs (*28*, *46*, *54*). In the case of DsRed from reef coral, it forms an obligate tetramer in its native state, but unlike avGFP, each DsRed in the tetramer interacts with two adjacent protomers via two different interfaces (*28*, *54*) (Figure 1.6). One basic strategy for decreasing the oligomeric state was to modify the surface residues on the interface of each protomers (*55*). However, due to the tetrameric nature, disruption of the interfaces usually lead to severe to even complete loss of fluorescence from the FPs. In the first successful efforts to engineer DsRed into a monomeric version, known as mRFP1, surface residues were modified to decrease the interactions between protomers. The loss of fluorescence from this modification was rescued by extensive protein engineering and directed evolution (*55*). The resulting variant, mRFP1, has a total of 33 mutations from DsRed (*55*). This monomeric RFP exhibits rapid maturation and is suitable for application in multicolor imaging in combination with GFP (*55*).

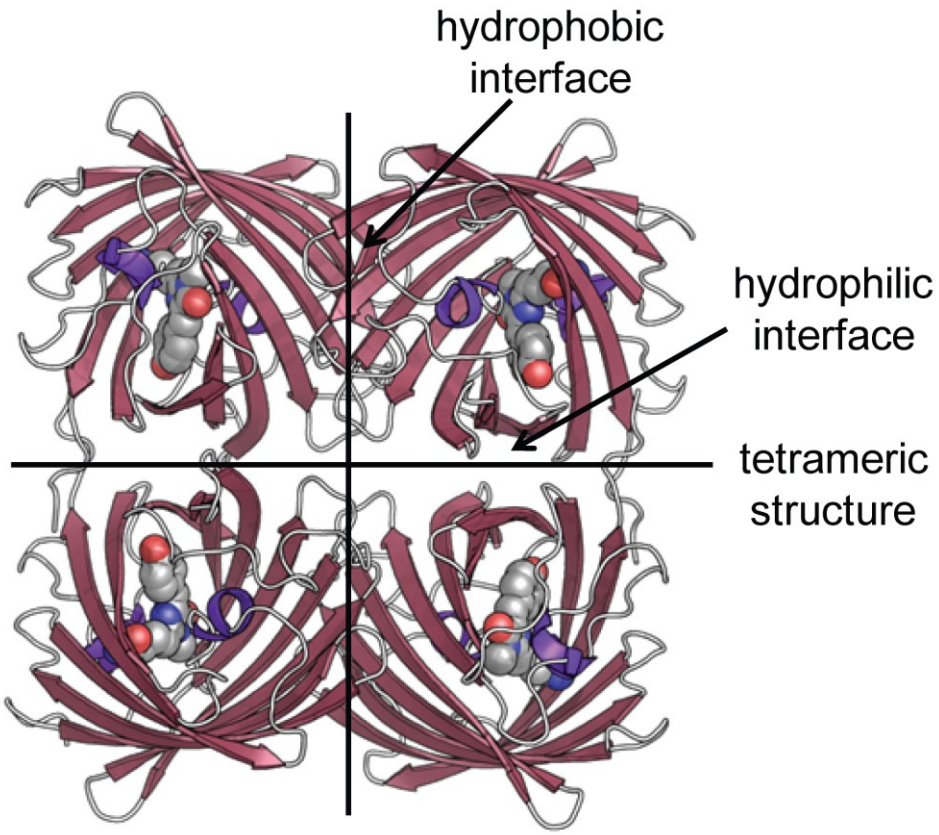

Figure 1.6. Tetrameric structure of DsRed (PDB ID 1GGX) (*28*).

1.2.4.3 Engineered FPs with different hues

The FPs color palette is not limited to just avGFP and DsRed, FPs with other colors were later discovered from nature and were engineered based on existing FPs in laboratories. Usually, FPs are categorized according to the fluorescence emission wavelengths (colors) from their chromophores: blue FPs, 440-470 nm; cyan/teal FPs, 470-500 nm; green FPs, 500-520 nm; yellow FPs, 520-550 nm; orange FPs, 550-575 nm; red FPs 575-650nm (Figure 1.7).

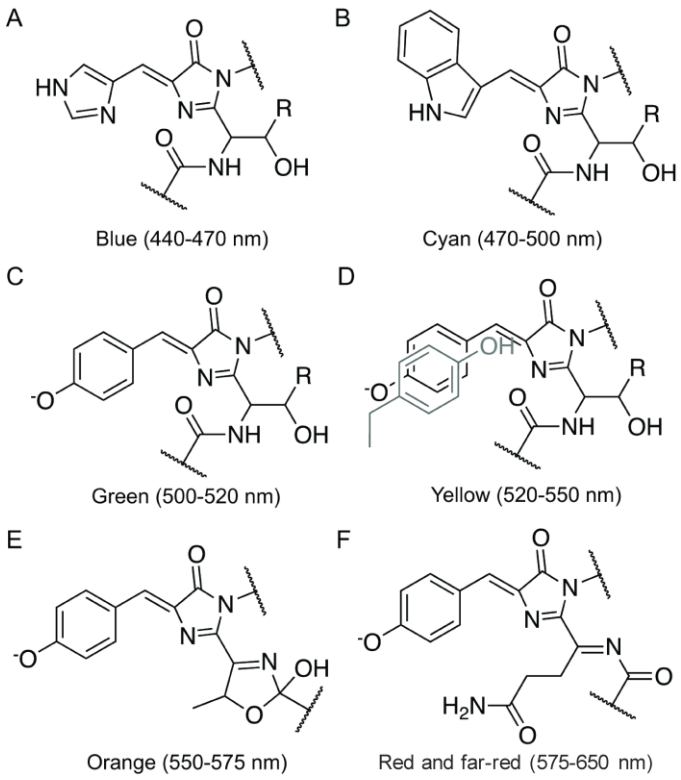

Figure 1.7. Representative chromophores for various FP color classes.

Besides avGFP and DsRed, more FPs with unique chromophore structure and colors have been discovered in nature. A tetrameric yellow FP, zFP538, from *Zoanthus* contains a novel three-ring chromophore structure (*56*). An orange FP originally discovered in stony coral *Fungia concinna* (*57*) shows another unique three-ring chromophore structure that gives rise to an emission maxima of 559 nm (*58*).

Since the unique conjugated structure of the chromophore gives rise to the fluorogenic feature of FPs, modifying its structure can lead to alteration of FPs' colors. Only by mutating Tyr66 to His, researchers were able to turn avGFP (with emission maxima of 508 nm) into a blue FP (with emission maxima of 448

nm) (*23*) (Figure 1.7A). In the same studies, it was also demonstrated that mutating Tyr66 to Trp, avGFP was turned into a cyan FP (with emission maxima of 480 nm (*23*)) (Figure 1.7B). Similar strategies were applied to monomeric RFP, where mutating Tyr66 to Trp generated a yellow FP variant, mHoneydew (*16*). Moreover, mutating Tyr66 to Phe in an highly optimized monomeric RFP, mCherry, lead to the identification of a blue variant, mBlueberry (*59*). Besides Tyr66, mutating Gln65 in mRFP1 to Thr generated an orange color variant, with the formation of a third ring from the hydroxyl of this Thr65 residue to the main chain acylimine moiety (*16*) (Figure 1.7E).

Another strategy to modulate the hues of FPs is by mutating the adjacent residues that non-covalently interacting with the chromophore. An elegant example of this strategy was demonstrated by developing a yellow FP (*27*). Specifically, Thr203 in GFP was mutated to a Tyr whose phenol ring forms a π-π stacking to the phenol ring of the GFP chromophore. This effect red-shifted the emission peak of GFP from 511 nm to 525 nm to become a yellow FP (*27*) (Figure 1.7D). In another example, an mRFP variant with an emission maxima at 612 nm was engineered to have a red-shifted emission at 649 nm (*60*). A later study showed that this drastic red-shift of the emission is mainly attributed to a single mutation Val16 to Glu, which creates a chromophore environment that allows solvent reorganization to decrease the excited state chromophore energy (*61*).

Mutating surrounding residues to the chromophore can not only shift FPs' emission spectrum, but also generate FPs with novel spectral properties. In one example, a red FP variant from the stony coral *Montipora* was engineered to exhibit peak excitation and emission at 440 nm and 620 nm, respectively (*62*).

This unique long Stokes shift between the excitation and emission is due to a process called excited state proton transfer (ESPT) supported by a novel hydrogen bond network in close proximity to the phenol group of the chromophore (*63*). Specifically, the side chain of Asp157 destabilizes the anionic phenolate form (absorbance ~575 nm; fluorescence ~620 nm) and thereby helps maintain the chromophore in the neutral phenol form (absorbance ~440 nm; typically non-fluorescent) at physiological pH. Illumination with ~440 nm light leads to formation of the excited state of the phenol form which is associated with a decreased pK_a. Accordingly, the proton is transferred from the phenol via Ser142 to Asp157, and the anionic chromophore emits its characteristic red fluorescence (*63*) (Figure 1.8).

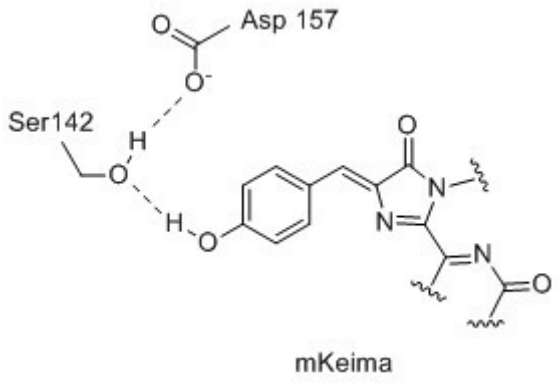

Figure 1.8. Proton relay of mKeima. Shown are chromophore and the residues involved in ESPT.

1.2.4.4 Engineered FPs with other favorable or novel properties

Earlier efforts of FP engineering was focused on fixing some inherent problems of FPs, such as slow folding and maturation, tendency for oligomerization, and limited hues, nevertheless, more recent studies have shifted the focus to engineer FPs as versatile molecular tools. In a recent study, a monomeric RFP, mCherry, was demonstrated to be suitable for opto-acoustic tomography (*64*). Another direction of FP engineering is focused on generating FP variants with high extinction coefficient but very low quantum yield as dark FRET acceptors. A YFP variant (*65*) and a recently developed chromoprotein, Ultramarine (*66*), both showed great promise for this technique. Despites most applications of FPs employ their fluorogenic feature, a recent study discovered a light-dependent dissociation and association phenomenon on a FP, Dronpa (*67*), which can be used as a light-sensitive domain for optical control of protein activity (*68*).

1.2.5 Applications of FPs

The most common application of FPs is to use them as a reporter to track the dynamics of a protein-of-interest in live cells. Specifically, a FP is genetically fused to a protein-of-interest. During expression in live cells, a FP will be tethered to each protein-of-interest. By fluorescence microscopy, one can easily observe the dynamics and localization of this protein-of-interest. Besides serving as a reporter for a target protein, FPs can also work as an indication of a specific gene promoter's activity. To visualize the activity of a gene promoter, the gene of a FP is genetically placed under the control of such promoter. Switching this promoter from 'off' to 'on' will lead to the transcription and translation of the FP's gene. In

this way, the activity of a target promoter can be visualized by the fluorescence readout from the FP under fluorescence microscopy.

In addition to functioning as a reporter for a target protein or gene promoter, a new class of photoactivatable or photoswitchable FPs enables fluorescence imaging to achieve super-resolution (*69*). In this technique, a photoactivatable or photoswitchable FP is genetically fused to a target protein, so that this FP is tethered to the protein-of-interest during expression as discussed above. This class of FPs has a unique highlightable feature, i.e. illumination will cause their chromophore to undergo a conversion from a non-fluorescent to a fluorescent state (*67*, *70*). During imaging, instead of illuminating all the FPs at once, a sparsely distributed sub-population of FP molecules is highlighted from a non-fluorescent to a fluorescent state, followed by image acquisition, and bleaching. This highlight-acquisition-bleach process is repeated to generate images with resolution up to 20~30 nm (*69*).

Besides engineering and applying FPs as reporters, another major aspect of FPs application is to develop and engineer genetically encoded FP-based biosensors. This aspect will be discussed in detail in the next section.

1.3 Genetically encoded FP-based biosensors

A biosensor is defined as a system or platform that consists of a biomolecule for analyte recognition and a transducer for converting this recognition event to an observable signal output (*71*, *72*). The term 'genetically encoded FP-based biosensors' is usually appreciated as a protein-based biosensor that utilizes FPs for its signal transducer element (*71*). The fact that a

protein-based biosensor can be readily manipulated makes it a versatile tool for bioanalytical research. Moreover, given its unique fluorogenic property and the high sensitivity of fluorescence, FPs are promising candidates as a transducer element in a biosensor. Depending on its design, genetically encoded FP-based biosensors can be categorized into three general classes: FRET-based biosensors, single FP-based biosensors, and bimolecular fluorescence complementation (BiFC)-based biosensors.

1.3.1 FRET-based biosensors

FRET is a non-radiative quantum mechanical process, in which the excitation energy from a donor chromophore (with higher energy, shorter wavelength) is transferred to an acceptor chromophore (with lower energy, longer wavelength) via dipole-dipole interaction (*73*). The process of FRET depends on the distance (usually within 10 nm), orientation, and the spectral overlap of the donor and acceptor chromophores. Having hues that cover the whole visible spectrum renders FPs excellent candidates for designing FRET-based biosensors. A general rationale for designing FRET-based biosensors is to couple a protein-protein interaction, the activity of an enzyme, or the presence of an analyte to the energy transfer efficiency between a donor FP to an acceptor FP (*71*). A summary of these designs are illustrated in Figure 1.9.

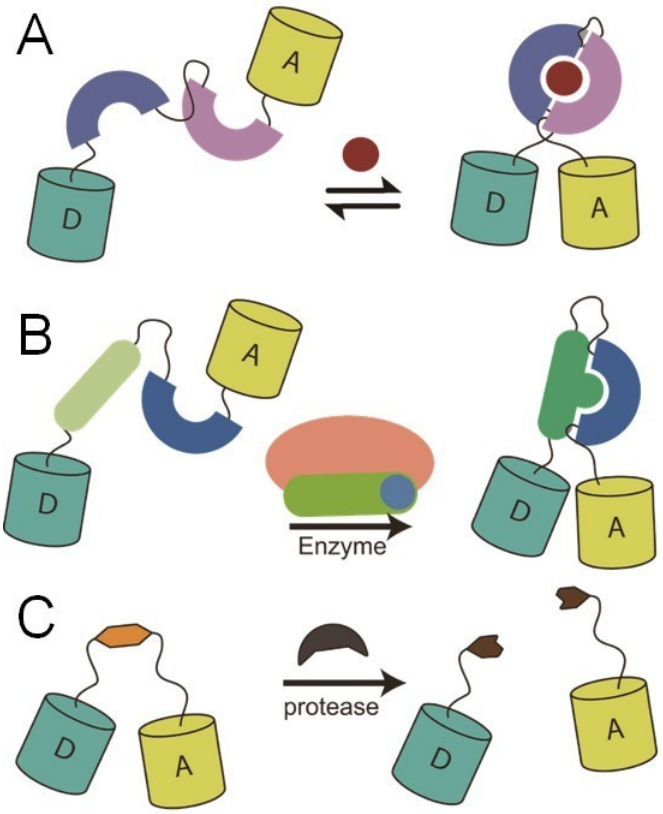

Figure 1.9. FRET-based FP biosensor designs. (A) An intramolecular biosensor of small molecules (red circle). (B) A biosensor of enzymatic activity. (C) A protease biosensor.

In the first design (Figure 1.9A), the FRET efficiency between the donor FP and the acceptor FP is coupled to the presence of an analyte via a protein sensing domain. When the analyte, usually a small molecule, is present, the protein sensing domain will bind to this molecule and undergo a conformational change that changes the distance thus the FRET efficiency between the two FPs. The most famous biosensor based on this design is the Cameleon-type Ca^{2+} indicators (*3*, *74*). This type of Ca^{2+} indicators are composed of a genetic fusion of the Ca^{2+} binding domain calmodulin (CaM) and a short peptide known as M13,

flanked by a blue-shifted donor FP and a red-shifted acceptor FP. As FRET is strongly distant dependent, the Ca^{2+}-dependent interaction of CaM and M13 leads to a change in FRET efficiency and a ratiometric change in the fluorescence signal (*3*).

In the second design (Figure 1.9B), the biosensors' FRET efficiency relies on the conformational change induced by post-translational modifications. This type of biosensors fuses the donor FP and the acceptor FP to each end of a polypeptide that consists of a substrate domain and the corresponding recognition domain. The recognition domain only binds to the enzymatically-modified substrate, which generates a conformational change that changes the FRET efficiency between the donor FP and the acceptor FP. One example of such design is a genetically encoded fluorescent reporter for the activity of serine/threonine kinase protein kinase B (*75*). When the substrate is phosphorylated by kinase B, the FHA2 domain binds to this phosphorylated substrate, which leads to a decrease of FRET efficiency (*75*). This type of design has also been exploited to probe the enzymatic activity of protein kinase A (*76*–*78*), Src (*79*), and GTPases (*80*).

In the last design (Figure 1.9C), the change of FRET efficiency is related to the activity of proteolytic enzymes. Biosensors of this type fuse the donor FP and the acceptor FP to each side of a protease substrate-sequence. When this substrate is proteolyzed by proteolytic enzymes, a loss of FRET can be observed due to the separation of the two FPs. One of the first examples of biosensors based on this design utilized a trypsin-cleavable peptide as the substrate, and fused a BFP and a GFP to its N- and C-termini, respectively (*81*). Other

examples include genetically encoded biosensors for caspase-3 (*82*), and poliovirus 2A protease (*83*).

Despite FRET-based biosensors show great versatility from detecting small molecules, post-translational modification, to the activity of proteolytic enzymes, further developments of this class of biosensors have been hampered by their poor sensitivity due to the imperfect properties of the donor and acceptor FPs. A pair of desirable FPs in FRET-based biosensors should have properties such as high brightness, high photostability, minimal sensitivity to the change of environment, and maximal spectral overlap between the donor and acceptor FPs. One of the most popular choices for engineering FRET-based biosensors is an engineered CFP-YFP pair, known as Cypet and Ypet (*84*). Cypet and Ypet share a good spectral overlap, and exhibit high brightness of fluorescence. In addition, the weak affinity between these two FPs promotes the change of FRET efficiency (*84*). Despite the popularity of the CFP-YFP pair for FRET-based biosensors, the problem of reversible photobleaching (*85*–*87*), photoconversion (*88*), and phototoxicity from the CFP excitation (*89*, *90*) can complicate their application in imaging. To address this problem, a new pair of FPs, known as Clover and mRuby2 (*91*), was engineered and has been shown to exhibit superior performance when used in various FRET-based biosensors (*91*).

1.3.2 Single FP-based biosensors

In contrast to the FRET-based biosensors, single FP-based biosensors only utilize a single FP as the transducer element. The signal readout from this class of biosensors is usually a change of fluorescence intensity, or sometimes a

shift of its excitation or emission spectrum. Compared to ratiometric FRET-based biosensors, the majority of single FP-based ones are intensiometric, yet usually with a greater magnitude of signal change. Based on the design rationale, single FP-based biosensors can be categorized into two types as illustrated in Figures 1.10 and 1.11, respectively.

The first type of single FP-based biosensors takes advantage of the fact that a FP itself is sensitive to the change of the environment (Figure 1.10). One of the first examples of this type of biosensors employed an engineered GFP variant as a biosensor for the change of pH (*4*). This pH indicator, known as pHluorins, responds to the change of pH in the environment by altering the equilibrium of its chromophore between the protonated neural state to the anionic deprotonated state, which leads to a change of its excitation profile (*4*). Another example of employing single FPs for biosensors is a recently developed GFP variant that is capable of sensing the change of Ca^{2+} concentration (*92*). In this design, three β-strands in GFP were engineered to bind to one Ca^{2+} and change the fluorescence intensity of the protein upon binding to Ca^{2+} (*92*). Other single FP-based biosensors include YFP variants with an engineered binding pocket inside the β-barrel for sensing halide ions (*5*–*7*), GFP variants with surface modifications for sensing redox potential (*93*, *94*). Even though this type of design can couple a signal readout to the environmental sensitivity of an FP, the number of analytes or biological processes that can trigger such signal change from the FP is still very limited.

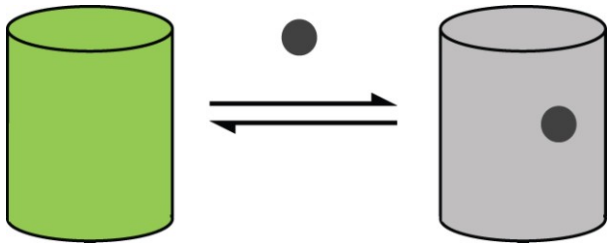

Figure 1.10. Schematic representation of the first type of single FP-based biosensors. The optical readout of the FP changes in response to small ions (grey circle).

To further expand the utility of singe FP-based biosensors for different analytes and biological processes, an extrinsic molecular sensing domain can be fused to an FP so that the recognition from the sensing domain is coupled to the signal change from the single FP, as shown in Figure 1.11. In this type of biosensors, the extrinsic molecular sensing domain is usually fused adjacent to the chromophore of the single FP. An analyte-induced conformational change of the sensing domain will change the microenvironment of the chromophore, which leads to a change of optical readout (*95*). Given the native N- and C- termini of FPs are not close to its chromophore (*27*), fusing the extrinsic molecular sensing domain to these termini is very unlikely to cause any chromophore perturbation. To solve this problem, a technique called circular permutation is employed to generate FPs with new N- and C- termini near its chromophore (*1*, *2*). Specifically, the native N- and C- termini of a FP are linked by a short, yet flexible polypeptide, and the new N- and C- termini are generated near the chromophore (Figure 1.12). By fusing this circularly permuted FP (cpFP) to a sensing domain, the analyte binding-induced conformational change is more readily cause a optical readout from the FP.

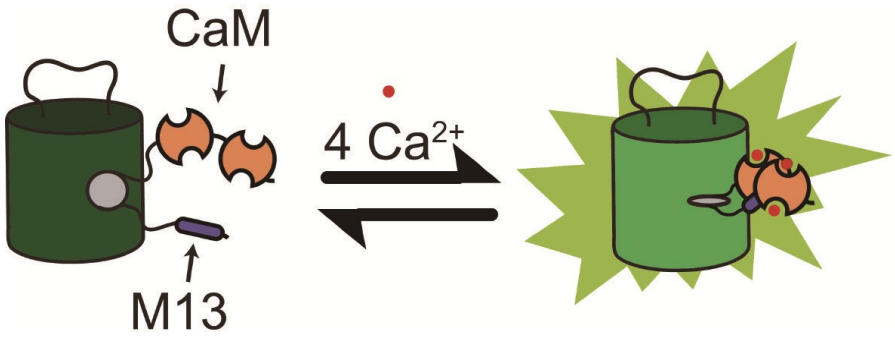

Figure 1.11. Schematic representation of the second type of single FP-based biosensors. Shown is a single FP-based Ca^{2+} biosensor, GCaMP. Ca^{2+}-binding domains CaM and M13 are fused to the new N- and C-termini of a cpGFP. In the absence of Ca^{2+}, the fluorescence is quenched. Upon binding to Ca^{2+}, the conformational change of CaM and M13 restores the fluorescence.

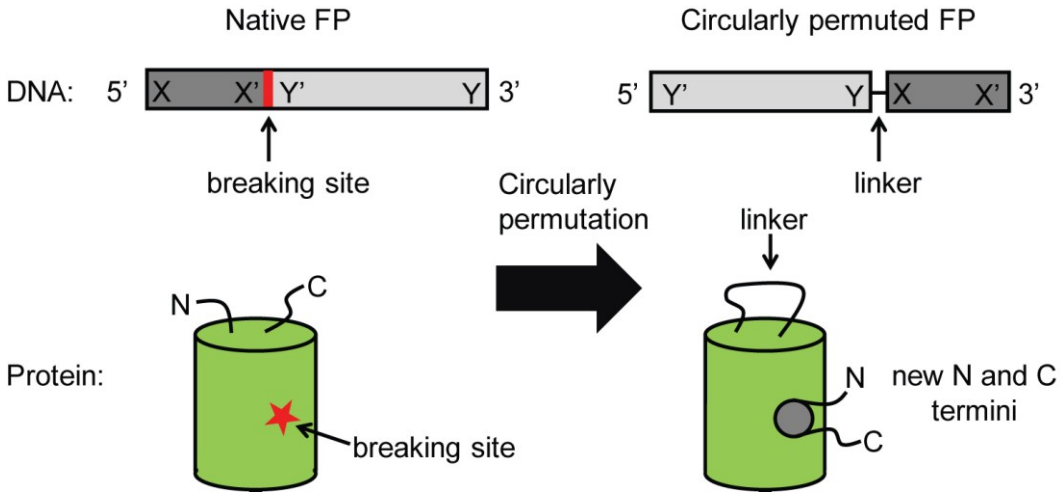

Figure 1.12. Circular permutation of a FP gene. The original N- and C-termini are fused together by a short peptide linker. A new N- and C-termini are created in a close proximity of the chromophore.

One very well-known Ca^{2+} indicator based on this type of design is the GCaMP (*1*, *2*). In the original design of GCaMP, CaM and M13 were fused to the C- and N-termini of a cpGFP. In the Ca^{2+}-free state, CaM and M13 are flexible and the chromophore of the cpGFP exhibits dim green fluorescence due to its exposure to solvent. Binding to Ca^{2+} causes the association of CaM and M13, which modifies the chromophore environment of the cpGFP such that the green fluorescence intensity increases (*96*).

1.3.3 BiFC-based biosensors

Besides using a whole FP or two FPs as the transducer element as previously discussed, protein engineers also utilize the idea of FP complementation to design another class of biosensors, known as BiFC-based biosensors. In this class of biosensors, a FP is genetically separated into two fragments and fused to two potentially interacting protein partners, respectively. Without protein-protein interaction between the target proteins, these two FP fragments exhibit no fluorescence or very low fluorescence. Interaction from the target proteins brings the two FP fragments to a close proximity and renders the reconstruction of a whole fluorogenic FP, thereby indicates their interaction (Figure 1.13).

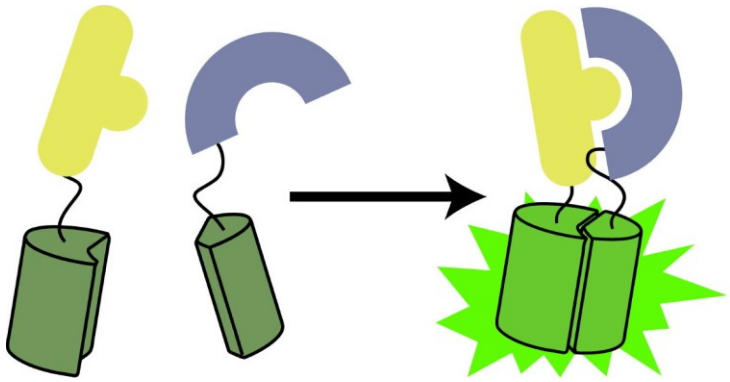

Figure 1.13. Bimolecular fluorescence complementation strategy. Two potential interaction protein partners are fused the non-fluorescent split FP fragments, respectively. Protein-protein interaction of the two partners lead to the association of the two FP-fragments and restores the fluorescence.

This complementation idea was first demonstrated in avGFP in 2000 (*97*). Two fragments of avGFP were fused to leucine zipper domains. Dimerization of the leucine zipper domains lead to the reassembling of a fluorogenic avGFP (*97*). Later efforts have expanded the BiFC-based biosensors color palette to include cyan, yellow, red, and far red (*98*, *99*). The versatility of this class of biosensors have been demonstrated in various aspects in cell biology including applications in high-throughput screening for protein-protein interaction partners (*100*–*105*), detection of deglycosylation in live cells (*106*), and visualization of newly synthesized proteins (*107*, *108*). Nevertheless, an inherent drawback of this class of biosensors is the irreversibility nature of the FP complementation. In applications that are sensitive to this problem, FRET-based biosensors or the recently developed dimerization dependent fluorogenic biosensors (*109*, *110*) might be a better choice.

1.4 Protein engineering

Protein engineering is a process to generate new proteins with desired functions via changing their polypeptide sequence. There are two mutually non-exclusive strategies involved in protein engineering: rational design, and directed evolution. Protein engineering by rational design is usually guided by computational simulation of the protein's sequence-structure-function relationship and/or published crystallographic studies. Started from the 1960s, computational simulation-guided protein engineering has achieved numerous success including the first fully automated designed protein with a novel sequence (*111*), an artificial protein that exhibits unique topology that has not been observed in nature (*112*), protein domains that recognize new target sequences (*113*), and novel catalytic enzymes for different reactions (*114–116*).

Besides rational protein design, directed evolution, as another strategy, offers enormous potential for the protein engineering community to develop novel proteins with desired features. Inspired by the idea of natural selection, directed evolution is a combination of generating libraries of indiscriminately modified variants, and artificially selecting these libraries for variants with desired phenotypes (*117–119*). Specifically, in directed evolution, the following steps are repeated: (1) generation of a gene library with diverse variability; (2) expressing this gene library in a suitable host such as *E. coli*; (3) screening this library by selecting variants with desired features, and using these variants as templates for the generation of next round's gene library (Figure 1.14). The beauty of directed evolution is that it surpasses the intricate relationship between a protein's sequence, structure, and function by applying selection pressure for the

favourable phenotypes. One of the most successful examples of this strategy is the evolution of a protease, subtilisin E, for higher resistant to chemical oxidation and detergent (*120*, *121*). Directed evolution has also been applied in engineering other proteins such as DNA polymerase (*122*), integrase (*123*), endoglucanase (*124*), and even FPs (*44*, *55*, *125*, *126*).

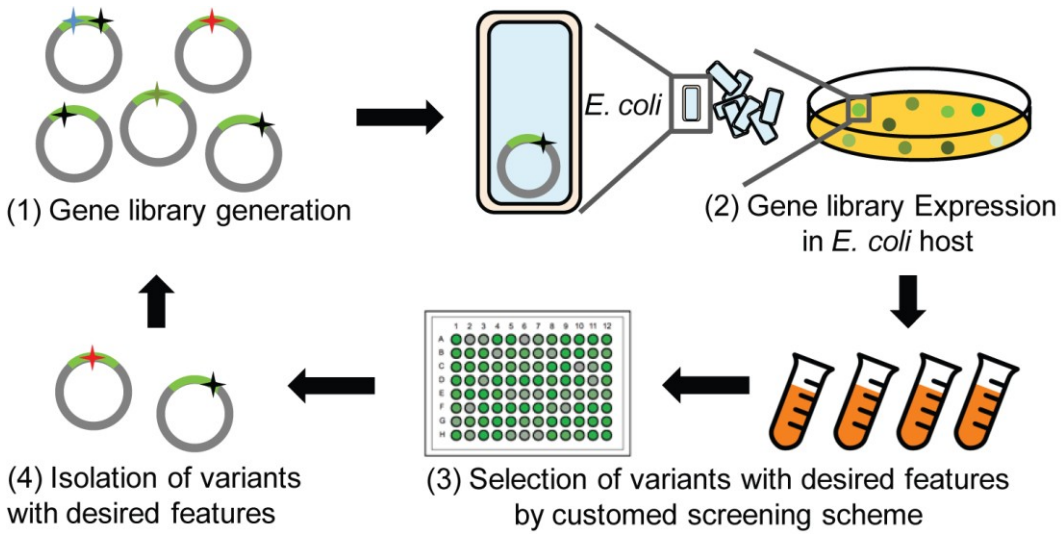

Figure 1.14. Schematic representation of a typical directed evolution process.

As the first step in directed evolution, generating a gene library with diversity is the prerequisite of the subsequent selection. Generation of a gene library cannot be achieved without the invaluable development of molecular biology techniques such as mutagenesis and *in vitro* gene recombination. One of the first examples of site-directed mutagenesis enabled a change of amino acid at a specific position in a protein (*127*). Usually site-directed mutagenesis is combined with computational simulation or crystallographic studies for structure-guided protein engineering. However, given the elusiveness of a protein's

sequence-structure-function relationship, random mutagenesis is usually preferred in generation of gene libraries in directed evolution. Random mutagenesis is carried out by error-prone polymerase chain reaction (PCR) (*128*, *129*). The error rate in this reaction is intentionally controlled by adjusting the concentration of Mn^{2+}, unbalancing the concentration of deoxynucleotide triphosphates (dNTPs), as well as using a low fidelity polymerase for gene amplification (*128*, *130*). Since the majority of point mutations are usually detrimental to the function of a protein, controlling the error rate becomes crucial in generating a gene library as higher error rate leads to higher probability of accumulating more detrimental mutations (*131*, *132*). Due to the nature of this process, accumulation of beneficial mutations for desired protein feature in directed evolution is relatively slow.

To compensate the above shortcoming of random mutagenesis, another technique, *in vitro* gene recombination, allows rapid propagation of beneficial mutations in directed evolution. In *in vitro* gene recombination, fragments of homologous genes are amplified by PCR, annealing of these fragments to different homologous gene templates enables the generation of hybrid genes that might have synergistically beneficial mutations (*133*–*136*). One of the first examples of *in vitro* gene recombination is demonstrated in a TEM-1 derived enzyme, where a 32,000-fold increase of activity was observed (*133*). Based on the initial method of *in vitro* gene recombination (*133*, *137*), improved protocols have also been developed including staggered extension PCR (*134*), random-priming in vitro recombination (*138*).

After the generation of a diverse gene library, screening of the desired phenotype is another essential step. A general rule of thumb in screening a

library is “you get what you screen for” (*139*). An effective screening strategy should not only allow the selection of phenotype with desired properties, but also be sensitive enough to discriminate variants with improved function. In practice, designing such a robust scheme for screening has been proved to be challenging. Common screening strategies usually correlate the activity of the target protein being evolved to other signal outputs such as the production of a fluorophore, and the growth rate under a controlled condition (*139*, *140*).

1.5 The scope of the thesis

The discovery and subsequent applications of FPs have launched the era of fluorescent live cell imaging. The design and developments of FP-based indicators have further solidified the versatility of FPs and rendered them as indispensable tools in life science research now more than ever. Despite the tremendous developments and efforts invested in the field of FP-based indicators, there remain numerous opportunities in engineering indicators with improved or novel properties for studying biological processes *in vivo*. In this thesis we describe our efforts in developing a series of FP-based Ca^{2+} and glutamate indicators with various colors and useful spectral properties as versatile tools for interrogating cell signaling in cell biology.

In Chapter 2, we describe our efforts in employing protein engineering to expand the color palette of genetically encoded Ca^{2+} indicators to include orange and improved red fluorescent variants, known as O-GECO1, R-GECO1.2 and CAR-GECO1, respectively. We also describe our discovery of a photoactivation phenomenon in red fluorescent Ca^{2+} indicators, which could potentially cause

false positive artifacts in Ca^{2+} imaging traces during optogenetic activation with ChR2. At last, we demonstrate, in both a beta cell line and slice culture of developing mouse neocortex, that these artifacts can be avoided by using an appropriately low intensity of blue light for ChR2 activation.

Chapter 3 describes our work to engineer the first excitation ratiometric Ca^{2+} indicator, REX-GECO1, with an optimal 2-photon excitation within the near-infrared (NIR) window (650 to 1000 nm). We demonstrate that REX-GECO1 can be used as either a ratiometric or intensiometric Ca^{2+} indicator in organotypic hippocampal slice cultures (1- and 2-photon) and the visual system of albino tadpoles (2-photon). Furthermore, we demonstrate single excitation wavelength two-color Ca^{2+} and glutamate imaging in organotypic cultures.

In Chapter 4, R-GECO1 and R-GECO1.2 are further engineered into a series of low affinity R-GECOs with K_ds ranging from 12 μM to more than 540 μM. We demonstrate that these indicators can be used to image cell compartments with high Ca^{2+} concentration or with broad range of Ca^{2+} change, such as the endoplasmic reticulum (ER) and mitochondria. We also demonstrate these new red Ca^{2+} indicators with low affinities can be used to monitor ER and mitochondrial Ca^{2+} in combination with a GFP-based reporter.

In Chapter 5, the development, optimization and characterization of a RFP-based glutamate indicator, GltR1, are described. We demonstrate GltR1 can detect glutamate changes on the surface of cultured human cells, as well as the glutamate dynamics during spontaneous activities of dissociated rat hippocampal neurons.

In Chapter 6, we provide a summary of this thesis, and a brief discussion on the future directions in the field of engineering FP-based indicators.

Chapter 2 Development of orange and red Ca^{2+} indicators[2]

[2] A version of this chapter has been published as J. Wu, L. Liu, T. Matsuda, Y. Zhao, A. Rebane, M. Drobizhev, Y-F. Chang, S. Araki, Y. Arai, K. March, T. E. Hughes, K. Sagou, T. Miyata, T. Nagai, W-h. Li, R. E. Campbell, "Improved orange and red Ca^{2+} indicators and photophysical considerations for optogenetic applications", *ACS Chem. Neurosci*., 4, 963–972 (2013). I performed directed evolution and the majority of the characterization of O-GECO1, R-GECO1.2 and CAR-GECO1.

2.1 Introduction

The development of genetically encoded Ca^{2+} indicators has proven to be a great benefit to cell biology, as these tools have enabled the robust visualization and quantification of this key cytosolic second messenger in a diverse array of cell types and tissues (*141*, *142*). The two most important classes of genetically encoded Ca^{2+} indicators are the FRET-based type, such as cameleon (*3*), and the single FP-based type, such as GCaMP (*2*) and flash-pericam (*1*). In the original design of GCaMP, the Ca^{2+} binding domain of CaM, and the CaM-binding region of chicken myosin light chain kinase (M13), were fused to the C- and N-termini of a cpGFP. GCaMP exhibits dim green fluorescence in the Ca^{2+}-free state. Binding to Ca^{2+} causes the association of CaM and M13, which modifies the chromophore environment of the cpGFP such that green fluorescence intensity increases (*96*).

After the advent of the first GCaMP (*2*), the hues of this type of Ca^{2+} indicators have been limited to green. Part of the reason is due to the lack of effective screening strategy for directed evolution of GCaMP-type indicators. To accelerate the development of improved and hue-shifted GCaMP-type indicators, Dr. Yongxin Zhao has developed a colony-based screen for Ca^{2+}-dependent fluorescent changes (Figure 2.1). The premise of this screening system is that Ca^{2+} indicators targeted to the *E. coli* periplasm can be shifted toward the Ca^{2+}-free or Ca^{2+}-bound states by experimental manipulation of the environmental Ca^{2+} concentration. Accordingly, screening of large libraries of genetic variants of GCaMP-type indicators can be achieved by digital fluorescence imaging, at both high- and low-Ca^{2+} conditions, of plates containing hundreds of *E. coli* colonies each. In addition, Dr. Zhao has engineered the prototype of a RFP-based

GCaMP-type indicator, and designated this red fluorescent genetically encoded Ca^{2+} indicators for optical imaging as R-GECO0.1.

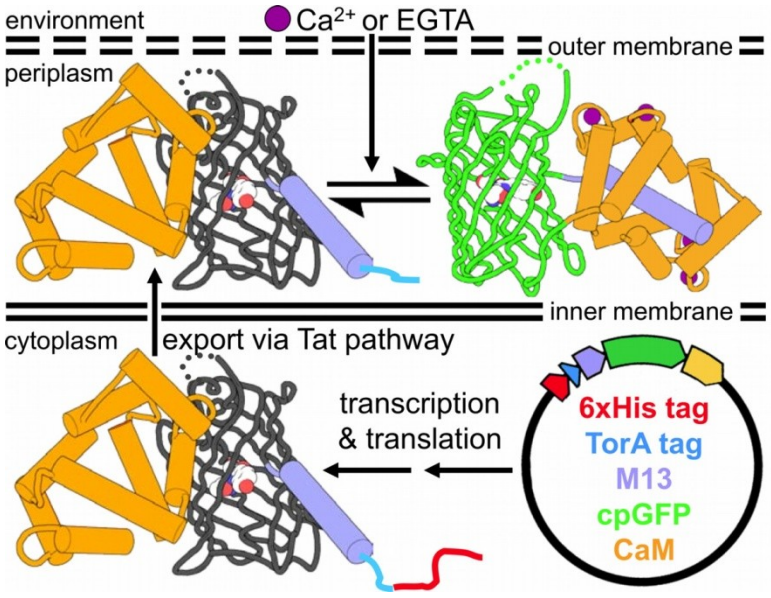

Figure 2.1. Schematic of the system for image-based screening of *E. coli* colonies. The GCaMP variant, as represented by GCaMP2 (PDB ID 3EVU and 3EVR) (*96*), has a TorA periplasmic export tag (*143*).

In this Chapter I will describe my work in the development, optimization, and characterization of a series of orange and red Ca^{2+} indicators. In the course of this work, a photoactivation phenomenon in red fluorescent Ca^{2+} indicators was discovered. I will also describe the *in vitro* characterization of this photoactivation phenomenon and the photophysical considerations for applying these Ca^{2+} indicators in optogenetics.

2.2 Results and discussion

2.2.1 Directed evolution of red Ca^{2+} indicators

R-GECO0.1 was constructed by replacing the cpGFP of G-GECO1.1 (*144*) with an analogous cp version (N_{term}-146 to 231-Gly-Gly-Thr-Gly-Gly-Ser-1 to 145-C_{term}) of the mApple red FP (*16*) (Figure 2.2A). R-GECO0.1 exhibits a modest response to Ca^{2+} with 0.6-fold increase of fluorescence. To optimize the fluorescent brightness and Ca^{2+} response of R-GECO0.1, I performed seven rounds of directed evolution using the colony-based screening system, in which the R-GECO variants were expressed in the periplasm of bacterial colonies. We identified a variant that exhibits a 16-fold fluorescence increase upon binding to Ca^{2+} (Figure 2.2B), and with a K_d to Ca^{2+} of 482 nM (Table 2.1). This variant was designated as R-GECO1.

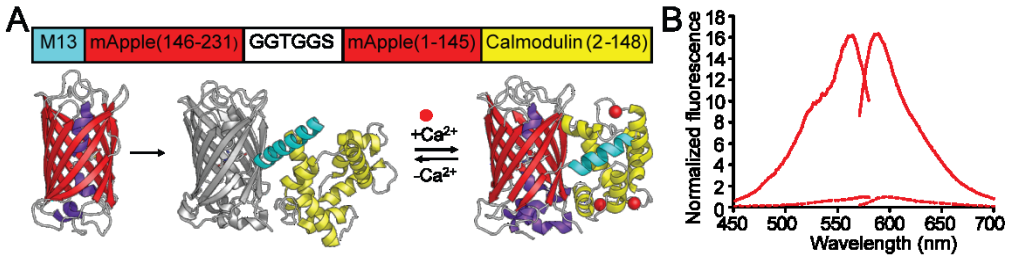

Figure 2.2. Schematic representation, excitation and emission of R-GECO1. (A) Schematic and structural representation of R-GECO1. The RFP structure is from mCherry (PDB ID 2H5Q) (*16*), the Ca^{2+} indicator structures are from G-CaMP2 (PDB ID 3EVU and 3EVR) (*96*). (B) Normalized excitation and emission of R-GECO1 in the Ca^{2+}-free (dashed line) and Ca^{2+}-bound states (solid line).

Table 2.1. Properties of new GECOs described in this work.

Protein	Ca^{2+}	λ_{abs} (nm) (ε) ($mM^{-1}\cdot cm^{-1}$)	λ_{em} (Φ)	Brightness [1] ($mM^{-1}\cdot cm^{-1}$)	pK_a	Intensity change ± Ca^{2+}	K_d for Ca^{2+} (nM) (Hill coefficient)
R-GECO1	-	577 (15)	600 (0.06)	0.72	8.9	16×	482 (2.06)
	+	561 (51)	589 (0.20)	10.2	6.59		
O-GECO1	-	545 (1.4)	570 (0.07)	0.098	9.44	146×	1500 (2.06)
	+	543 (65)	564(0.22)	14.3	6.07		
R-GECO1.2	-	564 (2.8)	595 (0.16)	0.45	8.93	33×	1200 (2.79)
	+	556 (52)	585 (0.29)	15.1	5.99		
CAR-GECO1	-	565 (2.5)	620 (0.11)	0.28	9.05	27×	490 (2.01)
	+	560 (36)	609 (0.21)	7.6	5.74		

[1]Brightness is defined as the product of ε and Φ.

2.2.2 Development of improved orange and red Ca^{2+} indicators

In an effort to expand the number of color choices of Ca^{2+} indicator available to researchers, we took inspiration from the far-red DsRed-derived mPlum variant (*60*) and attempted to similarly engineer variants of R-GECO1 with further red-shifted emission. However, introduction of various combinations of the key mutations of mPlum (Val16Glu, Phe65Ile, Leu124Val, and Ile161Met by DsRed numbering) into R-GECO1 resulted in non-fluorescent proteins or indicators with a drastically diminished Ca^{2+} response relative to R-GECO1. Of those variants that retained a Ca^{2+}-dependent signal, only the Phe65Ile/Ile161Met variant retained a signal change of at least 3-fold (compare to 16-fold for R-GECO1) and had a red-shifted emission peak (597 nm with Ca^{2+}).

Reasoning that alternative substitutions at key positions might further red-shifted fluorescence, we created a genetic library in which the two residues (16 and 65) that are most important to the red shift of mPlum (*61*) were fully randomized. We performed ratiometric fluorescence-based screening of this library expressed in the periplasm of bacterial colonies (*144*), and picked those variants with the highest ratio of 680/40 nm over 610/75 nm emission (535/50 nm excitation). This approach led to the identification of the red-shifted Val16Thr/Phe65Ile variant (emission maximum at 606 nm with Ca^{2+}) with a 9.5-fold intensity change. Further directed evolution with library creation by error-prone PCR and ratiometric screening ultimately led to the production of a variant designated as carmine (i.e., a deep red color) GECO 1 (CAR-GECO1) with fluorescence excitation and emission peaks at 560 nm and 609 nm, respectively, in the Ca^{2+}-bound state (Figure 2.3AB). CAR-GECO1 has 6 mutations relative to R-GECO1 (Figure 2.3D, Figure 2.4, and Table 2.2), and a 2-photon cross-section of 45 GM at 1052 nm (Figure 2.3C).

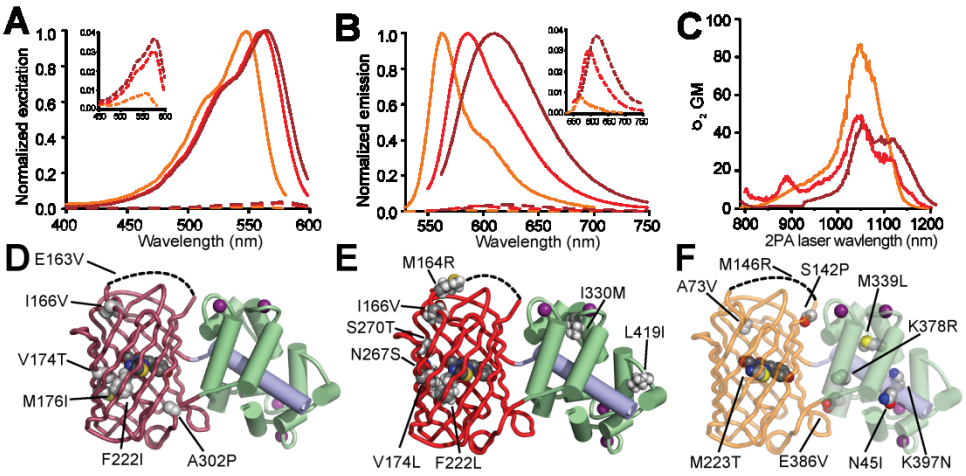

Figure 2.3. Characterization of improved indicators. (A) Excitation spectra of O-GECO1 (orange), R-GECO1.2 (red) and CAR-GECO1 (dark red) with (solid line)

and without (dashed line) Ca^{2+}. Inset: 25× y-axis zoom. (B) Emission spectra represented as in (A). (C) Two-photon excitation spectra of O-GECO1, R-GECO1 and CAR-GECO1, colored as in (A,B). (D-F) Models of: (D)CAR-GECO1; (E) R-GECO1.2; and (F) O-GECO1,showing location of substitutions relative to R-GECO1.

Table 2.2. List of substitutions for new GECOs described in this work. Residues are numbered as described in **Figure 2.4.**

Protein	Substitutions relative to R-GECO1
O-GECO1	N45I/A73V/S142P/M146R/M223T/M339L/K378R/E386V/K397N
R-GECO1.2	M164R/I166V/V174L/F222L/N267S/S270T/I330M/L419I
CAR-GECO1	E163V/I166V/V174T/M176I/F222I/A302P

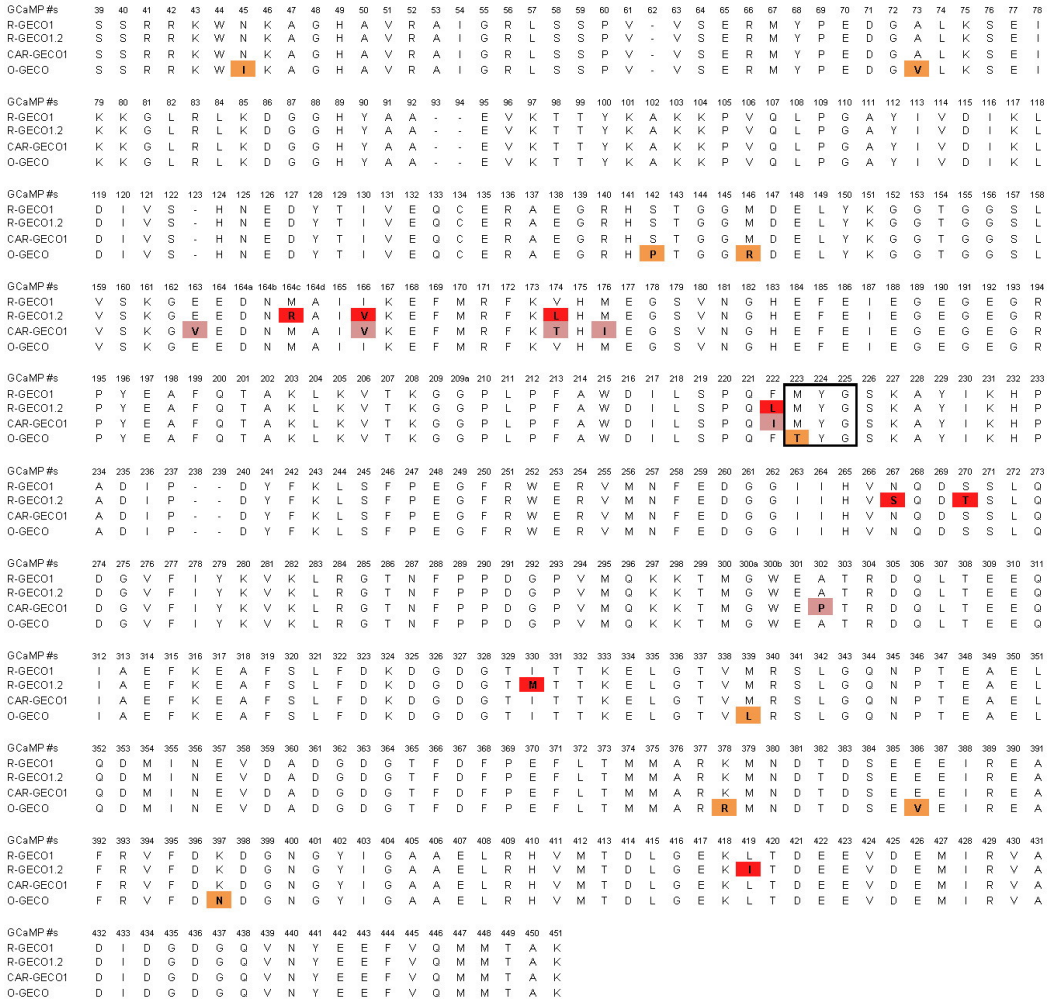

Figure 2.4. Sequence alignment of R-GECO1, R-GECO1.2, CAR-GECO1, and O-GECO1. Changes relative to R-GECO1 are shown as colored boxes. The chromophore-forming tripeptide is enclosed in a black box. Residue numbering is consistent with the crystal structure of G-CaMP2 (PDB ID 3EVR) (*96*).

Screening of the same library (i.e., randomization of positions 16 and 65) also led to the discovery of R-GECO1.1 with the Val16Leu and Phe65Leu mutations, a 27-fold intensity change, and essentially the same excitation and emission maxima as R-GECO1. Further directed evolution with library creation by error-prone PCR led to the identification of R-GECO1.2 which has 8 mutations relative

to R-GECO1 (Figure 2.3E, Figure 2.4, and Table 2.2), a 2-fold improved intensity change (33-fold) (Figure 2.3AB) relative to R-GECO1.

Similar to the strategy used to identify red-shifted variants, our efforts to generate an orange fluorescent variant were inspired by the mutations present in the orange DsRed-variant mOrange (*16*). Accordingly, we introduced the Lys163 mutation and created a gene library in which the codons for 4 positions (Met66, Phe83, Ile197, and Gln213 by DsRed numbering) were randomized to a rationally chosen codon subset. Screening of this library led to the identification of an orange fluorescent (excitation at 545 nm and emission 565 nm with Ca^{2+}) GECO variant, O-GECO0.1, with a 44-fold intensity change. Further directed evolution ultimately produced O-GECO1 with 9 mutations relative to R-GECO1 (Figure 2.3F, Figure 2.4, and Table 2.2), a fluorescence response of 146-fold, and a 2-photon cross-section of 85 GM at 1048 nm (Figure 2.3C). The large *in vitro* response of O-GECO1 is similar to that of the latest generation G-CaMP variants, G-CaMP5F (162-fold) and G-CaMP5H (158-fold) (*145*).

2.2.3 *In vitro* characterization

Systematic *in vitro* characterization revealed that CAR-GECO1 has a higher affinity to Ca^{2+} of 490 nM, while R-GECO1.2 and O-GECO1 exhibit a lower affinity to Ca^{2+} of 1200 nM and 1500 nM, respectively (Figure 2.5GHI, Table 2.1). Absorbance spectra with and without Ca^{2+} are consistent with the fluorescence spectra (Figure 2.5ABC), and they also revealed that there is a non-fluorescent chromophore species (~430 nm in O-GECO1, ~450 nm in R-GECO1.2, and CAR-GECO1) presents in the Ca^{2+}-free state in all four GECOs. This non-

fluorescent chromophore species correspond to the protonated form of the chromophore, but upon binding to Ca^{2+}, it is completely shifted to the anionic form with a higher wavelength absorbance. This change of absorbance upon Ca^{2+} binding suggests all three Ca^{2+} indicators are operated under the same mechanism. That is, in the Ca^{2+}-free state, the majority of the chromophore exists in the non-fluorescent, protonated state, and only a small amount of anionic chromophore gives the dim fluorescence; upon binding to Ca^{2+}, the conformational change of CaM and M13 alters the protonated-anionic equilibrium and shifts the chromophore to the fluorescent anionic state that leads to a increase of fluorescence. This potential mechanism is also consistent with increase of apparent pK_a among the four Ca^{2+} indicators upon binding to Ca^{2+} (Figure 2.5DEF, Table 2.1) as well as the x-ray crystal structure of R-GECO1 in the Ca^{2+}-bound state (PDB ID 4I2Y) (*146*).

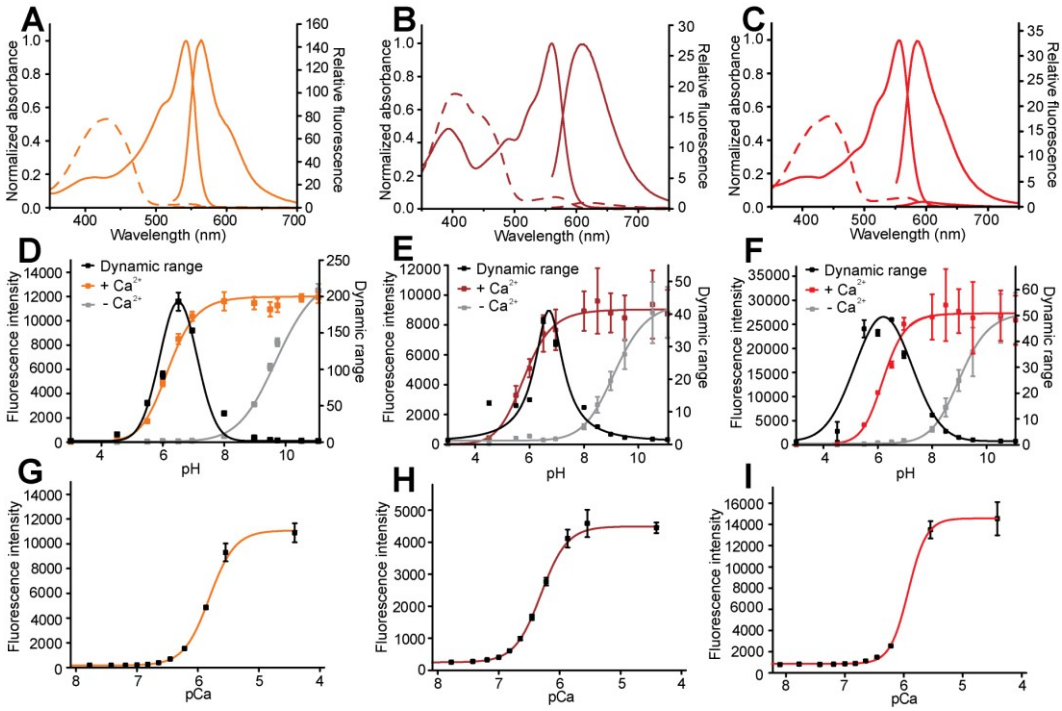

Figure 2.5. Spectral characterization of O-GECO1, CAR-GECO1 and R-

GECO1.2. (A) Absorbance and emission spectra of O-GECO1 in both the Ca^{2+}-free state (dotted line) and the Ca^{2+}-bound state (solid line). (B) Spectra for CAR-GECO1, represented as in (A). (C) Spectra for R-GECO1.2, represented as in (A). (D) Fluorescence intensity and dynamic range of O-GECO1 as a function of pH. Dynamic range is calculated by dividing fluorescence intensity of the Ca^{2+}-bound state by the intensity of the Ca^{2+}-free state. (E) Fluorescence intensity and dynamic range of CAR-GECO1, represented as in (D). (F) Fluorescence intensity and dynamic range of R-GECO1.2, represented as in (D). (G) Fluorescence intensity of O-GECO1 as a function of free Ca^{2+} concentration in buffer (10 mM MOPS, 100 mM KCl, pH 7.2). (H) Fluorescence intensity of CAR-GECO1 as a function of free Ca^{2+} concentration, represented as in (G). (I) Fluorescence intensity of R-GECO1.2 as a function of free Ca^{2+} concentration, represented as in (G).

2.2.4 Characterization in live cells

To demonstrate the utility of the new Ca^{2+} indicators, Satoko Araki from Dr. Takeharu Nagai's group in Osaka University and I performed systematic characterization of the dynamic response in HeLa cells treated with histamine to stimulate IP3-mediated release of Ca^{2+} from intracellular stores, followed by ionomycin/Ca^{2+} and ionomycin/EGTA to completely saturate and deplete intracellular stores of Ca^{2+}, respectively (Figure 2.6 and Table 2.3). Although there is a great deal of cell-to-cell heterogeneity in such experiments, averaging the results from many individual cells revealed that the improved intensity changes observed *in vitro* were preserved in cells. Of the four indicators, O-GECO1 gave the best performance in cells, exhibiting maximum fluorescence

intensity changes of 41 ± 10 fold (n = 49 cells) following treatment with histamine. Under identical conditions, R-GECO1, R-GECO1.2 and CAR-GECO1 had histamine-induced fluorescence changes of 9.2 ± 1.3, 11.2 ± 2.5 and 10.5 ± 1.8 fold, respectively (Figure 2.6 and Table 2.3).

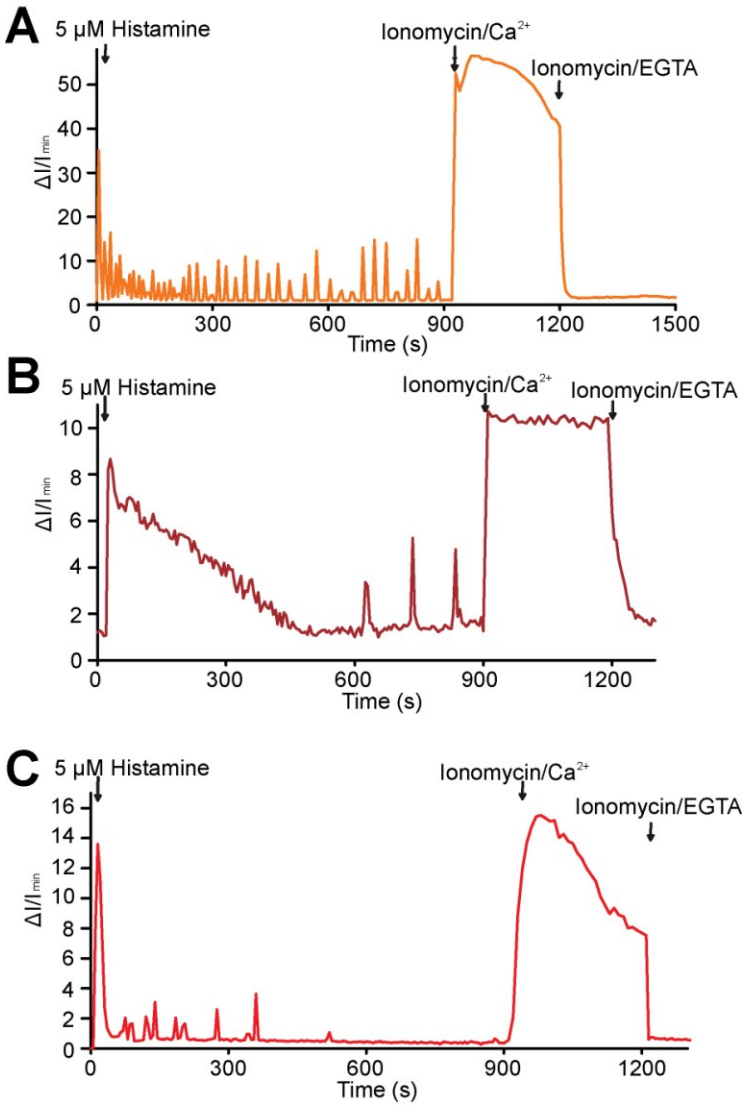

Figure 2.6. Representative intensity vs. time traces for HeLa cells transfected with: (A) O-GECO1; (B) CAR-GECO1; and (C) R-GECO1.2.

Table 2.3. Systematic characterization of the Ca^{2+}-dependent fluorescence of GECOs in HeLa cells. Cells were treated first with histamine (abb. His), then with Ca^{2+}/ionomycin (abb. Ca^{2+}), and finally with EGTA/ionomycin (abb. EGTA).

Protein	n[1]	Maximum Ca^{2+} to minimum EGTA ratio	Maximum His to minimum His ratio	Maximum His to maximum Ca^{2+} ratio
R-GECO1	22	4.9±1.9	9.2±1.3	0.98±0.15
O-GECO1	49	56.8±12.5	41.4±10.3	0.68±0.15
R-GECO1.2	39	12.4±2.3	11.2±2.5	0.68±0.16
CAR-GECO1	14	12.2±2.1	10.5±1.8	0.87±0.08

[1]Number of individual transfected cells on which systematic calibration experiments were performed.

2.2.5 Photoactivation in orange and red Ca^{2+} indicators

As the red-shifted excitation spectra of R-GECO1, R-GECO1.2, and CARGECO1 enable these Ca^{2+} indicators to be efficiently excited at wavelengths greater than 550 nm, we expected that they could be used to monitor Ca^{2+} concentration changes associated with ChR2 activation without causing unintentional additional activation of ChR2. To test this idea, Lin Liu from Dr. Wen-hong Li's group in University of Texas Southwestern Medical Center undertook a series of Ca^{2+} imaging experiments with a pancreatic islet insulinoma beta cell line, INS-1, transfected with a plasmid encoding either cytoplasmic RGECO1.2 (i.e., no targeting sequence) or R-GECO1.2 anchored to the plasma membrane with the N-terminal peptide sequence of the Src kinase Lyn (Lyn-R-ECO1.2) (*147*). For optogenetic manipulation experiments, these cells were cotransfected with a second plasmid encoding ChR2-(T159C)-EGFP (*148*). Control experiments with cells transfected with only the Ca^{2+} indicator revealed

that Lyn-R-GECO1.2 exhibited a slightly higher fluorescence intensity increase than R-GECO1.2 in response to KCl stimulated membrane depolarization and elevation of cytoplasmic and subplasmalemmal Ca^{2+} (Figure 2.7A-C) and was notably more sensitive than Fluo-3 and Lck-G-CaMP3 (Figure 2.7DE).When we imaged INS-1 cells cotransfected with plasmids encoding R-GECO1.2 (or Lyn-R-GECO1.2) and ChR2-(T159C)-EGFP (Figure 2.8AD), we found that we were able to achieve robust apparent increases in cytoplasmic and subplasmalemmal Ca^{2+} using brief episodes (20-200 ms) of blue light illumination (480-500 nm at 135 mW/cm^2) to activate ChR2(T159C)-EGFP (Figure 2.8BEGH). However, control experiments with cells expressing only R-GECO1.2 also revealed transient increases in red fluorescence during blue light illumination lasting 100 ms or longer (Figure 2.8C). This ChR2-independent increase in red fluorescence amounted to as much as 12% of the total fluorescence signal for 200 ms illumination (Figure 2.8CG). For reasons that remain unclear, the magnitude of the ChR2-independent fluorescent response was diminished in cells expressing Lyn-R-GECO1.2, and essentially indistinguishable from noise even for 200 ms illumination (Figure 2.8FH). Notably, the blue light was turned off during acquisition of the red fluorescence image, so these transient increases were not due to additional excitation power. A similar effect was observed when using R-GECO1 in combination with 440 nm activation of the Zebrafish blue opsin (*149*) coupled to the Gq signaling pathway (Figure 2.9) by Kelsey March from Dr. Thomas E. Hughes' group in Montana State University. Brief (5 ms) pulses of 440 nm blue light at high power (33 W/cm^2) consistently produced an approximate 20% increase in RGECO1 fluorescence, even in those that were not transfected with the opsin. However, upon illuminating the cell with a train of 3 or more pulses of 440 nm light, a threshold in opsin activation was crossed and a significantly

larger (80%), more persistent (10-30 s), and more heterogeneous R-GECO1 response was observed due to a Gq driven release of Ca^{2+} from intracellular stores. Akerboom *et al*. have recently reported similar observations of R-GECO1 photoactivation (*146*).

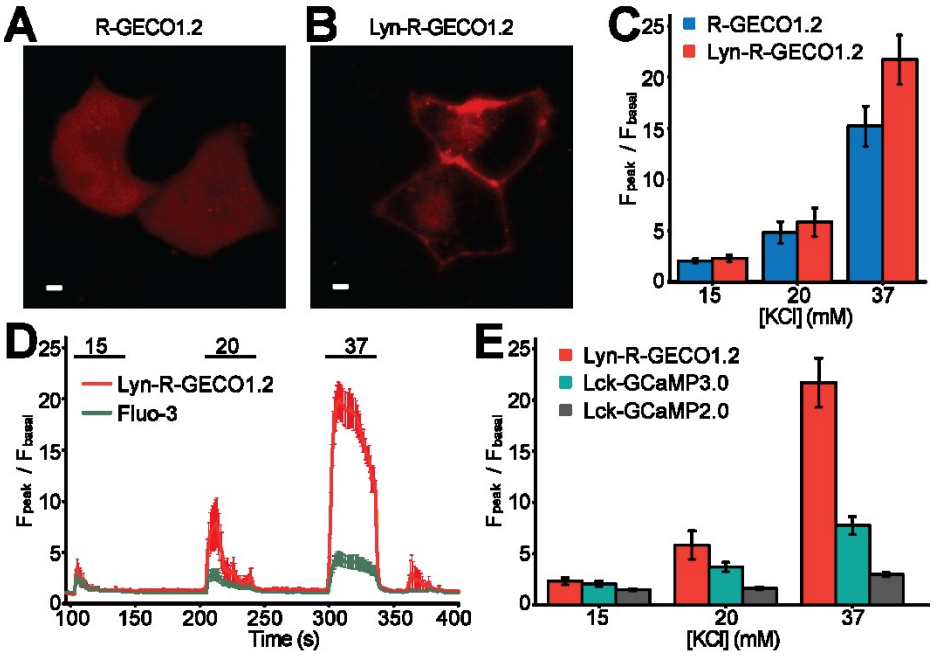

Figure 2.7. Characterization of plasma membrane targeted Lyn-R-GECO1.2.Example confocal images of INS-1 cells expressing either: (A) R-GECO1.2; or (B) Lyn-R-GECO1.2. Scale bar = 2 µm. (C) Relative to R-GECO1.2 (n = 35), Lyn-R-GECO1.2 (n = 31) shows an improved Ca^{2+} response from KCl stimulation. (D) Average time courses (n = 5) of concurrent imaging of Lyn-R-GECO1.2 and Fluo-3 in INS-1 cells. (E) Relative to Lck-G-CaMP3 (n = 15) and Lck-G-CaMP2 (n = 14), Lyn-R-GECO1.2 (n = 31) shows an improved response to changes in subplasmalemmal Ca^{2+}.

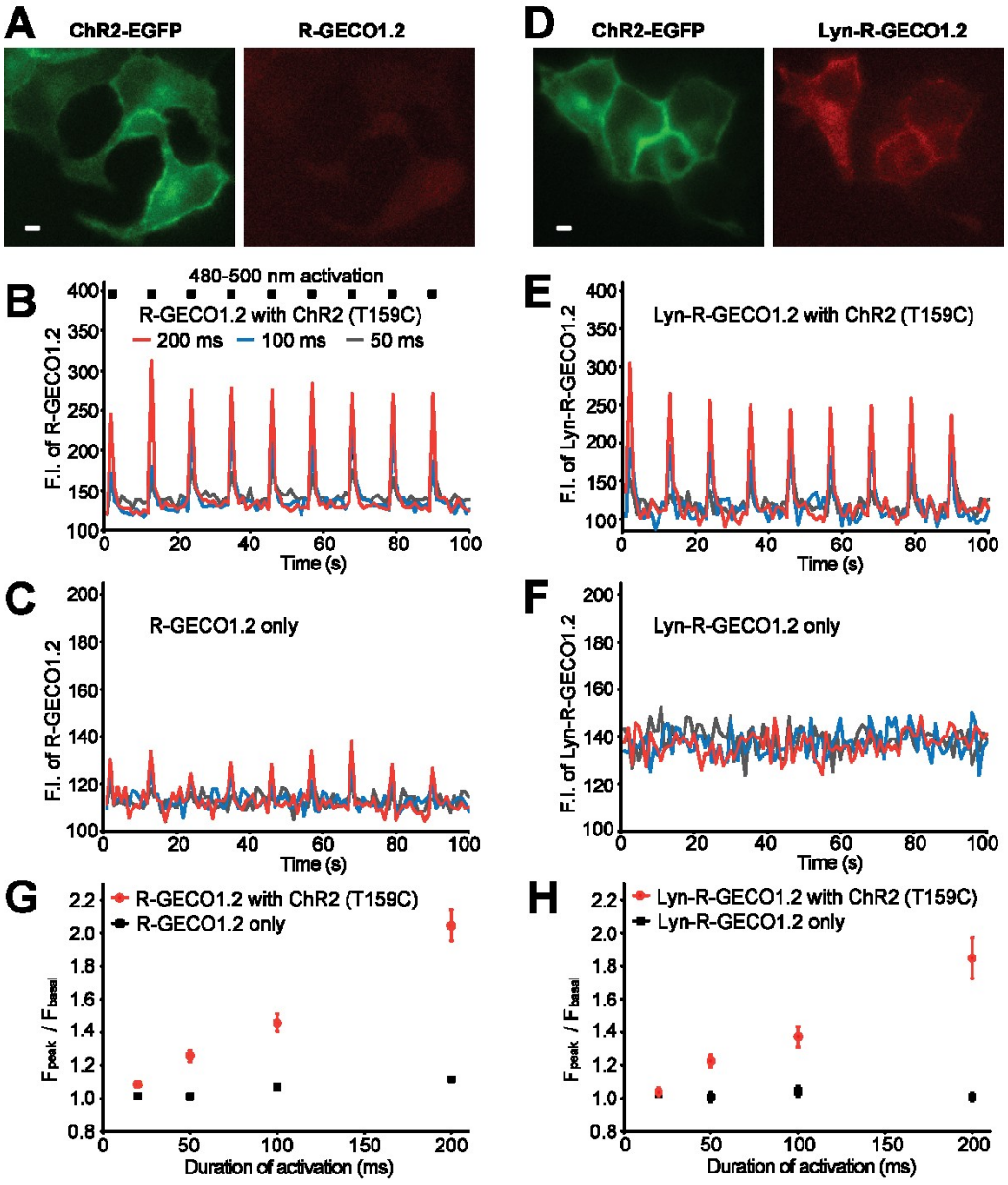

Figure 2.8. Imaging ChR2-induced Ca^{2+} transients in INS-1 cells. (A, D) Example fluorescence images of INS-1 cells expressing ChR2(T159C)-EGFP and either: (A) R-GECO1.2; or (D)Lyn-R-GECO1.2. Scale bar = 2 μm. (B, E) Fluorescence vs. time traces for cells expressing ChR2(T159C)-EGFP and either: (B) R-GECO1.2; or (E) Lyn-R-GECO1.2,during intervals of blue light irradiation (50 - 200 msec). (C, F)Fluorescence vs. time traces for cells expressing only: (C) R-

GECO1.2; or (F) Lyn-R-GECO1.2,during intervals of blue light irradiation (50 - 200 msec).(G, H) Average signal enhancements of R-GECO1.2 or Lyn-R-GECO1.2 upon increasing doses of blue light illumination in cells expressing: (G) R-GECO1.2 only(n=22) or R-GECO1.2 with ChR2(T159C)-EGFP (n=33); or (H) Lyn-R-GECO1.2 (n=18)or Lyn-R-GECO1.2 with ChR2(T159C)-EGFP (n=24).

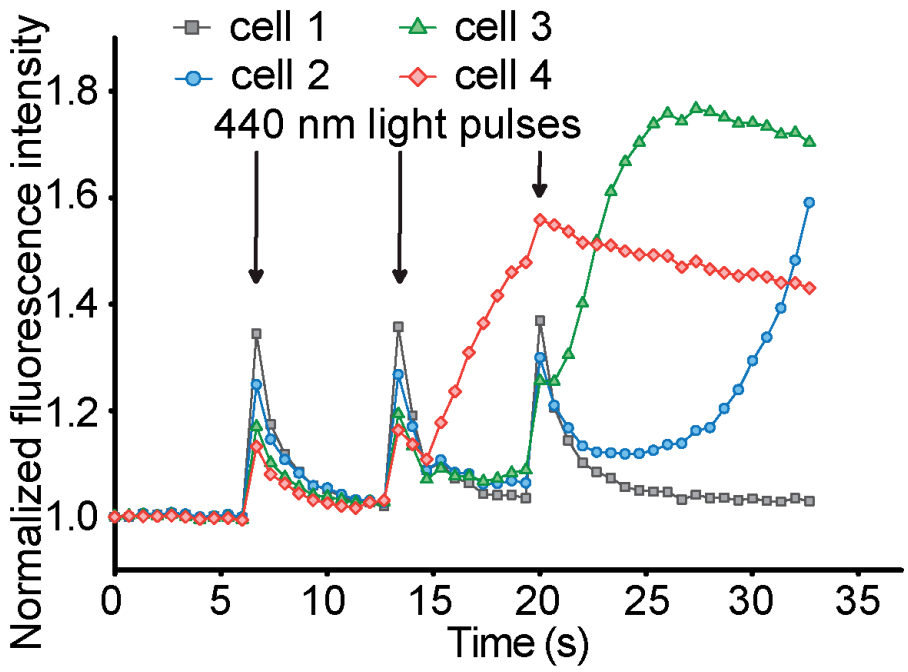

Figure 2.9. Fluorescence traces vs. time for optogenetic activation (440 nm) of HEK293 cells co-transfected with Zebrafish blue opsin, a hybrid Gq/t α subunit, and R-GECO1.

To determine if a similar combination of optogenetic activation and Ca^{2+} imaging could be achieved in intact brain tissue, Tomoki Matsuda and Yu-Fen Chang from Dr. Takeharu Nagai's group in Osaka University attempted to use

CAR-GECO1 and ChR2(T159C)-EGFP to manipulate and image intracellular Ca^{2+} in mouse neocortical slice culture. *In utero* electroporation of mice embryos at embryonic day 13 with either a vector encoding CAR-GECO1 or vectors for both CAR-GECO1 and ChR2(T159C)-EGFP, was performed. Confocal fluorescence imaging of the transfected neocortical neurons that had been born at the ventricular surface on the day of electroporation was performed 6 days later (Figure 2.10AD). Similar to our results in beta cells, Ca^{2+} elevations in cells transfected with only CAR-GECO1 showed transient increases in red fluorescence when illuminated with a 36 mW 405 nm laser at 100% power (90 $\mu J/\mu m^2$) for 1 s (Figure 2.10B). At 5% power levels (4.5 $\mu J/\mu m^2$, for 1 s), these increases in red fluorescence decreased to a level where they were practically indistinguishable from noise (Figure 2.10C). Co-transfection with plasmids for both CAR-GECO1 and ChR2(T159C)-EGFP, followed by period illumination with the 405 nm laser at 5% power, resulted in a robust CAR-GECO1 fluorescence response due to intracellular Ca^{2+} elevations (Figure 2.10F). No activation of ChR2(T159C)-EGFP was observed when transfected cells were illuminated with light from a 10 mW 561 nm laser at 50% power (12.5 $\mu J/ \mu m^2$) (Figure 2.11). Taken together, our imaging results in beta cells and neurons empirically demonstrate that, while this photoactivation phenomenon certainly complicates the use of red fluorescent Ca^{2+} indicators for use in combination with ChR2(T159C)-EGFP, it by no means prevents it. By appropriately adjusting the dosage or the duration of the light used for ChR2(T159C)-EGFP activation, it is feasible to perform optogenetic activation and Ca^{2+} imaging concurrently.

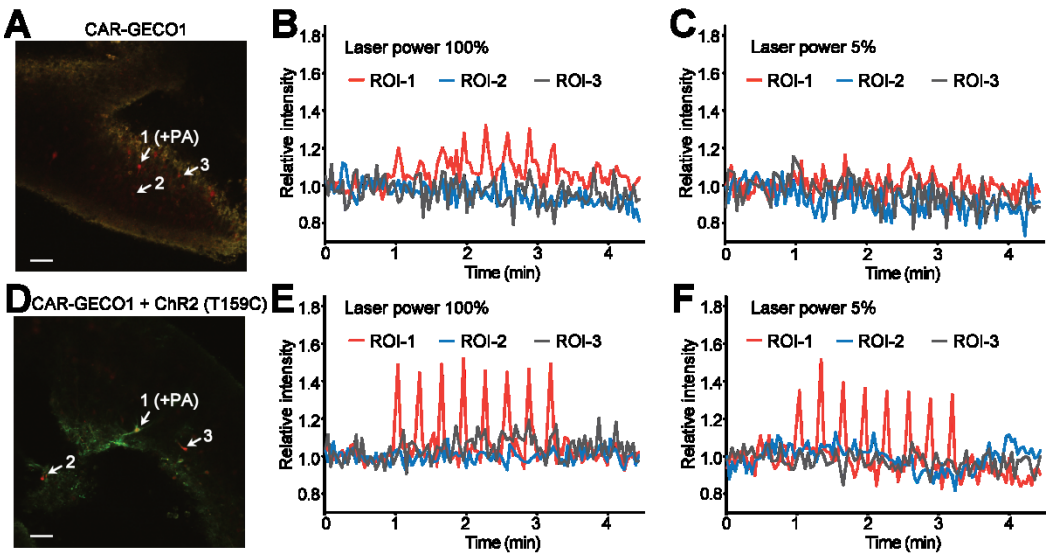

Figure 2.10. Confocal imaging of ChR2(T159C)-induced Ca^{2+} elevations in mouse neocortical slice culture. Fluorescence images and response to photoactivation light for neocortial neurons transfected with only CAR-GECO1 (A−C) or cotransfected with CAR-GECO1 and ChR2(T159C)- EGFP (D−F). Scale bar = 50 μm. (B, C) Fluorescence vs. time traces for cells transfected with only CAR-GECO1, during intervals of illumination at region of interest 1 (ROI-1) with a 405 nm laser at either 100% (90 μJ/μm^2) (B) or 5% (4.5 μJ/μm^2) (C) power. Control cells at ROI-2 and 3 were not illuminated. (E, F) Identical experimental conditions to (B, C) using tissue that has been cotransfected with CAR-GECO1 and ChR2(T159C)- EGFP. Based on the colocalization of green and red fluorescence, the neuron being photoactivated (at ROI-1) is expressing both CAR-GECO1 and ChR2(T159C)-EGFP.

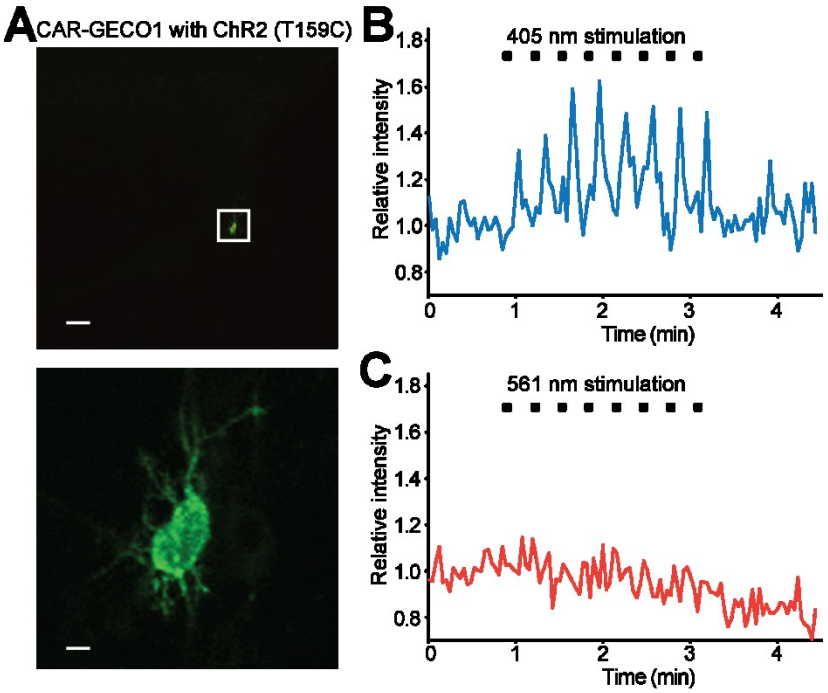

Figure 2.11. ChR2(T159C)-EGFP is activated by 405 nm illumination, but not by 561 nm illumination. (A) A neocortical neuron expressing both CAR-GECO1 and ChR2(T159C)-EGFP was identified in mouse neocortical slice culture previously transfected by electroporation. Scale bars for the upper and lower panels are 50 μm and 4 μm, respectively. (B) Fluorescence vs. time trace during intervals of illumination with a 405 nm laser with 100% power (90 μJ/μm^2). (C) Fluorescence vs. time trace during intervals of illumination with a 561 nm laser at 10% power (2.5 μJ/μm^2) for excitation and 50% power (12.5 μJ/μm^2) for stimulation.

2.2.6 Characterization of photoactivation

In an effort to obtain further insight into the mechanism of the GECO photoactivation, we undertook an *in vitro* characterization of the effect of intense violet light illumination on the fluorescence intensity of R-GECO1, R-GECO1.2, CAR-GECO1, O-GECO1, and RCaMP1.07 (*150*) Consistent with our cell imaging

results, we found that all five purified proteins exhibited substantial transient increases in the proportion of proteins in an anionic red fluorescent form upon illumination with light from a 405 nm laser at 1200 mW/cm^2 in the absence of Ca^{2+}. At physiological pH (7.2), we observed absorbance increases of 631 ± 36% for CAR-GECO1, 434 ± 22% for R-GECO1.2, 256 ± 12% for R-GECO1, 291 ± 6% for RCaMP1.07, and 249 ± 52% for O-GECO1 (Figure 2.12A-C and Figure 2.13AB). The recovery to the initial state proceeded rapidly once the 405 nm laser was turned off, and did not appear to be accelerated by illumination with longer wavelength visible light. With the exception of O-GECO1, all the rising portions (tau_{on}) of the intensity vs. time curves were well fit as monoexponential functions with tau_{on} values ranging from 0.22 ± 0.02 s to 0.31 ± 0.02 s (Table 2.4 and Figure 2.14). O-GECO1 was best fit as a biexponential function with tau_{on} values of 0.11 ± 0.04 s (major component) and 5.4 ± 1.2 s (minor component). In contrast, the falling portions (tau_{off}) for most indicators were best fit as biexponential functions, with the exception of R-GECO1.2 (tau_{off} = 0.54 ± 0.05 s), which lacked the slow minor component (tau_{off2} ~1.6 to 4.2 s) that was shared by the other GECOs.

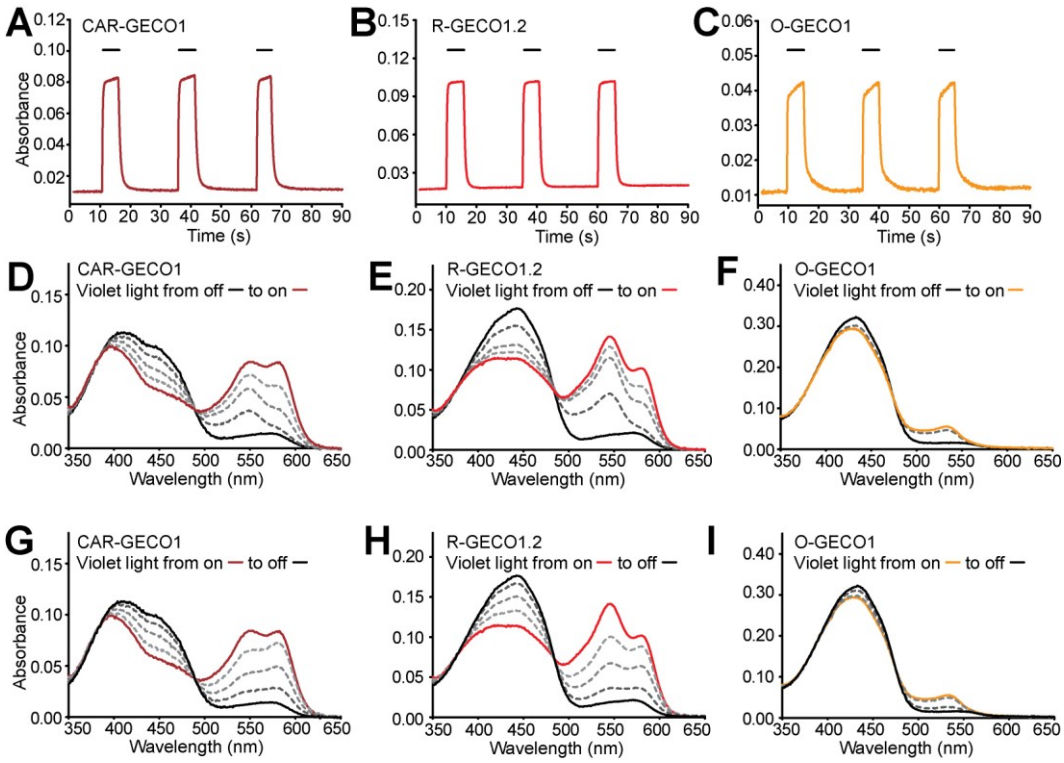

Figure 2.12. Reversible photoactivation of Ca^{2+} indicators during 405 nm illumination. Solutions of purified Ca^{2+} indicators were illuminated with a violet light laser (405 nm, 150 mW) for 5 s intervals. (A−C) Absorbance changes for the fluorescent (anionic) form of the Ca^{2+}-free state during 5 s violet light pulses (black solid line) for (A) CAR-GECO1 at 560 nm; (B) R-GECO1.2 at 570 nm; (C) O-GECO1 at 545 nm. (D−F) Transient absorbance spectra (dashed lines) acquired immediately after the onset of illumination for (D) CAR-GECO1; (E) R-GECO1.2; (F) O-GECO1. (G−I) Transient absorbance spectra (dashed lines) acquired immediately after the end of illumination for (G) CAR-GECO1; (H) R-GECO1.2; (I) O- GECO1.

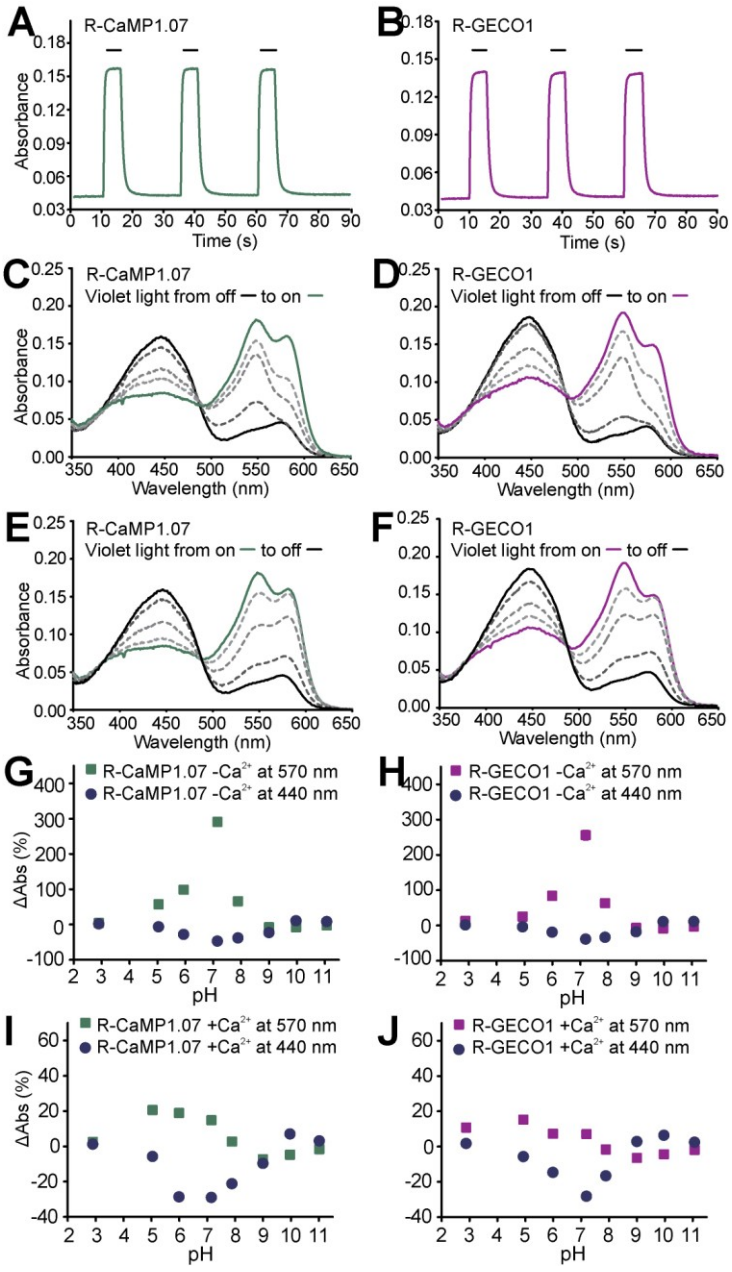

Figure 2.13. Characterization of RCaMP1.07 and R-GECO1 photoactivation. (A, B) Absorbance changes for the fluorescent (anionic) form of the Ca^{2+}-free state during 5 s violet light pulses (black solid line) for: (A) RCaMP1.07 at 570 nm; and (B) R-GECO1 at 570 nm. (C, D) Transient absorbance spectra (dashed lines) acquired immediately after the onset of illumination for: (C) RCaMP1.07; and (D) R-GECO1. (E, F) Transient absorbance spectra (dashed lines) acquired

immediately after the end of illumination for: (E) RCaMP1.07; and (F) R-GECO1. Change of absorbance in the Ca^{2+}-free state (G, H) and Ca^{2+}-bound state (I, J) with violet light (405 nm) illumination as a function of pH for: (G, I) RCaMP1.07; (H, J) R-GECO1.

Table 2.4. Kinetic characterization of photoactivation in GECOs and RCaMP1.07.

Protein	tau_{on} (s) [1]		tau_{off}(s) [2]	
	Major component (%)	Minor component (%)	Major component (%)	Minor component (%)
R-GECO1	0.31 ± 0.02 (100%)	NA[3]	0.66 ± 0.01(84%)	1.6 ± 0.1 (16%)
CAR-GECO1	0.22 ± 0.02 (100%)	NA[3]	0.60 ± 0.03(94%)	4.2 ± 0.6 (6%)
R-GECO1.2	0.23 ± 0.02 (100%)	NA[3]	0.54 ± 0.05 (100%)	NA[3]
O-GECO1	0.11 ± 0.04(86%)	5.4 ± 1.2 (14%)	0.35 ± 0.01(77%)	3.1 ± 0.2 (23%)
RCaMP1.07	0.27 ± 0.02 (100%)	NA[3]	0.68 ± 0.03(84%)	1.6 ± 0.1 (16%)

[1] O-GECO1 was best fit with a bi-exponential kinetic model, while the rest were best fit with a mono-exponential model. [2] R-GECO1.2 was best fit with a mono-exponential model, while the rest were fit with a bi-exponential model. [3] Not applicable.

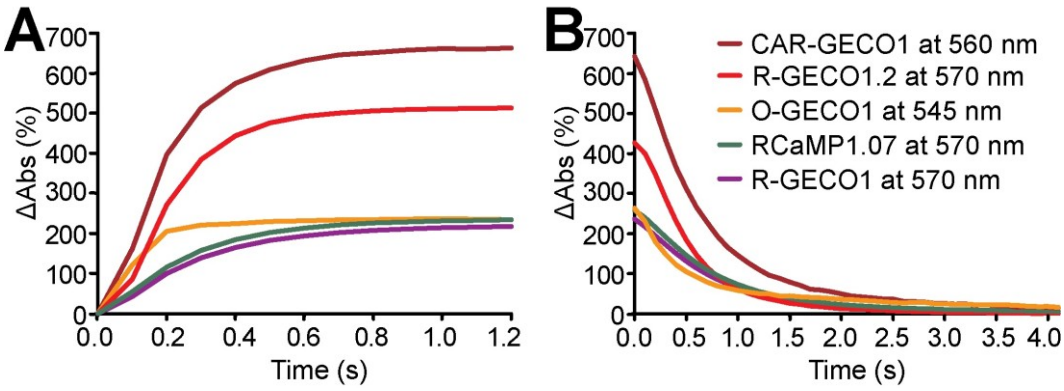

Figure 2.14. Averaged absorbance vs. time traces during photoactivation and recovery in the dark. (A) Absorbance vs. time during photoactivation. (B) Absorbance vs. time during recovery in the absence of strong blue light. Each trace is averaged from three time course measurements.

Inspection of the transient absorbance spectra revealed that the new species produced by photoactivation had a peak absorbance (λ_{max} = 545 nm) that was blue-shifted relative to R-GECO1 (and 1.2), CAR-GECO1, and RCaMP1.07, and essentially identical to that of O-GECO1 (Figure 2.12D-F and Figure 2.13CD). In all cases, formation of the new species was associated with a decrease in the proportion of the neutral, non-fluorescent form of the chromophore (Figure 2.12D-F and Figure 2.13CD). Excitation at the transiently formed 545 nm peak during photoactivation did not give rise to significant fluorescence, yet 405 nm illumination itself generated a slightly red-shifted emission peak (λ_{max} = 605 nm). For the red fluorescent GECOs, the fast increase in the 545 nm peak was followed by a slower increase in a longer wavelength absorbing species, effectively indistinguishable from normal red fluorescent state (Figure 2.12D-F and Figure 2.13CD). Upon turning the photoactivation light off, the intensity of the 545 nm peak decreased faster than that of the red fluorescent state (Figure

2.12G-I and Figure 2.13EF). For all 5 proteins, we observed that photoactivation became most significant at pH ~7, and diminished at higher and lower pH values (Figure 2.15A-C and Figure 2.13GH). The photoactivation effect was greatly diminished for the Ca^{2+}-bound states of all Ca^{2+} indicators (Figure 2.15D-F, note the y-scale difference relative to Figure 2.15A-C; and Figure 2.13IJ, note the y-scale difference relative to Figure 2.13GH), presumably because of the much smaller fraction of the protein in the neutral ground state. We observed a proportional decrease in photoactivation as the power of the 405 nm laser was decreased from 1200 to 1.2 mW/cm^2 (Figure 2.16). At laser intensities in the range of 12 mW/cm^2 or less (< 1% laser power), intensity changes for the dim Ca^{2+}-free state were limited to less than 50%.

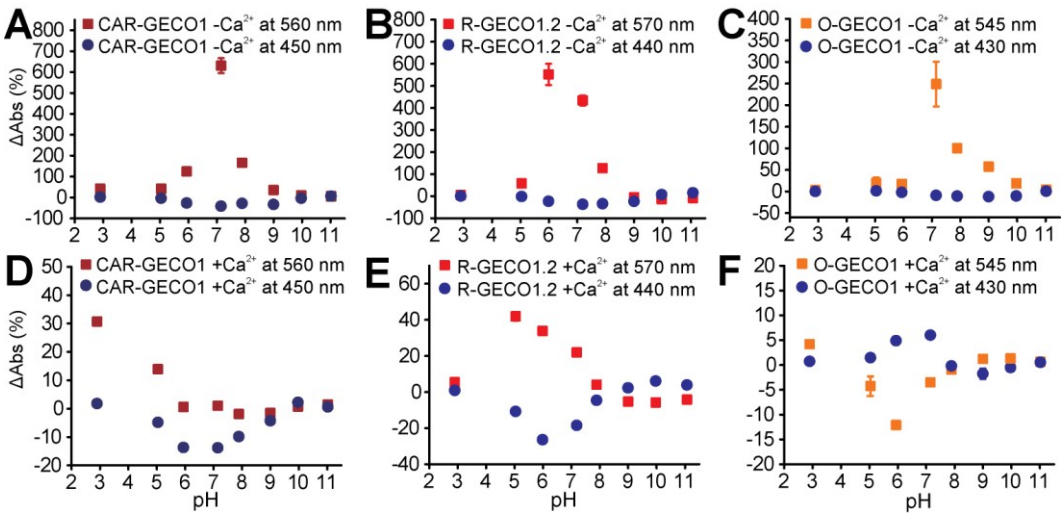

Figure 2.15. pH dependence of photoactivation of Ca^{2+} indicators. Change of absorbance in the Ca^{2+}-free state (A−C) and Ca^{2+}-bound state (D−F) with violet light (405 nm) illumination as a function of pH for: (A, D) CAR-GECO1; (B, E) R-GECO1.2; (C, F) O-GECO1.

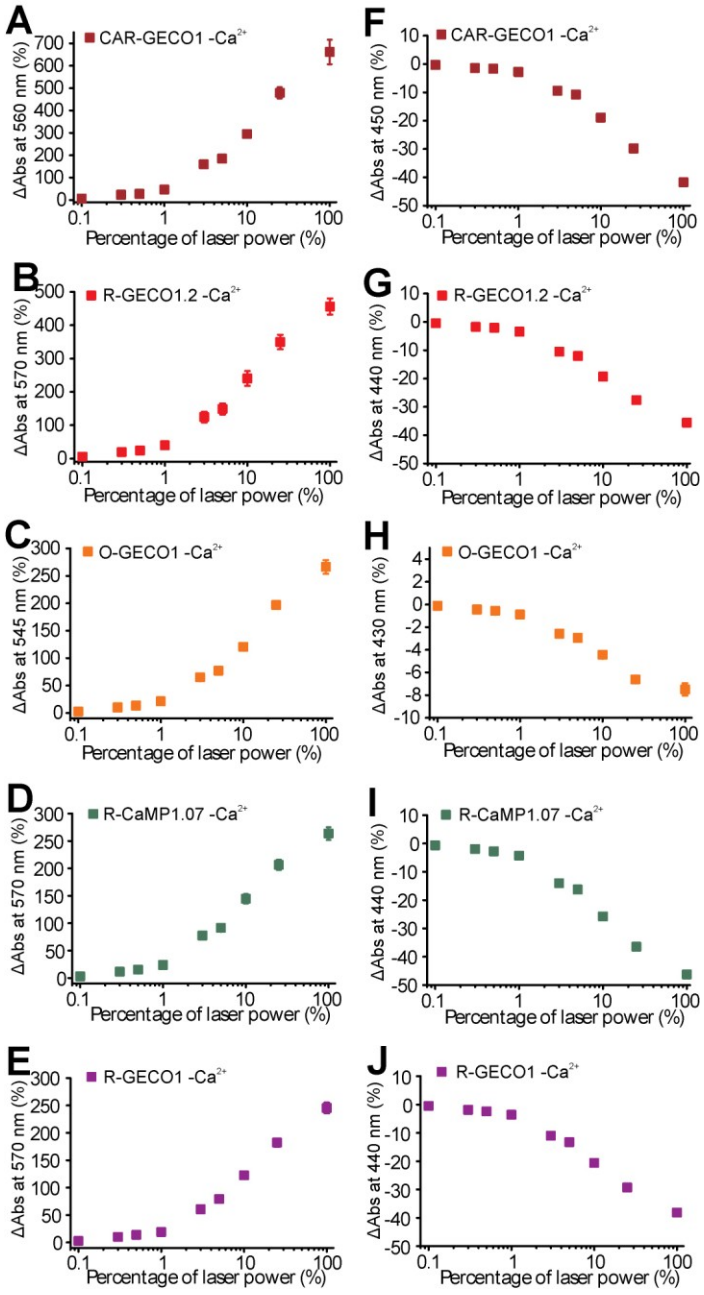

Figure 2.16. Change of absorbance for Ca^{2+} indicators in the Ca^{2+}-free state as a function of illumination power (100% = 150 mW). Change of absorbance in percent of CAR-GECO1 at 560 nm (A) and 450 nm (F); R-GECO1.2 at 570 nm (B) and 440 nm (G); O-GECO1 at 545 nm (C) and 430 nm (H); RCaMP1.07 at 570 nm (D) and 440 nm (I); and R-GECO1 at 570 nm (E) and 440 nm (J), as illumination power is varied from 0.1% to 100%.

2.2.7 A proposed model for photoactivation

The above results have led us to propose a model that captures the key features of the photoactivation phenomenon (Figure 2.17). Specifically, illumination shifts the chromophore ground state equilibrium towards a non-fluorescent anionic form that has a blue-shifted absorbance relative to the red fluorescent form that predominates at high pH and in the Ca^{2+}-bound state. This blue-shifted species then undergoes a slower conversion to the typical red fluorescent form. When illumination is turned off, this process is reversed and both the blue-shifted form (faster) and the red fluorescent form (slower) convert back to the neutral ground state form. The fact that the photoactivated form is not identical to the high pH anionic form rules out the simplest photoactivation mechanism in which violet/blue light illumination reversibly shifts the equilibrium between the protonation states of the chromophore towards the anionic form (*151*). Rather, we must turn to possible mechanisms in which the photoactivated form has an alternate structure, conformation, or microenvironment. One possibility is that violet or blue light illumination induces a *Z* to *E* isomerization of the chromophore, with the E isomer stabilized in an anionic state with a higher energy (blue shifted) absorbance. Precedent indicates that, in some cases, the *E* isomers of FP chromophore are neutral and non-fluorescent, (*47*, *152*, *153*) while in other cases they are anionic and fluorescent (*46*). Precedents also indicate that the time constants for *Z* to *E* recovery in the dark are much slower than those observed with the R-GECOs, and are typically in the range of minutes (*47*) to hours (*153*).

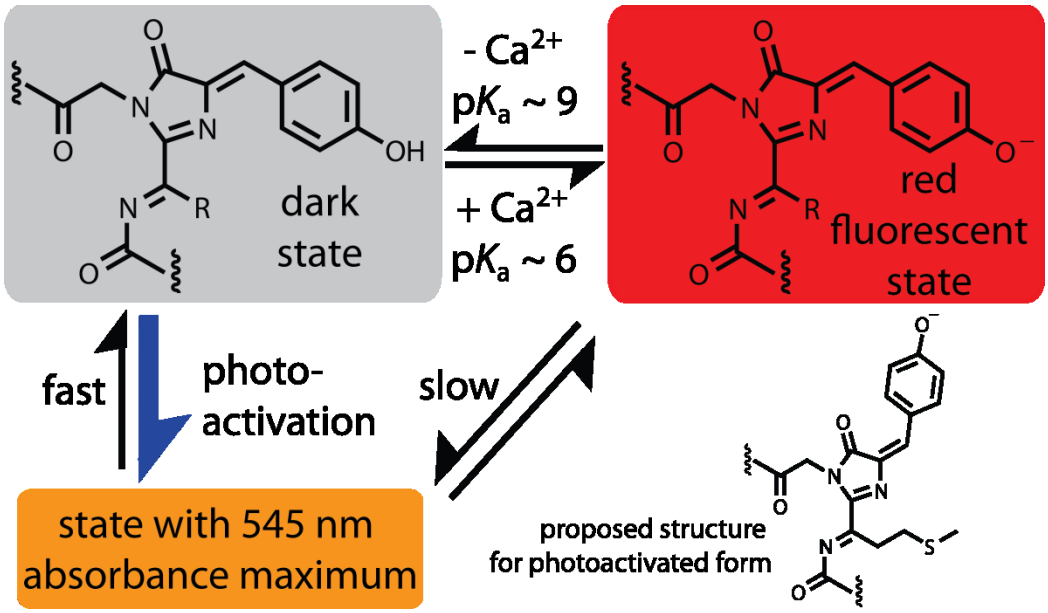

Figure 2.17. Proposed mechanism of photoactivation in red fluorescent GECOs.

An alternative photoactivation mechanism, which lacks precedent but could also explain the observed results, is that blue light illumination induces the formation of a mOrange-type chromophore structure with a third ring. In mOrange (and O-GECO1), a threonine in the first position of the chromophore-forming tripeptide forms a dihydrooxazole ring due to attack of the side chain hydroxyl group on the carbonyl moiety of the preceding residue (*154*). This cyclization decreases the conjugation of the (otherwise red fluorescent) chromophore, resulting in a blue-shifted absorption and emission. To test the possibility that photoactivation induces a similar cyclization to form a 6-member sulfonium-containing ring (Figure 2.18A) in R-GECO1, we substituted the methionine at the first position of the chromophore (position 223; Figure 2.18A) with glutamine. It is unlikely that the glutamine side chain could participate in an analogous cyclization reaction. The resulting R-GECO-M223Q variant retained its response

to Ca^{2+} and could be photoactivated (Figure 2.18B-D). We conclude that photoactivation does not involve the formation of a 6-membersulfonium-containing ring, leaving *Z* to *E* isomerization as the most reasonable explanation for the photoactivation phenomenon.

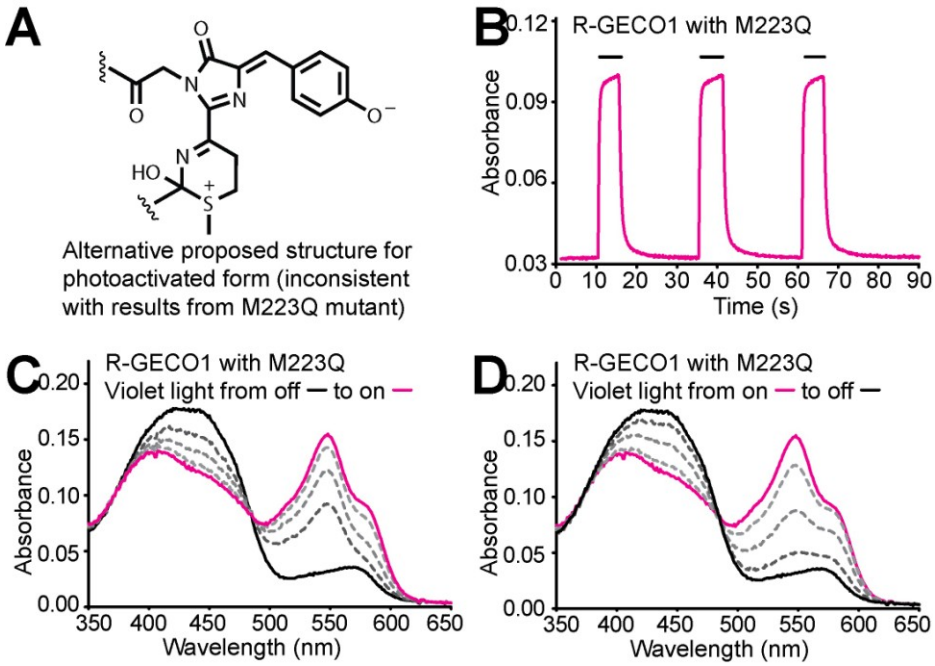

Figure 2.18. Characterization of R-GECO1-M223Q photoactivation. (A) Alternative proposed structure for photoactivated form (inconsistent with results from M223Q mutant). (B) Absorbance changes for the fluorescent (anionic) form of the Ca^{2+}-free state during 5 s violet light pulses (black solid line). (C) Transient absorbance spectra (dashed lines) acquired immediately after the onset of illumination. (D) Transient absorbance spectra (dashed lines) acquired immediately after the end of illumination.

2.3 Conclusion

In conclusion, O-GECO1, R-GECO1, R-GECO1.2, and CAR-GECO1 are engineered Ca^{2+} indicators that undergo intensiometric changes of 146-, 16-, 33-, and 27-fold, respectively. These indicators enable the detection of transient elevation in intracellular Ca^{2+} concentration with improved sensitivity but, due to an inherent ability to be photoactivated, care must be taken when red fluorescent indicators are used in conjunction with blue light illumination. Fortunately, using decreased duration or intensities of violet/blue activation light can circumvent this problem. If high power optogenetic activation with violet/blue light is unavoidable, a delay of several seconds will be required to allow the GECO fluorescence to recover to baseline. Under such circumstances, R-GECO1.2 would be the indicator of choice due to its fast tau_{off}, recovering to approximately 2% of baseline with 3.5 s. Tethering of the Ca^{2+} indictor to the inner leaflet of plasma membrane (i.e., Lyn-R-GECO1.2) also helps to mitigate the problem of photoactivation, yet this approach may be limited to the subplasmalemmal microenvironment and may not be applicable to other cellular compartments. We anticipate that these new tools will stimulate further efforts to combine the use of genetically encoded Ca^{2+} indicators and optogenetic tools for the simultaneous activation and imaging of excitable cells in different tissues including brains.

2.4 Materials and methods

2.4.1 General methods and materials

Synthetic DNA oligonucleotides used for cloning and library construction were purchased from Integrated DNA Technologies. Pfu polymerase (Thermo)

was used for non-mutagenic PCR amplifications in the buffer supplied by the respective manufacturer. Taq polymerase (New England Biolabs) in the presence of $MnCl_2$ (0.1 mM) was used for error-prone PCR amplifications. PCR products and products of restriction digests were routinely purified using preparative agarose gel electrophoresis followed by DNA isolation using the GeneJET gel extraction kit (Thermo) or QIAEX II gel extraction kit (Qiagen). Restriction endonucleases were purchased from Thermo and used according to the manufacturer's recommended protocol. Ligations were performed using T4 ligase in Rapid Ligation Buffer (Promega). Small-scale isolation of plasmid DNA was performed by GeneJET miniprep kit (Thermo) or by alkaline lysis of bacteria (a pellet derived from 1.5-3 mL of liquid culture) followed by ethanol precipitation of the DNA. Large-scale plasmid DNA purifications were performed by alkaline lysis of bacteria (a pellet derived from 150-200 mL of liquid culture) followed by successive steps of isopropanol precipitation, PEG 8000 precipitation, and 2 rounds of phenol/chloroform extraction. The cDNA sequences for all GECOs and fusion constructs were confirmed by dye terminator cycle sequencing using the BigDye Terminator Cycle Sequencing kit (Applied Biosystems).

2.4.2 Generation of improved GECOs variants

R-GECO1 in pTorPE (*144*) was used as the initial template for all engineering. Mutations of V16E, F65I, L124V and I161M were introduced by using primers mplum_V16E, mplum_F65I, mplum_L124V and mplum_I161M and the QuikChange II Site-Directed Mutagenesis Kit (Agilent Technologies). Position 16 and 65 were randomized in a single QuikChange reaction. Random mutagenesis was performed by error-prone PCR amplification. Library of potentially orange-

fluorescent GECO variants were constructed by QuikChange reactions. In this library, the codon for position 66 was DYA, the codon for position 83 was TWH, the codon for position 163 was ATG, the codon for position 197 was RDA, and the codon for position 213 was CWG, where D = A or G or T, Y = C or T, W = A or T, H = A or C or T, and R = A or G.

2.4.3 Screening of gene libraries

The imaging system used for library screening has previously been described in detail (*155*). For libraries generated by random mutagenesis, we screened 10,000-20,000 colonies (10-20 plates of bacterial colonies) per round, typically stopping screening when a number of substantially improved variants had been identified. For libraries generated by randomization of one or more codons, we screened approximately 3-fold more colonies than the expected library diversity (e.g., 12,000 colonies for a 4,000-member library). During library screening we picked colonies that exhibited the top 0.01% to 0.1% change of fluorescence intensity (or ratio) upon application of an EGTA solution (2 mM EGTA, 30 mM Tris-HCl, pH 7.4; applied using a spray bottle that produced a fine mist). In later rounds of screening, we also picked the top 0.01% to 0.1% of colonies based only on their brightness (or ratio) prior to application of EGTA. Picked clones were individually cultured in 4 mL liquid LB medium (0.0016% L-arabinose, 200 μg/ml ampicillin) that was then shaken (250 rpm) for either 36 h at 30 °C (in earlier generations) or 22 h at 37 °C (in later generations). Proteins extracted from the liquid cultures of the picked clones were subjected to a second stage of screening in a Safire2 fluorescence microplate reader (Tecan). Extraction of periplasmic protein from *E. coli* cultures was performed by a cold osmotic shock

procedure. Briefly, bacterial cells were harvested by centrifugation at 13,000 g for 2 min at 4 °C and gently resuspended in 500 µL of ice-cold pH 8.0 buffer containing 30 mM Tris·Cl, 1 mM EDTA and 20% sucrose. After 5 min of gentle agitation on ice, the bacteria were again pelleted by centrifugation (9,000 g for 5 min at 4°C), resuspended in 400 µL of ice-cold 5 mM $MgSO_4$, and gently agitated for 10 min on ice. Following centrifugation to pellet the intact bacteria (9,000 g for 5 min at 4°C), the supernatant (the osmotic shock fluid containing the periplasmic protein fraction) was collected. In cases where the periplasmic export efficiency was particularly low, cytoplasmic protein was extracted by suspension of the osmotic shock cell fraction in B-PER (Pierce) followed by centrifugation to pellet the cell debris.

The procedure for screening CAR-GECO1 libraries was essentially identical, except for the use of ratiometric imaging of the *E. coli* colonies. Colonies expressing CAR-GECO variants, grown on 10 cm Petri dishes, were illuminated by light through an 535/50 nm excitation filter, and fluorescence emission was captured through both a 610/75 nm filter and a 680/40 nm emission filter. Colonies with ratios of 680/40 nm to 610/75 nm emission intensities that were in the highest 0.1% were picked and cultured individually.

2.4.4 Characterization of orange and red Ca^{2+} indicators

To purify GECOs for in vitro spectroscopic characterization, the pTorPE plasmid harboring the variant of interest was first used to transform electrocompetent *E. coli* DH10B cells. Following selection on LB/ampicillin (200 µg/ml), single colonies were picked and used to inoculate 4 mL LB medium (200

μg/ml ampicillin, 0.0016% L-arabinose). Bacterial cultures were shaken at 250 rpm and allowed to grow for 40 h at 30 °C. Bacteria were harvested by centrifugation (10,000 g for 5 min), resuspended in 30 mM Tris-HCl buffer (pH 7.4), lysed by French press, and clarified by centrifugation at 13,000 g for 45 mins at 4°C. Proteins were purified from the cell-free extract by Ni-NTA affinity chromatography (Agarose Bead Technologies). Purified proteins were dialyzed into either 30 mM Tris, 150 mM NaCl, pH 7.4 or 10 mM MOPS, 100 mM KCl, pH 7.2.

Absorption spectra were recorded on a DU-800 UV- visible spectrophotometer (Beckman) and fluorescence spectra were recorded on either a Safire2 platereader (Tecan) or a QuantaMaster spectrofluorometer (Photon Technology International).

For determination of fluorescence quantum yield, mOrange was used as a standard for O-GECO1, and mCherry for R-GECO1, R-GECO1.2 and CAR-GECO1. Briefly, the concentration of protein in a buffered solution (30 mM MOPS, pH 7.2, with either 10 mM EGTA or 10 mM Ca-EGTA) was adjusted such that the absorbance at the excitation wavelength was between 0.2 and 0.6. A series of dilutions of each protein solution and standard, with absorbance values ranging from 0.01 to 0.05, was prepared. The fluorescence spectra of each dilution of each standard and protein solution were recorded and the total fluorescence intensities obtained by integration. Integrated fluorescence intensity vs. absorbance was plotted for each protein and each standard. Quantum yields were determined from the slopes (S) of each line using the equation: $\Phi protein = \Phi standard \times (Sprotein/Sstandard)$.

Extinction coefficients were determined by first measuring the absorption spectrum of each GECO in Ca^{2+}-free buffer (30 mM MOPs, 100 mM KCl and 10 mM EGTA at pH 7.2) and Ca^{2+}-bound buffer (30 mM MOPS, 100 mM KCl and 10 mM Ca-EGTA at pH 7.2). The protein concentrations were determined by measuring the absorbance following alkaline denaturation and assuming ε = 44,000 $M^{-1}cm^{-1}$ at 446 nm. For R-GECO, the protein concentration was determined by comparing the absorption peak for denatured R-GECO to that of denatured mCherry (determined to have ε = 38,000 $M^{-1}cm^{-1}$ at 455 nm) following alkaline denaturation of both proteins. Extinction coefficients of each protein were calculated by dividing the peak absorbance maximum by the concentration of protein.

To determine the apparent pK_a for each GECO, a series of phosphate-free buffers was prepared as follows. A solution containing 30 mM trisodium citrate and 30 mM borax was adjusted to pH 11.5 and HCl (12 M and 1M) was then added dropwise to provide solutions with pH values ranging from 11.5 to 3 in 0.5 pH unit intervals. The pH titration of Ca^{2+}-free protein were performed by adding 1 µL of concentrated protein in Ca^{2+}-free buffer (30 mM MOPS, 100 mM KCl, 10 mM EGTA, at pH 7.2) into 100 µL of each of the buffers described above. The pH titration of the Ca^{2+}-bound protein was performed by adding 1 µL of protein in Ca2+ containing buffer (30 mM MOPS, 100 mM KCl and 10 mM $CaCl_2$, pH 7.2) into 100 µL of the pH buffers. The fluorescence of each GECO in each buffer condition was recorded using a Safire2 multiwell fluorescence platereader (Tecan).

Two-photon absorption spectra and cross sections were measured using a previously described method and optical setup (*156*). Briefly, femtosecond

Optical Parametric Amplifier (TOPAS-C, Light Conversion) was used for two-photon excitation of fluorescence. Fluorescence signal was collected from the first millimeter of the sample solution, contained in 1 cm optical cuvette. Two-photon absorption spectral profiles were measured relative to Styryl 9M in chloroform in the 1090 to 1200 nm region and relative to Rhodamine B in methanol in the 780 to 1080 nm region. Two-photon cross sections were obtained relative to Rhodamine B in methanol at 1050 and 1114 nm in independent experiments. The concentration of chromophores was determined using peak extinction coefficients and the Lambert-Beer law.

2.4.5 *In vitro* characterization of photoactivation

For characterization of photoactivation in GECOs and RCaMP1.07, purified proteins were diluted to an absorbance value in the range of 0.1-0.5 in a buffered solutionwith a pH value ranging from 3 to 11. Kinetics experiments were performed using a UV-Visible spectrometer (Agilent 8453 Spectrophotometer). Purified proteins samples in buffered pH solutions were illuminated by a 150 mW (1200 mW/cm^2) 405 nm laser (Changchun New Industries Optoelectronics Tech. Co., LTD.) 3 times with a duration of 5 s each time during a kinetic measurement. When measuring photoactivation with different light source power, neutral density filters (2000a UVND, Chroma) were used while the rest of experimental conditions were kept the same.

2.4.6 Construction of mammalian expression plasmids

To construct mammalian expression plasmids, pTorPE containing O-GECO1, R-GECO1, R-GECO1.2 or CAR-GECO1 were used as the initial templates. PCR amplification of the GECO gene was performed. PCR products were purified by gel electrophoresis in 1% agarose gel (Agarose S, Nippon Gene Co.). Gel extractions were carried out with the GeneJET gel extraction kit (Thermo). The resulting products were subjected to digestion with the BamHI and EcoRI restriction enzymes, and purified as described above for PCR products. The resulting DNA fragments were ligated with a modified pcDNA3 plasmid (*144*) that had previously been digested with the same two enzymes. To construct the plasmid for expression of CAR-GECO1 in brain slices, the pEFx vector (constructed by replacement of the CMV-enhancer and β-actin promoter of pCAGGS with the human elongation factor 1α (EF1α) promoter) (*157*) was digested with BamHI and EcoRI and ligated with the CAR-GECO1 gene fragment cut from the pcDNA3 plasmid with the same enzymes. The pEFx vector enabled us to achieve high levels of CAR-GECO1 expression in brain slices. DNA sequencing was used to verify the inserted gene sequences, and large scale plasmid preparations to produce sufficient plasmid DNA for mammalian cell transfections was carried out as previously described (*144*).

To generate Lyn-R-GECO1.2, R-GECO1.2 plasmid was digested with Kpn1 and BamH1. Oligos containing Lyn sequence (sense or antisense) and Kpn1 or BamH1 restriction sites were ligated with the digested plasmid. To construct ChR2(T159C)-EGFP, ChR2(T159C) was PCR-amplified from vector pCI-Synapsin-ChR2(T159C) using primers containing EcoR1 and BamH1 restriction

sites. The amplified product was then ligated with EGFP-N1 that has been digested with EcoR1 and BamH1.

2.4.7 HeLa cell culture and imaging

HeLa cells (40-60% confluent) on collagen-coated 35 mm glass bottom dishes (Mastumami) were transfected with 1 μg of plasmid DNA and 4 μL Lipofectamine 2000 (Life technologies) according to the manufacturer's instructions. After 2 h incubation the media was exchanged to Dulbecco's Modified Eagle Medium (DMEM) with 10% fetal bovine serum (FBS) and the cells were incubated for an additional 24 h at 37 °C in a CO_2 incubator. Immediately prior to imaging, cells were washed twice with Hank's Balanced Salt Solution (HBSS) and then 1 ml of 20 mM HEPES buffered HBSS (HHBSS) was added.

Cell imaging was performed with an inverted microscope (Eclipse Ti-E, Nikon) equipped with a digital CCD camera (ORCA-R2, Hamamatsu Photonics K.K.), a micro scanning stage (MSS-BT110, Chuo Precision Industrial Co. Ltd.), and an incubator system (Chamlide IC, Live Cell instrument). The AquaCosmos software package (Hamamatsu Photonics K.K.) was used for automated microscope and camera control. For determination of the dynamic range of new indicators in live cells, cells were imaged with a 40× oil objective lens (NA 1.3), excitation light intensity was decreased to 1% with a neutral density filter (ND100), and a 0.6× relay lens was attached before CCD camera. We used the following combinations of excitation filters, dichroic mirrors and emission filters, respectively: 534/20 nm, 552 nm, and 572/28 nm for O-GECO1; and 562/40 nm, 593 nm, and 624/40 nm for R-GECO1, R-GECO1.2 and CAR-GECO1. All filters

were purchased from Semrock and had part numbers FF01-534/20-25, FF552-Di01-25.36, FF01-572/28-25, FF01-562/40-25, FF593-Di02-25.36, and FF01-624/40-25. Imaging was performed at room temperature.

For imaging of histamine-induced Ca^{2+} dynamics, 500 ms exposure images (2×2 binning) were acquired every 5 s for 15 min. Approximately 30 s after the start of the experiment, histamine (500 μM in PBS, 10 μL) was added to a final concentration of 5 μM. After 15 min of imaging, cells were washed twice with HBSS and then incubated for 10 min in 1 mL HHBSS to allow histamine-induced oscillations to subside. Cells were then once again imaged as described above, with exposures every 10 s for a duration of 5 min. Approximately 30 s after the start of the imaging, 1 mL of 2 mM $CaCl_2$, 10 μM ionomycin in Ca^{2+}- and Mg^{2+}-free HHBSS (HHBSS(-)) was added to the dish via peristaltic pump (AC-2110, ATTO). After 5 min of imaging, cells were washed 3 times with HHBSS(-), 1 mL of 1 mM EGTA and 5 μM ionomycin in HHBSS(-) was added to the media, and cells were imaged once again with exposures every 5 s for a duration of 5 min.

2.4.8 Ca^{2+} imaging of R-GECO1.2 and ChR2 activation in INS-1 cells

INS-1(832/13) cells were seeded on 35-mm glass bottom imaging dishes (MatTek) and transfected 24 h later with R-GECO1.2 with or without ChR2(T159C)-EGFP by Metafectene (Biontex) according to the manufacturer's instructions. Cells were then cultured for additional 24 hours before imaging. Photoactivation and imaging were carried out on an inverted wide-field fluorescence microscope (Axiovert 200, Carl Zeiss) through a 63x oil objective (NA 1.25). Fluorescence excitation was controlled by a Lambda DG4 exciter (Sutter Instrument) equipped with a 175-watt Xenon lamp (PerkinElmer,

PE175BF). To activate ChR2(T159C)-EGFP, or to image Fluo-3 or G-CaMP, a band-pass filter (S490/20x, Chroma) was used to provide excitation light at the intensity of 135 mW/cm^2 (measured immediately above the objective lens using a LI-190 quantum sensor and a LI-250A light meter (LI-COR Biosciences)). Fluorescence emissions from R-GECO1.2 (605 $\pm$ 26 nm), Fluo-3 or G-CaMP (525 $\pm$ 18 nm) were collected using an EMCCD camera (iXon3 897, Andor).

2.4.9 Light driven Gq activation

The hybrid Gq/t α subunit was a chimeric Gq subunit in which the last C-terminal 18 amino acids of Gq were replaced with Gt. This is a commonly used strategy for converting receptor specificity of a particular α subunit (*158*). To create the Gq/t hybrid, a series of PCR primers were designed to amplify the coding region of Gq and replace the C-terminal 18 amino acids of Gq with Gt. The final PCR product was cloned in the CMV expression plasmid pUB2.1 (Addgene plasmid 40728) using an InFusion joining reaction (Clontech, Mountain View, CA). HEK 293 cells were cotransfected with CMV expression plasmids carrying the Zebrafish blue opsin, the hybrid Gq/t α subunit, and the R-GECO1 calcium sensor using Lipofectamine 2000 (Life Technologies, Grand Island, NY) following the manufacturer's recommended protocol. Time lapse imaging was done with an Olympus IX70 inverted microscope fitted with computer controlled filter wheel and shutter (Sutter Instrument, Novato, CA) in the excitation path. A Retiga camera (Surrey, BC, Canada) and a 40× objective lens were used to collect the images. An Exfo light source (Mississauga, Ontario, Canada) with a metal halide lamp provided the excitation light. A 440/20 excitation filter was used to activate the Zebrafish blue opsin, and a 556/20 excitation filter was used to

excite the R-GECO1. The dichroic and emission filters were from Semrock (Rochester, NY) “Pinkel” set (GFP/DsRed-2X-A-000).

2.4.10 Ca^{2+} imaging with ChR2 activation in mice brain slices

For imaging of cultured mice brain slices, pallium tissue of day 13 embryos of ICR strain mice was electroporated with plasmids (pEFx/CAR-GECO1 and pEF-1/ChR2(T159C)-EGFP) using a CUY21 electroporator (Nepagene) and an applied voltage of 30 V as previously described (*159*, *160*). Cerebral walls were isolated from the electroporated embryos 6 days later and were sliced (300 μm), embedded in collagen gel (*161*), and imaged in artificial cerebrospinal fluid containing NaCl (125 mM), KCl (5 mM), NaH_2PO_4 (1.25 mM), $MgSO_4$ (1 mM), $CaCl_2$ (2 mM), $NaHCO_3$ (25 mM), and glucose (20 mM) at pH 7.4. All images were obtained with confocal upright microscope (A1R, Nikon) equipped with a 25× water immersion lens (NA 1.10, Nikon) (*160*). Light from a 36 mW 405 nm diode laser was used to activate ChR2(T159C)-EGFP, and CAR-GECO1 was imaged with excitation with a 10 mW 561 nm laser and collection of fluorescence through a 570–620 nm bandpass filter. Expression of ChR2(T159C)-EGFP was confirmed by EGFP florescence excited by a 488 nm laser.

For imaging neocortical neurons in mice brain slices, images were first acquired with 561 nm laser excitation at 10% power (2.5 $\mu J/\mu m^2$) for 1 min. Samples were then stimulated for 1 s, by 405 nm laser at 100% (90 $\mu J/\mu m^2$) or 5% (4.5 $\mu J/\mu m^2$) power, or by 561 nm laser with 50% power (12.5 $\mu J/\mu m^2$). Following stimulation, images were acquired with 561 nm laser excitation at 10% power

(2.5 μJ/μm^2) for 15 s. This 1 s stimulation and 15 s acquisition process were repeated 7 more times. Finally, the samples were imaged by 561 nm laser with 10% power (2.5 μJ/μm^2) for 1 min.

Chapter 3 Development of a long Stokes shift red fluorescent protein Ca^{2+} indicator for 2-photon and ratiometric imaging[3]

[3] A version of this chapter has been submitted for publication as J. Wu, A. S. Abdelfattah, L. S. Miraucourt, E. Kutsarova, A. Ruangkittisakul, H. Zhou, K. Ballanyi, G. Wicks, M. Drobizhev, A. Rebane, E. S. Ruthazer, and R. E. Campbell, "A long Stokes shift red fluorescent protein Ca^{2+} indicator for 2-photon and ratiometric imaging". I was responsible for the concept formation, rational design, directed evolution, the majority of in vitro characterization, imaging in HeLa cells and dissociated neurons, data collection and analysis as well as composition of the manuscript.

3.1 Introduction

In the past two decades, many advances in neuroscience have been propelled forward by the use of 2-photon excitation fluorescence microscopy. As one of the most powerful imaging techniques for probing neuronal dynamics, genetically encoded Ca^{2+} indicators also show great promise in 2-photon excitation microscopy applications (*142*). Recently, we reported the development and subsequent improvement of a series of new genetically encoded Ca^{2+} indicators that enable imaging of Ca^{2+} dynamics in a single cell with multiple spectrally distinct colors (*144*, *162*). Of these new colors, red fluorescent indicators have the greatest potential to challenge the latest generation of highly optimized GCaMP variants as the preferred tool for *in vivo* imaging. The versatility of red Ca^{2+} indicators has been demonstrated in various tissues and organisms including the retinotectal system in zebrafish (*163*), mushroom body neurons in *Drosophila* (*164*, *165*) and chicken spinal cord (*166*).

Relative to more blue shifted fluorophores, red fluorophores have the intrinsic advantages of requiring longer wavelength excitation light that is associated with deeper tissue penetration, lower autofluorescence, and lower phototoxicity. These favorable trends continue with wavelengths extending into the NIR optical window (650 to 1000 nm), where light penetrates the furthest into mammalian tissue due to minimal absorption by hemoglobin and water (*167*, *168*). Despite substantial efforts to push RFPs (and RFP-based Ca^{2+} indicators (*162*)) to ever-longer excitation and emission wavelengths, even the most red-shifted of the RFPs have negligible 1-photon absorbance at wavelengths of 650 nm or above (*169*). An alternative approach to excite visible fluorophores is 2-photon excitation (*170*) at NIR wavelengths that are approximately double (half

the energy) the 1-photon excitation maximum. However, since RFPs tend to have 1-photon excitation peaks at 580-600 nm, their 2-photon cross section maxima typically lie beyond 1000 nm (*171*). At these wavelengths non-zero absorption by water can lead to undesirable tissue heating, and, importantly, these wavelengths are outside of tuning range of many commercial Ti-sapphire lasers. A solution to this problem is to develop long Stokes shift RFPs and RFP-based Ca^{2+} indicators with 1-photon excitation maxima at ~460 nm and 2-photon excitation ~920 nm. In this way, the combined advantages of both NIR excitation and red fluorescence emission can be realized.

Most GCaMP-type indicators, and all of the red fluorescent ones reported to date, respond to Ca^{2+} with an intensiometric response. That is, the fluorescence increases at a particular wavelength in response to an increase in Ca^{2+} concentration. However, for many applications it is desirable to have a ratiometric response where an increase in intensity at one wavelength is associated with a decrease at another. Indeed, a ratiometric response is inherent to all FRET-based Ca^{2+} indicators with a fluorescent acceptor, making these indicators more suitable for quantitative measurements due to decreased susceptibility to concentration differences and random instrumental deviations that affect both channels equally (*3*, *74*). Both excitation and emission ratiometric green fluorescent GCaMP-type indicators have been reported (*1*, *144*), and have proven useful in *Xenopus* embryos (*172*), zebrafish larvae (*173*) and mouse cortical neurons (*174*). To realize the advantages of both a red emission wavelength and a ratiometric response, it would be preferable to have a red fluorescent ratiometric Ca^{2+} indicator.

One strategy to develop such a ratiometric red Ca^{2+} indicator is to engineer an ESPT pathway, such as that found in mKeima (*62*), into an existing

intensiometric red Ca^{2+} indicator. It has been reported that ESPT can be engineered into red FPs, such as mKate, by introducing an acidic Glu or Asp residue at position 160, which is in close proximity to the phenol group of the chromophore (*175*). The side chain of the acidic residue destabilizes the anionic phenolate form (absorbance ~580 nm; fluorescence ~600 nm) and thereby helps maintain the chromophore in the neutral phenol form (absorbance ~460 nm; typically non-fluorescent) at physiological pH. Illumination with ~460 nm light leads to formation of the excited state of the phenol form which is associated with a decreased pK_a. Accordingly, the proton is transferred from the phenol to the proximal acidic group, and the anionic chromophore emits its characteristic red fluorescence (*176*).

Inspired by the X-ray crystal structure of the intensiometric Ca^{2+} indicator R-GECO1 (PDB ID 4I2Y) (*146*), we reasoned that we could engineer it to undergo Ca^{2+}-dependent ESPT. We expected that this would produce a long Stokes shift red fluorescent Ca^{2+} indicator with 2-photon excitation in the NIR window and an excitation ratiometric response. Here, we describe our successful effort to develop, characterize, and validate a red excitation ratiometric genetically encoded Ca^{2+} indicator for optical imaging (REX-GECO).

3.2 Results and discussion

3.2.1 Initial engineering of REX-GECO0.1

Our design for engineering a ratiometric red Ca^{2+} indicator was inspired by reports of engineered monomeric RFPs with large Stokes shift (*175*, *176*). Inspection of the X-ray crystal structure of R-GECO1 (PDB ID 4I2Y) (*146*) (Figure 3.1) revealed three residues (Ser64, Lys80 and Ile116; GCaMP numbering as in

the PDB file 3EVR (*96*); Figure 3.2) that were near the phenolate moiety of the chromophore of R-GECO1 in the Ca^{2+}-bound state. We reasoned that each of these residues could reasonably serve to stabilize the phenol form and act as an excited state proton acceptor if mutated to an acidic residue. Lys80 was the most promising position due to its direct electrostatic interaction with the phenolate moiety. To test our hypothesis, we created a genetic library in which the codons for Ser64, Lys80 and Ile116 were simultaneously randomized using a codon subset that encoded for a total of 624 different variants. This library was expressed in the pTorPE periplasmic expression vector (*144*), and thoroughly screened in a colony imaging format by looking for colonies that exhibited long Stokes shift red fluorescence (excitation at 438/24 nm and emission 609/57 nm). This screening led to the identification of an excitation ratiometric variant, designated as REX-GECO0.1, which harbored the Lys80Glu mutation. REX-GECO0.1 exhibits an excitation peak at ~575 nm (i.e., the phenolate form) in the Ca^{2+}-free state, but upon binding to Ca^{2+}, this peak decreases and a long Stokes shift excitation peak arises at ~480 nm (i.e., the phenol form). The excitation ratio (*R* = red intensity with excitation at 450 nm divided by the red intensity with excitation at 580 nm) increased 6.5-fold (R_{+Ca}/R_{-Ca} - 1) upon binding to Ca^{2+}.

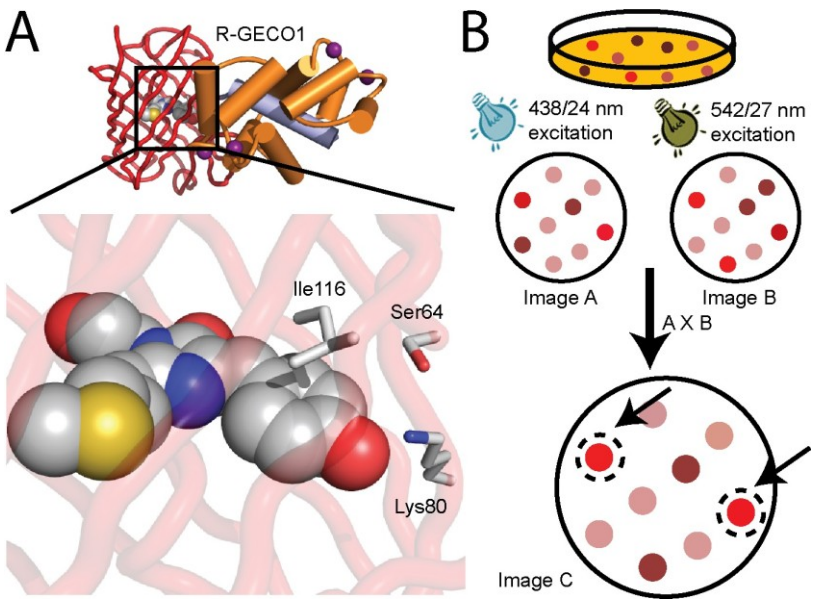

Figure 3.1. Structure of R-GECO1 and screening scheme for REX-GECO. (A) Overall structure of R-GECO1 (PDB ID 4I2Y) and zoom in on its chromophore. The side chains of 3 proximal residues, Ser64, Lys80 and Ile116, are shown in stick format (*146*). Residue numbering is consistent with the crystal structure of G-CaMP2 (PDB ID 3EVR) (*96*). (B) Screening scheme to identify excitation ratiometric red fluorescent variants. *E. coli* colonies expressing REX-GECO variants were illuminated using either 438/24 nm or 542/27 nm light, and a red fluorescent image using 609/57 nm filter was acquired. The two resulting images were then multiplied to generate a third image in which colonies with strong moderate to strong intensity under both illumination conditions had the highest combined intensity. These colonies were selected for further testing.

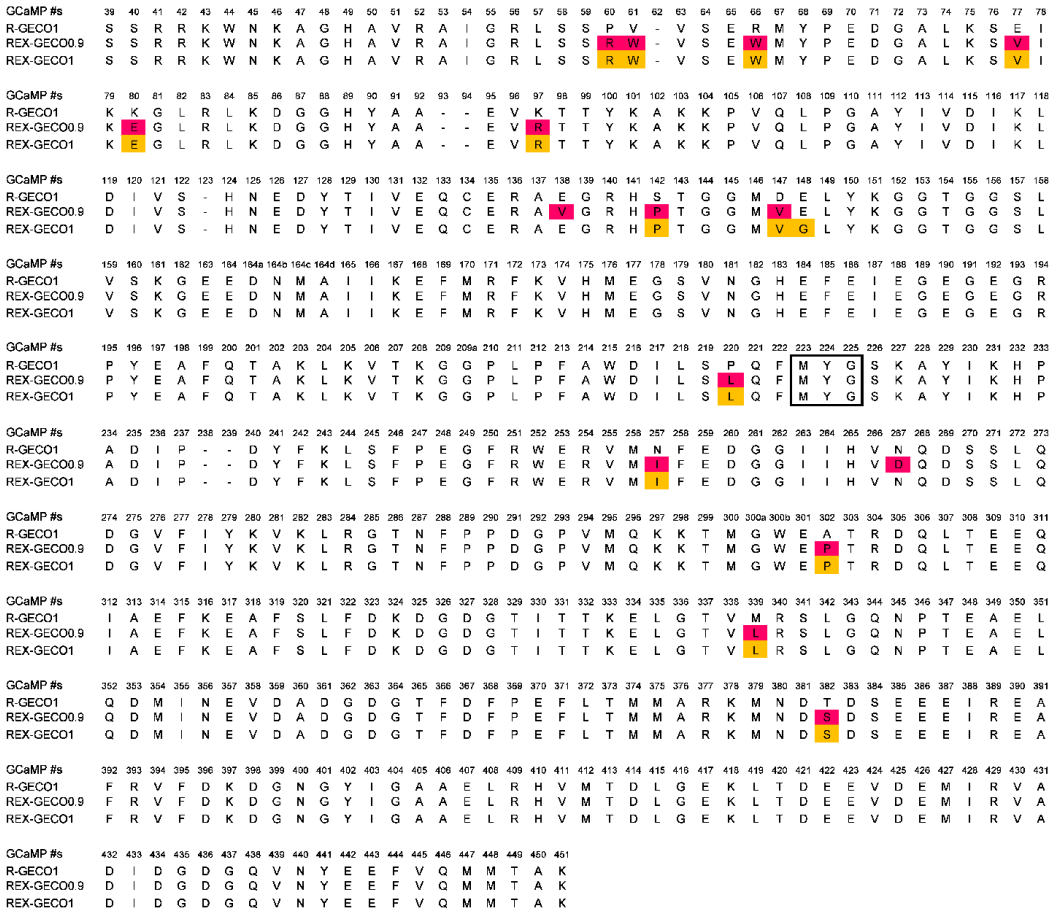

Figure 3.2. Sequence alignment of R-GECO1, REX-GECO0.9 and REX-GECO1. Changes relative to R-GECO1 are shown as colored boxes. The chromophore-forming tripeptide is enclosed in a black box. Residue numbering is consistent with the crystal structure of G-CaMP2 (PDB ID 3EVR) (*96*).

3.2.2 Rational design and directed evolution of REX-GECO0.1 for improved function

REX-GECO0.1's fluorescence brightness and maturation rate, in the context of *E. coli* colonies, were greatly reduced compared with R-GECO1. To engineer a variant with brighter fluorescence and a larger response to Ca^{2+}, we applied both rational design and directed evolution. Based on our previous

experience, the linker between M13 and the cpFP domain plays an important role in the protein folding efficiency and response to Ca^{2+} (*144*, *162*). In an effort to identify the optimal composition of this linker, we created a library by fully randomizing linker positions 60 and 61 (Pro and Val, respectively, in REX-GECO0.1). Screening of this library for bright long Stokes shift red fluorescence led to the identification of a variant with mutations Pro60Arg and Val61Trp (REX-GECO0.2). REX-GECO0.2 showed ~3-fold improved fluorescence brightness and improved maturation rate in *E. coli* relative to REX-GECO0.1, while retaining a similar excitation ratio change upon binding Ca^{2+}.

To further optimize REX-GECO0.2, we turned to a directed evolution strategy that involved multiple rounds of library creation by random mutagenesis and screening by fluorescence imaging of bacterial colonies. After each round the brightest clones were cultured, purified, and subjected to a secondary screen in microplate format to determine their Ca^{2+} response. A mixture of the 4-8 variants with the brightest fluorescence and largest responses to Ca^{2+} was used as the template for the next round of library creation by random mutagenesis. For the first 6 rounds of this procedure, we screened libraries only on the basis of the brightness of their long Stokes shift red fluorescence in colonies. For the last 2 rounds of directed evolution, we switched to screening for proteins that exhibited a combination of bright long Stokes shift and short Stokes shift (excitation at 542/27 nm and emission 609/57 nm) fluorescence (Figure 3.1B). The end product of these 8 rounds of directed evolution were two improved variants: REX-GECO0.9 and REX-GECO1 with 15 and 14 mutations, respectively, relative to R-GECO1 (Figure 3.3A, Figure 3.2, Table 3.1).

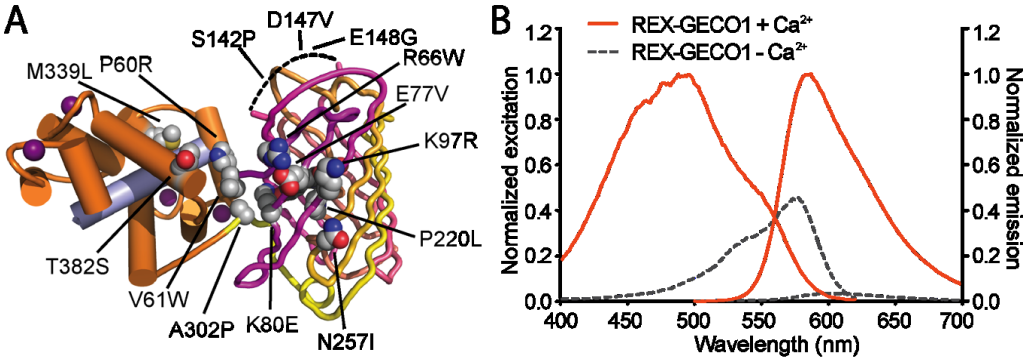

Figure 3.3. Structural model and excitation, emission spectra of REX-GECO1. (A) Model of REX-GECO1, showing location of substitutions relative to R-GECO1 (PDB ID 4I2Y) (*146*). Residue numbering is consistent with the crystal structure of G-CaMP2 (PDB ID 3EVR) (*96*). (B) Excitation and emission spectra of REX-GECO1 both in the presence and absence of Ca^{2+}.

Table 3.1. List of substitutions for new GECOs described in this work. Residues are numbered as described in **Figure 3.2**.

Protein	Substitutions relative to R-GECO1
REX-GECO0.9	P60R, V61W, R66W, E77V, K80E, K97R, E138V, S142P, D147V, P220L, N257I, N267D, A302P, M339L, T382S
REX-GECO1	P60R, V61W, R66W, E77V, K80E, K97R, S142P, D147V, E148G, P220L, N257I, A302P, M339L, T382S

3.2.3 *In vitro* characterization of REX-GECOs

Systematic *in vitro* characterization of REX-GECO0.9 and REX-GECO1 revealed that these two proteins exhibit very similar spectral properties and differ primarily in their respective affinities for Ca^{2+}. Specifically, REX-GECO1 (K_d = 240 nM, k_{off} = 1.7 s^{-1}) has a higher affinity for Ca^{2+} than REX-GECO0.9 (K_d = 680 nM,

k_{off} = 3.2 s^{-1}) (Figure 3.4EF, Table 3.2). Shared properties of the two proteins include excitation and emission maxima of 575 nm and 600 nm, respectively, in the Ca^{2+}-free state. Once bound to Ca^{2+}, these maxima shift to 480 nm and 585 nm, respectively (Figure 3.3, Table 3.2). Both REX-GECOs showed a strong 2-photon excitation peak at 910 nm (Figure 3.4GH). Absorbance spectra with and without Ca^{2+} are consistent with the fluorescence spectra (Figure 3.4AB), but also reveal the presence of an additional non-excitable absorption peak at 450 nm in the Ca^{2+}-free state. This peak likely corresponds to a population of the phenol form of the chromophore that is unable to undergo ESPT and instead undergoes excited state relaxation via a non-radiative pathway. REX-GECO0.9 and REX-GECO1 exhibit 70- and 100-fold maximal ratio changes, respectively, around physiological pH. These ratio changes decrease substantially at lower pH values, with apparent pK_as of 6.2 and 6.5, respectively (Figure 3.4CD, Table 3.2). When illuminated by a 405 nm laser (at 1200 mW/cm^2), both REX-GECOs showed minor photoactivation in the Ca^{2+}-free state, but not the Ca^{2+}-bound state (Figure 3.5).

Table 3.2. Properties of new GECOs described in this work.

Protein	Ca^{2+}	λ_{abs} (nm) (ε) ($mM^{-1}\cdot cm^{-1}$)	λ_{em} (Φ)	Brightness[1] ($mM^{-1}\cdot cm^{-1}$)	pK_a	Ratio change[2] ± Ca^{2+}	K_d for Ca^{2+} (nM) (Hill Coefficient)	k_{off} (s^{-1})
REX-GECO0.9	-	582 (26)	600 (0.07)	1.8	6.2	70×	680 (1.7)	3.2
	+	480 (27)	585 (0.23)	6.2				
REX-GECO1	-	582 (26)	600 (0.06)	1.6	6.5	100×	240 (1.8)	1.7
	+	480 (28)	585 (0.23)	6.4				

[1]Brightness is defined as the product of ε and Φ. [2]Defined as the change of the excitation ratio (450 nm / 580 nm), i.e. ratio change = R_{+Ca}/ R_{-Ca}-1, where R_{+Ca} is the excitation ratio in the Ca^{2+}-bound state, R_{-Ca} is the excitation ratio in the Ca^{2+}-free state. [3]pK_a is the pH at which the dynamic range is 50% of maximum.

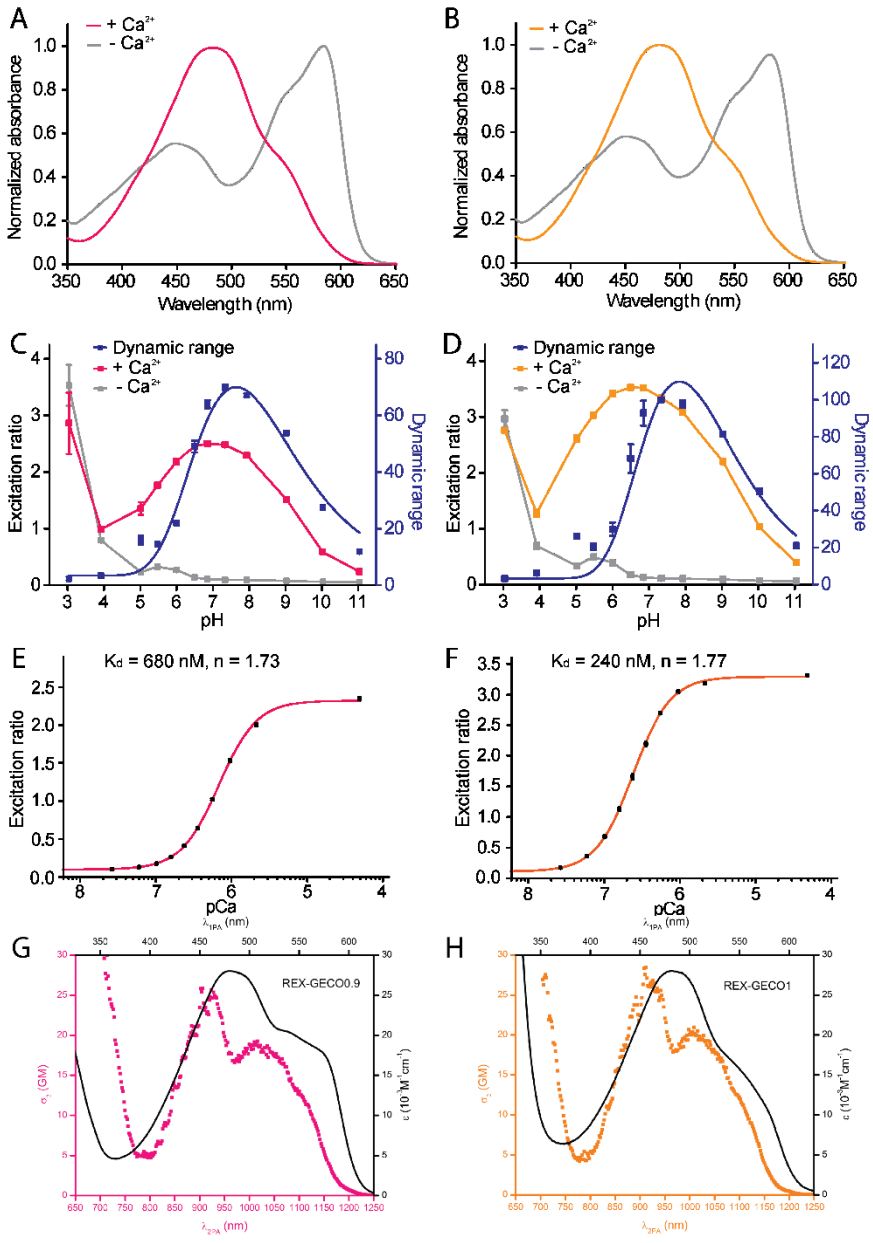

Figure 3.4. Characterization of REX-GECO0.9 and REX-GECO1. (A and B) Absorbance spectra of REX-GECO0.9 (A) and REX-GECO1 (B) in both the Ca^{2+}-free state (grey line) and the Ca^{2+}-bound state (pink or orange line). (C and D)

Excitation ratio and dynamic range of REX--GECO0.9 (C) and REX-GECO1 (D) as a function of pH. Excitation ratio = 480 nm / 570 nm excitation fluorescence intensity ratio. Dynamic range is calculated by dividing excitation ratio of the Ca^{2+}-bound state by the excitation ratio of the Ca^{2+}-free state. (E and F) Excitation ratio of REX-GECO0.9 (E) and REX-GECO1 (F) as a function of free Ca^{2+} concentration in buffer (10 mM MOPS, 100 mM KCl, pH 7.2). Excitation ratio = 480 nm / 570 nm excitation fluorescence intensity ratio. K_d is dissociation constant of Ca^{2+}, n is Hill coefficient. (G and H) 2-photon excitation spectra of REX-GECO0.9 (G) and REX-GECO1 (H).

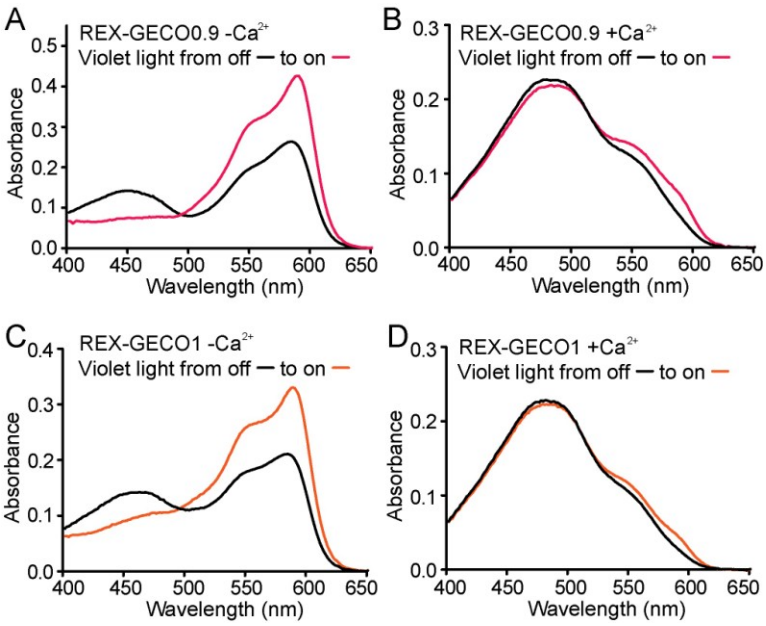

Figure 3.5. Characterization of REX-GECO0.9 and REX-GECO1 photoactivation. (A, B) Absorbance spectra of REX-GECO0.9 in the Ca^{2+}-free state (A) and in the Ca^{2+}-bound state (B) with or without a 405 nm laser (at 1200 mW/cm^2) illumination. (C, D) Absorbance spectra of REX-GECO1 in the Ca^{2+}-free state (C) and in the Ca^{2+}-bound state (D) with or without a 405 nm laser (at 1200 mW/cm^2) illumination.

Due to its higher Ca^{2+} affinity, which we empirically found to be associated with better performance in neurons, REX-GECO1 is our preferred variant for imaging applications. We attribute the differences in Ca^{2+} affinity to the Glu138Val mutation in REX-GECO0.9. Residue 138 is on the surface of the cpRFP and has its side chain directed toward the second EF-hand of CaM. Mutating the hydrophilic Glu to a hydrophobic Val likely alters the interactions at the cpRFP-CaM interface that communicate Ca^{2+} binding into a change in the chromophore environment.

3.2.4 Live cell performance of REX-GECO1 with 1-photon and 2-photon excitation

To explore the utility of REX-GECO1 for Ca^{2+} imaging, we expressed it in cultured human cells, dissociated rat hippocampal primary neurons, and organotypic rat hippocampal slices and performed a variety of intensiometric (1- and 2-photon excitation) and ratiometric (1-photon) imaging experiments. Initial experiments with HeLa cells expressing REX-GECO1 revealed 13.4 ± 4.7-fold intensity changes (fluorescence intensity for excitation at 472/30 nm and emission at 622/18 nm), and 36.2 ± 18.6-fold (n = 36) excitation ratio changes (ratio = fluorescence intensity for excitation at 472/30 nm with emission at 622/18 nm divided by fluorescence intensity from excitation at 620/60 nm with emission at 700/75 nm) upon treatment with histamine (Figure 3.6C, Table 3.3). When imaged using 2-photon microscopy (fluorescence intensity for excitation at 910 nm and emission at 642.5/75 nm), REX-GECO1 showed 5.3 ± 1.6-fold (n = 30)

intensity changes to histamine treatment (Figure 3.6D), consistent with our results from 1-photon excitation (Table 3.3).

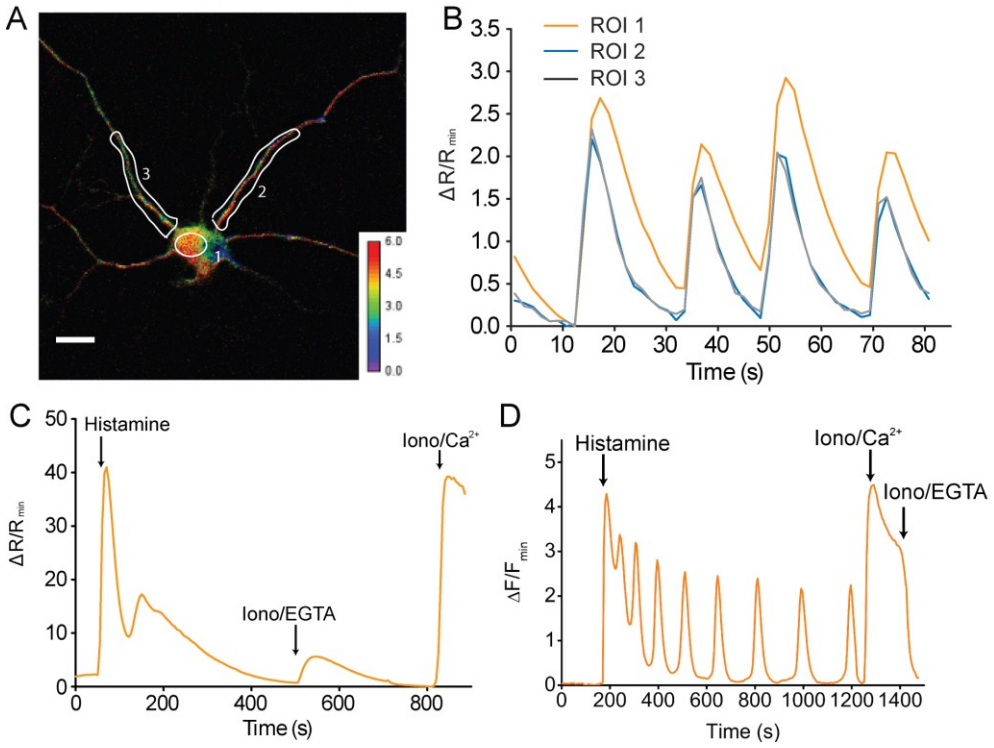

Figure 3.6. Imaging REX-GECO1 with 1-photon and 2-photon excitation. (A) Pseudocolored ratio image of a dissociated rat hippocampal neuron expressing REX-GECO1. Pseudocolored ratio is from red fluorescence ratio by blue light excitation to yellow light excitation. Scale bar represents 20 μm. (B) Change of excitation ratio vs. time traces for the same dissociated rat hippocampal neuron in (A). Three regions of interest (ROI) as labelled in (A); $\Delta R = R - R_{min}$. (C) Change of excitation ratio and fluorescence intensity traces of a HeLa cell expressing REX-GECO1 ($\Delta R = R - R_{min}$). (D) Change of red fluorescence intensity trace of a HeLa cell expressing REX-GECO1 ($\Delta F = F - F_{min}$) excited at 910 nm.

Table 3.3. Systematic characterization of the Ca^{2+}-dependent fluorescence of REX-GECO1 in HeLa cells with 1-photon (1P) and 2-photon (2P) excitation. Cells were treated with histamine (abb. His), then with Ca^{2+}/ionomycin (abb. Ca^{2+}), and finally with EGTA/ionomycin (abb. EGTA).

Protein	Excitation	n[1]	Maximum Ca^{2+} to minimum EGTA ratio	Maximum His to minimum His ratio	Maximum His to maximum Ca^{2+} ratio
REX-GECO1	1P ratiometric[2]	36	59 ± 26	36 ± 19	0.98 ± 0.37
	1P intensiometric[3]	36	23 ± 7	13 ± 5	0.84 ± 0.15
	2P intensiometric[4]	30	7.4 ± 2.6	5.3 ± 1.6	0.85 ± 0.32

[1]Number of individual transfected cells on which systematic calibration experiments were performed. [2]Ratio = fluorescence intensity for excitation at 472/30 nm and emission at 622/18 nm / fluorescence intensity from excitation at 620/60 nm and emission at 700/75 nm. [3]Intensity = fluorescence intensity for excitation at 472/30 nm and emission at 622/18 nm. [4]Intensity = fluorescence intensity for excitation at 910 nm (MaiTai DeepSee Ti:sapphire laser) and emission at 642.5/75 nm.

Next, we investigated the performance of REX-GECO1 in dissociated rat hippocampal neurons. REX-GECO1 has a K_d of 240 nM, making it suitable for detection of neuronal Ca^{2+} oscillations (typically from ~50 to 250 nM) (*177*). Dissociated rat hippocampal neurons expressing REX-GECO1 were imaged (1-photon excitation) using the same setup used for imaging HeLa cells. REX-GECO1 displayed high sensitivity to Ca^{2+} in dissociated rat hippocampal neurons, giving more than 2-fold ratio change for spontaneous Ca^{2+} changes (Figure 3.6AB).

My colleague, Ahmed Abdelfattah, further tested the performance of REX-GECO1 in hippocampal neurons and glial cells in rat organotypic hippocampal slices. Tissues were transiently transfected by *ex vivo* electroporation using two different plasmids with different promoters (Figure 3.7AC). Human synapsin I

promoter was used for preferential expression of REX-GECO1 in neurons (*178*, *179*) (Figure 3.8B). A cytomegalovirus (CMV) promoter was used to drive preferential expression of REX-GECO1 in glial cells (*180*) (Figure 3.8A). Hippocampal slices were cultured for 8-12 days (5-7 days post-transfection). Expression of REX-GECO1 in the cytoplasm of neural cells led to visualization of both the cell bodies and cell processes (Figures 3.7AC**,** Figure 3.9A). Transfected cells were healthy based on their morphology (Figure 3.8) and responsive as they showed expected pharmacologically-induced Ca^{2+} rises. During imaging we did notice a few intracellular puncta in the cell bodies of some neurons and glial cells, but this did not affect the health or response of those cells.

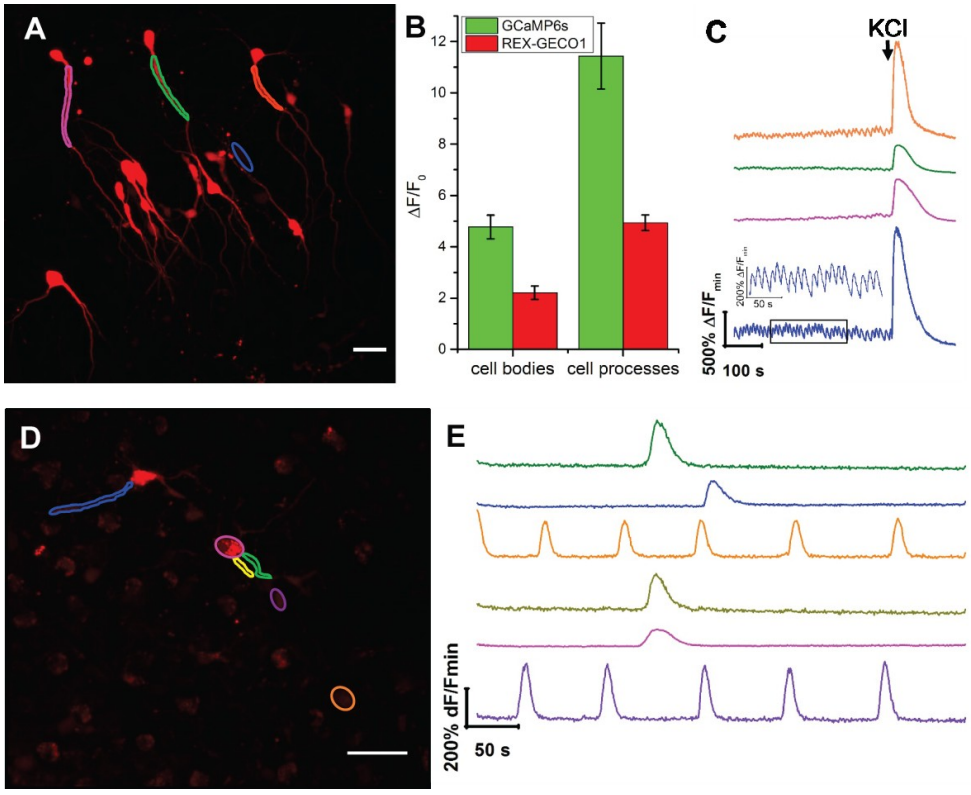

Figure 3.7. Confocal imaging of REX-GECO1 in neurons and glial cells in organotypic brain slices. (A) An average intensity projection of a 3D Z-stack of

images acquired for an organotypic rat hippocampal brain slice in which neurons are expressing REX-GECO1 under the synapsin I promoter. Scale bar represents 30 μm. (B) Comparison of REX-GECO1 and GCaMP6s in organotypic hippocampal brain slices. Response shown due to theophylline excitation of brain slices transfected with REX-GECO1 (cell bodies: 2.2 ± 0.5 fold; n = 8, cell processes: 4.9 ± 0.6 fold; n = 9) or GCaMP6s (cell bodies: 4.8 ± 0.9 fold; n = 5, cell processes: 11.4 ± 2.6 fold; n = 5). (C) Fluorescence vs. time traces for single cells as indicated in (A) upon treatment with 10 mM theophylline, followed by 30 mM KCl. The trace color corresponds to regions marked in (A). Inset: Zoom in on theophylline induced fluorescence oscillations as marked by black borderline. (D) An average intensity projection of a 3D Z-stack of glial cells expressing REX-GECO1 under CMV promoter in an organotypic rat hippocampal slice. Scale bar represents 30 μm. (E) Glutamate induced Ca^{2+} oscillations in glial cell bodies and processes as indicated in (D). Colors of the traces correspond to the colors of the regions marked in (D).

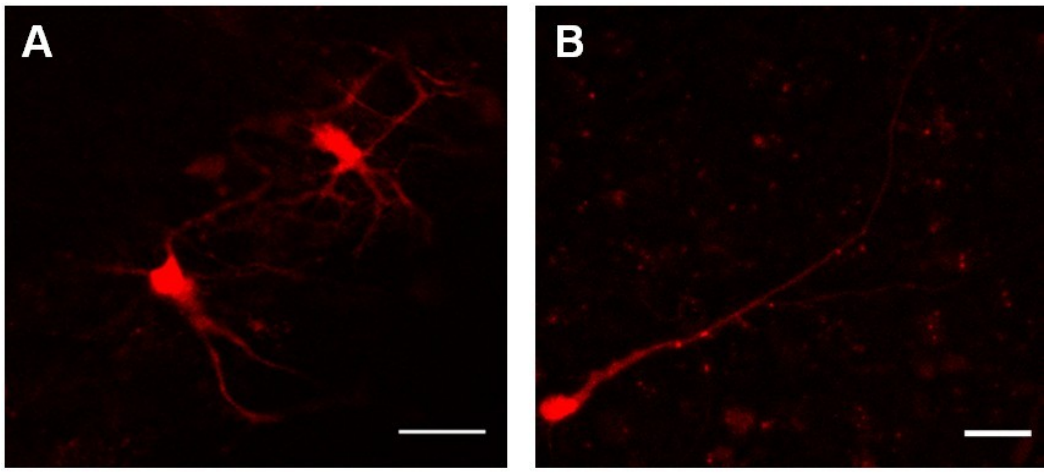

Figure 3.8. Confocal imaging of REX-GECO1 controlled by human synapsin I promoter and cytomegalovirus (CMV) promoter in rat hippocampal brain slices.

(A) REX-GECO1, under CMV promoter, preferentially expresses in glial cells when transfected in cultured rat hippocampal brain slices. Scale bar 30 μm. (B) REX-GECO1, under human synapsin I promoter, preferentially expresses in neurons when transfected in cultured rat hippocampal brain slices. Scale bar 30 μm.

When expressed in neurons, REX-GECO1 exhibited bright baseline fluorescence when excited by a 543 nm laser. For imaging of dynamic Ca^{2+} oscillations we switched to a 488 nm laser for excitation and used theophylline (10 mM) to pharmacologically excite neurons in organotypic brain slices. Theophylline, at low millimolar concentration, blocks both adenosine and $GABA_A$ receptors and has been shown to evoke sustained rhythmic seizure-like activities in different neural networks including hippocampal neurons (*181*–*185*). Indeed, upon treatment with theophylline, REX-GECO1 (under synapsin I promoter) successfully detected neuronal Ca^{2+} transients and oscillations with large fluorescence intensity changes (cell bodies: 2.2 ± 0.5 fold; n = 8, cell processes: 4.9 ± 0.6 fold; n = 9) (Figure 3.7B, Figure 3.9CD). Under identical conditions, GCaMP6s (*186*), one of the most highly optimized GFP-derived Ca^{2+} indicators, exhibits fluorescence changes in response to theophylline (cell bodies: 4.8 ± 0.9 fold; n = 5, cell processes: 11.4 ± 2.6 fold; n = 5) that are approximately double that of REX-GECO1 (Figure 3.7C). Depolarization of REX-GECO1-expressing neurons with 30 mM KCl, which activates voltage-gated Ca^{2+} channels to promote Ca^{2+} influx (*187*, *188*), increased fluorescence intensity by 11.7 ± 3.4-fold (n = 8).

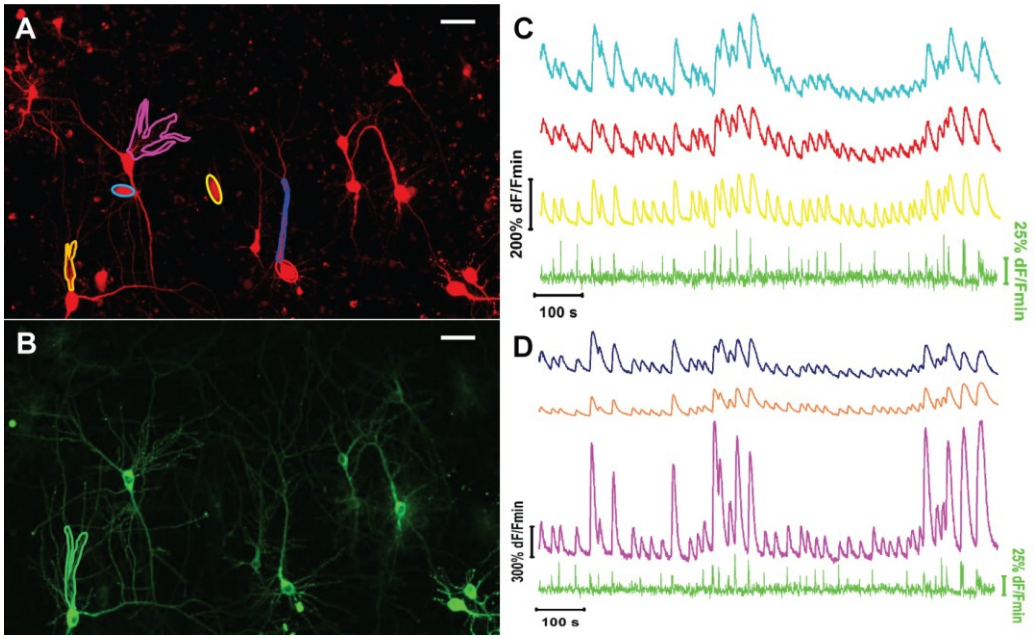

Figure 3.9. 1-photon confocal dual-color imaging of REX-GECO1 co-expressed with a green glutamate indicator (iGluSnFR) in organotypic rat hippocampal slices. (A) An average intensity projection of a 3D Z-stack of neurons expressing REX-GECO1 under synapsin I promoter in a hippocampal slice, Scale bar represents 30 μm. (B) An average intensity projection of a 3D Z-stack of the neurons in (A) expressing iGluSnFR under synapsin I promoter in a hippocampal slice, Scale bar represents 30 μm. (C-D) Simultaneous imaging of theophylline-induced [Ca^{2+}] oscillations and glutamate transients in (C) neuron cell bodies and (D) neuron processes as highlighted in (A) and (B). Colors of the traces correspond to the colors of the highlighted regions. The glutamate signal is shown in green in both graphs.

Bath-application of glutamate was used to evoke Ca^{2+} rises in hippocampal glial cells expressing REX-GECO1 (under the CMV promoter). Activation of the glutamate receptors on glial cells leads to an increase in intracellular Ca^{2+} levels

mostly due to 'metabotropic' release from endoplasmic reticulum (*189*–*191*). This Ca^{2+} increase has been described as oscillatory waves of elevated intracellular Ca^{2+} concentration spreading across glial cells (*192*, *193*), including those of the rat hippocampus (*194*). REX-GECO1 successfully detected Ca^{2+} rises in both glial cell bodies (2.2 fold ± 1.0 fold; n = 4) and their processes (3.7 ± 0.9 fold; n = 10) with sufficient spatial and temporal resolution to allow us to visualize Ca^{2+} waves across the cells as described previously (Figure 3.7CD).

Overall, REX-GECO1 showed robust responses to the activities of neural cells. Notably, we found that the bright baseline fluorescence with 543 nm laser excitation helped us to identify cells of interest. Moreover, the dim baseline fluorescence with the 488 nm laser excitation enables recording of Ca^{2+} oscillations with a large dynamic range. We believe that the combination of these two characteristics will greatly facilitate efforts to use REX-GECO1 for both identifying and imaging Ca^{2+} dynamics in cells of interest.

3.2.5 REX-GECO1 for dual color imaging in rat hippocampal organotypic slice cultures

We next investigated the utility of REX-GECO1 in multicolor imaging together with a second genetically encoded indicator. Since REX-GECO1 has a Ca^{2+}-dependent excitation peak at 480 nm, we reasoned that it could also be used as an intensiometric red Ca^{2+} indicator with a large Stokes shift, and thereby combined with an intensiometric green indicator for multicolor imaging using a single excitation wavelength. To demonstrate this, we set out to image both Ca^{2+} and glutamate responses in organotypic rat hippocampal slice cultures. We reasoned that because pyramidal hippocampal neurons are glutamatergic

(*195*), one would be able to simultaneously detect Ca^{2+} transients and glutamate release when neurons are excited. My colleague, Ahmed Abdelfattah, co-expressed REX-GECO1 in the cytosol and a green glutamate indicator, iGluSnFR (*9*), on the plasma membrane of neurons using a synapsin I promoter for both indicators (Figure 3.9AB) and used theophylline to induce seizure-like activity in hippocampal neurons as described above. Using 1-photon excitation at 488 nm, we successfully recorded simultaneous glutamate release (green channel) and Ca^{2+} transients (red channel). REX-GECO1 revealed Ca^{2+} rises in both the cell bodies (Figure 3.9C) and processes (Figure 3.9D) of hippocampal neurons with large signal magnitude (cell bodies: 2.2 ± 0.5 fold; n = 7, cell processes: 4.9 ± 0.6 fold; n = 7). A short lasting (~0.5 s) increase in glutamate, as released from surrounding neurons (*196*), was followed by a longer (~10-20 s) Ca^{2+} rise in neurons indicating that the Ca^{2+} influx was induced by glutamate. Similar results were obtained using 2-photon excitation at 940 nm for both REX-GECO1 and iGluSnFR (Figure 3.10). Overall, these results demonstrate that REX-GECO1 can be combined with GFP-based indicators to create new opportunities for simultaneous multicolor 1- and 2-photon imaging.

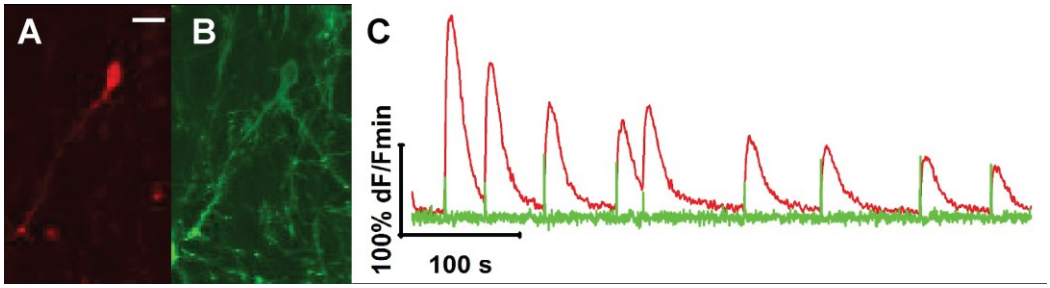

Figure 3.10. 2-photon dual-color imaging of neurons co-expressing REX-GECO1 and iGluSnFR in organotypic rat hippocampal brain slices. (A) A neuron expressing cytoplasmic REX-GECO1 under synapsin I promoter in a

hippocampal slice (emission 605-680 nm), Scale bar represents 20 μm. (B) The same neuron as in (A) co-expressing iGluSnFR on the plasma membrane (emission 460-500 nm). (C) Theophylline-induced Ca^{2+} (red) and glutamate (green) transients and oscillations in the neuron in (A) and (B) excited at 940nm.

3.2.6 REX-GECO1 for *in vivo* imaging

One of the most powerful applications of genetically encoded Ca^{2+} indicators is minimally invasive monitoring of neuronal activity *in vivo*. Dr. Loïs S. Miraucourt and Elena Kutsarova from Dr. Edward S. Ruthazer's group in McGill University used DNA electroporation to drive expression of REX-GECO under the CMV promoter, in some cases co-expressed with EGFP, in the eye and optic tectum of albino *Xenopus laevis* tadpoles (Figure 3.11A). Animals were imaged by 2-photon microscopy at least two days after electroporation to allow sufficient protein expression. We first used an *ex vivo* isolated brain preparation to monitor Ca^{2+} elevation in optic tectal neurons co-expressing REX-GECO0.9 and EGFP in response to pharmacological activation of N-methyl-D-aspartate (NMDA) type ionotropic glutamate receptors (Figure 3.11B). Bath application of 20 μM NMDA resulted in a robust increase in the ratio of red to green fluorescence in these cells (2.2±0.37 fold; n = 6 cells). We next tested whether REX-GECO1 could be used to detect neuronal responses to more physiological stimuli, by presenting brief pulses of light to activate neurons in the visual system of the intact animal. Neurons in the optic tectum, the primary visual area in the tadpole brain, are readily distinguishable from radial glial cells based on their position and morphology. Figure 3.11C shows an example of REX-GECO1 fluorescence changes in the cell body of a tectal neuron in response to 10 s light flashes

presented to the contralateral eye (max $\Delta F/F_0$ of mean response = 70.6%). As expected, the neighboring radial glia cell showed no light-evoked response above noise for this experiment. In the retina, light modulates glutamate release from photoreceptors onto bipolar cells, driving a change in their membrane potential. Unlike tectal neurons, bipolar cells do not fire action potentials, but instead rely on voltage-dependent Ca^{2+} influx at their axon terminals to continuously modulate neurotransmitter release. Consequently, 1 s light flashes evoked small but consistent increases in REX-GECO1 fluorescence in the axon terminals (max $\Delta F/F_0$ of mean response = 10.3%) but not at the bipolar cell soma (max $\Delta F/F_0$ of mean signal = 0.7%) (Figure 3.11D). EGFP fluorescence did not respond to visual stimulation, making it useful for correcting for gradual specimen drift which can be a common problem when imaging in the intact animal. These results demonstrate that REX-GECO1 can be used to detect physiological Ca^{2+} changes in neurons *in vivo*.

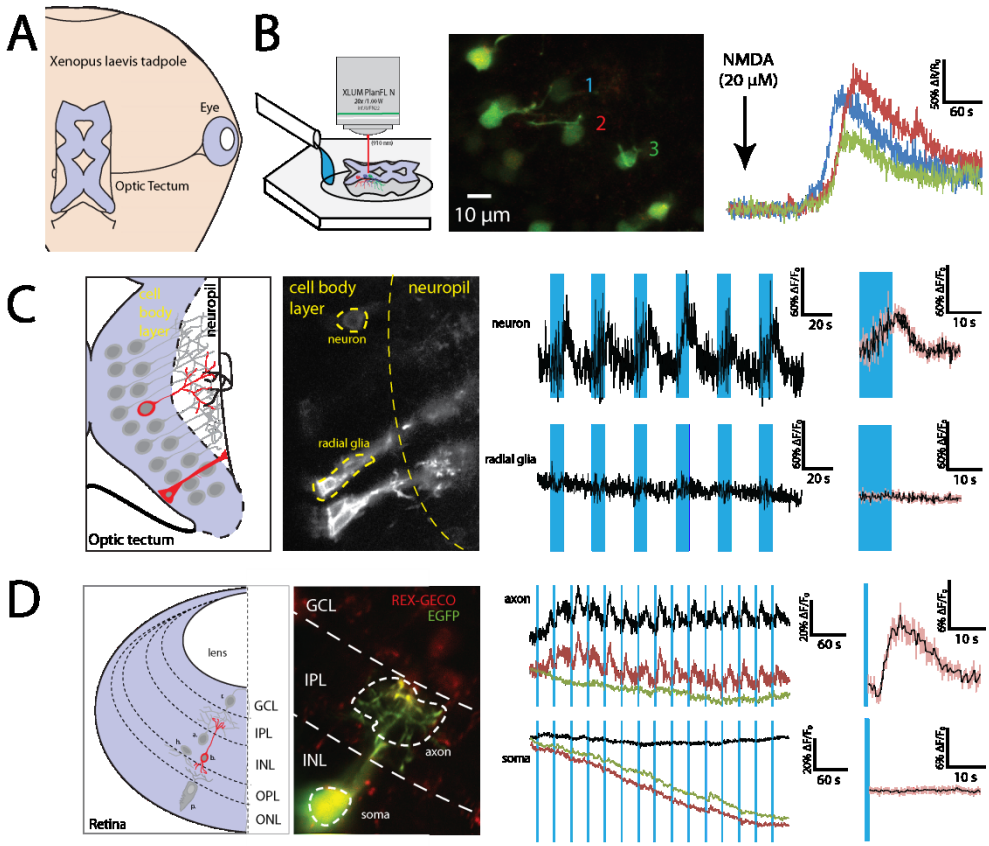

Figure 3.11. *Ex vivo* and *in vivo* 2-photon microscopy of REX-GECO responses to pharmacological and visual stimulation in the retinotectal system of Xenopus laevis tadpoles. (A) The eye projects visual inputs to the contralateral optic tectum in the tadpole (OB, olfactory bulb; DiE, diencephalon; E, eye; OT, optic tectum; HB, hindbrain). (B) Whole brain prep with tectal neurons co-expressing REX-GECO0.9 (red) and EGFP (green) imaged at 910 nm responding to bath application of 20 µM NMDA for the 3 cells indicated. *middle*: 2P z-stack projection. (C) *In vivo* tectal neuron co-expressing REX-GECO1 and EGFP exhibits Ca^{2+} transients in response to 10 s light flashes to the eye (blue bars). Radial glia is unresponsive. Regions of interest drawn for the cells analyzed. *Right*: Average of visually evoked responses (black) ± SEM (red). (D) Non-spiking retinal bipolar cell co-electroporated with REX-GECO1 (red) and EGFP (green) shows light

evoked Ca^{2+} elevations in the neuropil but not in the cell soma. (ONL – outer nuclear layer; OPL – outer plexiform layer; INL – inner nuclear layer; IPL – inner plexiform layer; GCL – ganglion cell layer; p. – photoreceptor; h. – horizontal cell; b. – bipolar cell; a. – amacrine cell; r. – retinal ganglion cell). Plots of somatic and axonal $\Delta F/F_0$ for REX-GECO1 (red) and EGFP (green) in response to 2 s light flashes (blue bars). The black trace is REX-GECO1 with EGFP $\Delta F/F_0$ subtracted. *Right*: Averaged responses of the bipolar cell subdomains to light flashes.

3.3 Conclusion

By utilizing rational design and directed evolution, we have developed a red fluorescent Ca^{2+} indicator, REX-GECO1, with an *in vitro* ratiometric change up to 100-fold. The availability of REX-GECO1 provides new possibilities for Ca^{2+} imaging using genetically encoded indicators with high sensitivity, as we have demonstrated in HeLa cells, dissociated rat hippocampal neurons, neurons and glial cells in organotypic rat hippocampal slices, and tectal neurons in the tadpole brain *in situ*. With a Ca^{2+}-dependent excitation peak at 480 nm, and a 2-photon excitation peak at ~910-940 nm, REX-GECO1 enables simultaneous dual color imaging together with a GFP-based fluorescent probe. We demonstrate the utility of this feature of REX-GECO1 by simultaneously imaging both Ca^{2+} and glutamate in both 1- and 2-photon modalities. Overall, we expect that REX-GECO1 will have broad appeal as the preferred Ca^{2+} indicator for use in combination with any of the plethora of GFP-based probes and indicators currently available.

3.4 Materials and methods

3.4.1 Engineering and screening of REX-GECO

For the engineering of REX-GECO, R-GECO1 in pTorPE (*144*) was used as a template. Point mutations to R-GECO1 were performed using QuikChange II Site-Directed Mutagenesis Kit (Agilent Technologies). Random mutagenesis was generated by error-prone PCR amplification. In the first generation library, the codon for residue 64 was mutated to BMM (encoding Ala, Asp, Gln, Glu, His, Pro, Ser, and Tyr), the codon for residue 80 was mutated to VAN (encoding Asn, Asp, Gln, Glu, His, and Lys), and the codon for residue 116 was mutated to VHM (encoding Ala, Asn, Asp, Gln, Glu, His, Ile, Leu, Lys, Met, Pro, Thr, and Val).

For REX-GECO variants screening, the imaging system used has been described in detail (*155*). PTorPE plasmids containing REX-GECO variants were electroporated into *E. coli* strain DH10B (Invitrogen). These *E. coli* were then cultured on 10 cm LB-agar Petri dishes supplemented with 400 μg/mL ampicillin (Sigma) and 0.0004% (wt/vol) L-arabinose (Alfa Aesar) at 37 °C overnight. During screening, a 609/57 nm emission filter was used to capture the fluorescence emission. Two images, image A and image B, were captured by using excitation filter of 438/24 nm or 542/27 nm to illuminate *E. coli* colonies expressing REX-GECO variants on Petri dishes. These two images were then multiplied to generate a third image C. Colonies showed the highest 0.1% emission intensities in image C were picked and cultured in 4 mL liquid LB with 100 μg/mL ampicillin and 0.0016% (wt/vol) L-arabinose at 37 °C overnight. Proteins were then extracted from the liquid LB culture and subjected to a secondary screen by using a Safire2 fluorescence microplate reader (Tecan).

3.4.2 Characterization of REX-GECO1

To purify REX-GECO1 proteins for characterization, DH10B *E. coli* expressing REX-GECO1 in pTorPE were picked and cultured in 4 mL liquid LB medium (100 μg/mL ampicillin) at 37 °C overnight. This 4 mL culture was then inoculated into 500 mL liquid LB medium (100 μg/mL ampicillin, 0.0016% L-arabinose) and cultured at 22 °C for 48 h. After culture, bacteria were harvested by centrifugation and resuspended in 30 mM Tris-HCl buffer (pH 7.3). REX-GECO proteins were extracted from bacteria by French press and centrifugation, followed by Ni-NTA affinity chromatography (Agarose Bead Technologies) for purification. Purified REX-GECO proteins were subjected to buffer exchange to 10 mM MOPS, 100 mM KCl (pH 7.2) by centrifugal concentrators (GE Healthcare Life Sciences).

To measure the fluorescence and absorbance spectra of REX-GECO, a QuantaMaster spectrofluorometer (Photon Technology International), and a DU-800 UV-visible spectrophotometer (Beckman) were used, respectively. To determine REX-GECO's quantum yield (Φ), mCherry and LSS-mKate2 were used as standards. Specifically, protein solutions were diluted by 10 mM MOPS, 100 mM KCl (pH 7.2) buffer to make solutions with absorbance values at excitation wavelength ranging from 0.01 to 0.05. Fluorescence spectra of each sample were measured, and the total fluorescence intensities were obtained by integration. These integrated fluorescence intensities were plotted against their absorbances, and the slope (S) of each line was determined. Quantum yield of REX-GECO was then determined by using the following equation: $\Phi_{protein} = \Phi_{standard} \times (S_{protein}/S_{standard})$. To determine extinction coefficient (ε), REX-GECO was first subjected to alkaline denaturation, its concentration was determined by the following equation: $c = A/(\varepsilon \times b)$, where A is absorbance at 450 nm, ε =

44,000 $M^{-1}cm^{-1}$, b = 1 cm. Then, its extinction coefficient was calculated by ε = A/(b × c), where A is peak absorbance before denaturation, b = 1 cm, c is the protein concentration. To measure the apparent pK_a of REX-GECO, a series of buffers (containing 30 mM trisodium citrate and 30 mM borax) with pH ranging from 3 to 11 were prepared. Fluorescence intensities of REX-GECO were measured in this set of pH buffers with and without the present of Ca^{2+}, respectively. The fluorescence intensities at different pH values were then fitted by Hill equation to determine the apparent pK_a. To determine REX-GECO's K_d to Ca^{2+}, a series of buffers were prepared by mixing Ca^{2+}-saturated and Ca^{2+}-free buffers according to previously described (*144*). REX-GECO proteins were then added into this series of buffers, and their fluorescence intensities were measured. These fluorescence intensities were then plotted against Ca^{2+} concentrations and fitted by Hill equation. A SX20 stopped-flow spectrometer (Applied Photophysics) was used to measure k_{off}. Briefly, Protein samples with 10 μM $CaCl_2$ (in 10 mM MOPS, 100 mM KCl pH 7.2) were rapidly mixed with a solution with 10 mM EGTA (in 10 mM MOPS, 100 mM KCl pH 7.2) at room temperature. The k_{off} was determined by fitting the fluorescence decay curve to a single exponential equation. Each protein sample was measured five times, and the averaged value was taken as k_{off}.

Two-photon absorption spectra were measured using fluorescence femtosecond setup, described previously (*171*). Briefly, it comprises a tunable parametric amplifier (550-2000 nm) producing ~100 fs pulses with 1 kHz repetition rate. Rhodamine B in methanol was used as a reference standard (*156*) for both the spectral shape and absolute cross section evaluations. The cross sections were measured at 900, 1000, and 1130 nm. The quadratic power dependence of fluorescence signal was checked at several wavelengths across

the spectrum. The concentration of proteins with matured chromophore was evaluated spectrophotometrically by using the extinction coefficients measured by alkaline denaturation method (see above). Note that Figure 3.4 presents the effective two-photon cross section weighted with the relative fractions of neutral, $n^{(n)}$, and anionic, $n^{(a)}$, forms: $\sigma_2(\lambda) = \nu^{(\nu)}\,\sigma_2{}^{(\nu)}(\lambda) + \nu^{(\alpha)}\,\sigma_2{}^{(\alpha)}(\lambda)$, where $\sigma_2{}^{(\nu)}(\lambda)$ and $\sigma_2{}^{(\alpha)}(\lambda)$ are the molecular two-photon absorption cross sections of the neutral and anionic forms, respectively, and $n^{(n)} + n^{(a)} = 1$.

3.4.3 Plasmids for mammalian cell imaging

For REX-GECO1 plasmid with a cytomegalovirus (CMV) promoter, template (REX-GECO1 in pTorPE (*144*)) was cloned into a modified pcDNA3 plasmid by PCR as previously described (*162*). This vector was used in 1-P, 2-P imaging of HeLa cells and 1-P imaging of dissociated rat hippocampal neurons. For REX-GECO1 plasmid with a human synapsin I promoter, template (REX-GECO1 in pTorPE) was cloned into an AAV2 plasmid flanked by restriction sites BamH1 and HindIII by PCR using primers: BamH1_fw (5' GAGGATCCACCATGGTCGACTCATCACGTC 3') and HindIII_rv (5' GCGATGAAGCTTCTACTTCGCTGTCATCATTTGTACAAACTCTTCGTAGTTT 3'). For iGluSnFR plasmid with a human synapsin I promoter, iGluSnFR (Addgene plasmid 41732) was used as a template, and cloned into an AAV2 plasmid flanked by restriction sites BamH1 and HindIII by PCR using primers: BamH1_iGlu_fw (5' CGAGGATCCGCCACCATGGAGACAGACACACTCCTG CTATGGGTAC 3') and HindIII_iGlu_rv (5'CCCTTATCATCCTCATCATGCTTT GGCAGAAGAAGCCACGTTAGAAGCTTCGATCC 3'). For GCaMP6s plasmid (with a human synapsin I promoter) used in comparison with REX-GECO1 in rat

hippocampal organotypic brain slices, GCaMP6s (Addgene plasmid 40753) was used as a template, and cloned into the same AAV2 plasmid flanked by restriction sites BamH1 and HindIII as for iGluSnFR.

3.4.4 Cell culture

HeLa cells (CCL2 line; ATCC) were cultured on collagen-coated 35 mm glass bottom dishes (Mastumami) until they reached 40-60% confluency. Transfection was performed by incubating HeLa cells with the mixture of 1 µg of plasmid DNA and 3 µL of Lipofectamine 2000 (Life technologies) for 2 h. After incubation, the medium was exchanged to Dulbecco's modified Eagle's medium (DMEM) (supplemented with 10% fetal bovine serum (FBS) (Sigma), 2 mM GlutaMax (Invitrogen) and penicillin-streptomycin) and the cells were incubated for 48 h at 37 °C in a CO_2 incubator. Prior to imaging, culture medium was changed to HEPES (25 mM) buffered Hanks' Balanced Salt Solution (HBSS).

Dissociated E18 Sprague Dawley Hippocampal Cells in Hibernate® EB Complete Media were purchased from BrainBits LLC. The cells were grown on (In Vitro Scientific) 35 mm glass bottom dish containing NbActiv4 (BrainBits LLC) supplemented with 2% FBS, penicillin-G potassium salt (50 units/mL), and streptomycin sulfate (50 µg/mL). Half of the culture media is replaced every 4-5 days. Neuronal cells were transfected on day 7 with plasmids containing constructs of interest using Lipofectamine 2000.

3.4.5 Transfection of rat hippocampal organotypic brain slices

Horizontal brain slices (250 µm thickness) from a 0-day-old (P0) Sprague Dawley rat were generated in ice-cold HBSS containing 1.3 mM $CaCl_2$ and 1 mM

$MgSO_4$ with a vibrating microtome (Leica VT1000S, Leica Microsystems, Richmond Hill, ON, Canada) as described previously (*182*). All procedures were carried out in compliance with the guidelines of the Canadian Council for Animal Care and with the approval of the University of Alberta Animal Care and Use Committee for Health Science. Hippocampal regions were cut from horizontal brain slices and placed on a sterile 0.4 µm pore membrane cell culture insert (Millipore PICMORG50). The insert and slice were then placed in a Petri dish containing 1.5 ml of NbActiv4 (BrainBits) supplemented with 5% fetal bovine serum (FBS), penicillin-G potassium salt (50 units/mL), and streptomycin sulfate (50 µg/mL). Slices are cultured at 37°C and 5% CO_2 for 24 hours prior to transfection by electroporation. The insert and slice are then placed directly above a Platinum Plate Petri dish electrode (CUY700-P2E, Nepa Gene, Japan), and the gap between the electrode and the membrane is filled with electroporation buffer (EB) (HBSS with 1.5 mM $MgCl_2$ and 10 mM glucose). Plasmids (pcDNA3.1, Life Technologies and AAV2 plasmid) for expression of the gene of interest are dissolved in EB at a concentration of 1 µg/µL and sufficient volume is added to just cover the slice. A square platinum electrode (CUY700-P2L, Nepa Gene, Japan) is then placed directly above the hippocampus slice and a power supply is used to apply five 20 V pulses (5 ms each, 1 Hz). The direction of electrical field is reversed and a second set of five pulses with the same settings is applied. The EB buffer is carefully replaced with supplemented NbActiv4 and slices are returned to incubator at 37 °C with 5% CO_2.

3.4.6 Microscopes for fluorescence imaging

Widefield imaging was performed on an inverted Nikon Eclipse Ti microscope equipped with a 200 W metal halide lamp (PRIOR Lumen), 20× and 40× objectives (Nikon), and a 16-bit QuantEM 512SC electron-multiplying CCD camera (Photometrics). A filter set of 472/30 nm (excitation), 622/18 nm (emission), and 495 nm (dichroic) was used for long Stokes shift excitation. Another filter set of 620/600 nm (excitation), 700/75 nm (emission), and 666 nm (dichroic) was used for short Stokes shift excitation. For time-lapse imaging, HeLa cells were treated with 5 μM (final concentration) histamine, 4 mM EGTA (with 5 μM ionomycin) and 10 mM $CaCl_2$ (with 5 μM ionomycin) in chronological order.

For 1-photon imaging, we used an upright FV1000 confocal microscope (Olympus Canada, Markham, ON, Canada) equipped with software (FluoView1000, Olympus Canada), a 20× XLUMPlanF1 water immersion objective (numerical aperture = 1.00), or a 60× XLUMPlanF1 water immersion objective (numerical aperture = 0.90), and connected to multi-line argon lasers (457 nm, 488 nm, and 515 nm) and HeNe lasers (543 nm and 633 nm) (Olympus Canada). For 2-photon imaging, we used a similar confocal system connected to a MaiTai DeepSee Ti:sapphire laser with a tunable excitation range from 710-990 nm (Spectra Physics, Santa Clara, CA, USA).

3.4.7 Imaging of rat organotypic hippocampal slices

The brain slice on the Millipore insert was placed in a custom-made chamber to hold it in place during imaging. Immediately prior to imaging, the slices were perfused with artificial cerebrospinal fluid (ACSF) superfusate

containing: 120 mM NaCl, 3 mM KCl, 1 mM $CaCl_2$, 2 mM $MgSO_4$, 26 mM $NaHCO_3$, 1.25 mM NaH_2PO_4 and 10 mM D-glucose (pH adjusted to 7.4 by gassing with 95% O_2, 5% CO_2), at 5 mL/min using a peristaltic pump (Watson-Marlow Alitea-AB, Sin-Can, Calgary, Alberta, Canada) and kept at room temperature. Imaging was started within 10 min following activation of the perfusion system.

For single-color 1-photon imaging of Ca^{2+} using REX-GECO1, the hippocampal slice was excited with 488 nm laser and emission was collected from 550 nm to 650 nm using a variable barrier filter. For dual-color imaging of Ca^{2+} using REX-GECO1 and glutamate using iGluSnFR, the slice was excited with 488 nm laser and emission was collected simultaneously in two channels from 500-520 nm for iGluSnFR and 590-690 nm for REX-GECO1 using variable barrier filters. In all cases, images were acquired at 1-3× digital zoom at a reduced frame resolution (256 × 256) and with a 4 µs/pixel scanning rate. This allowed image acquisition to be 2-3 frame/s to detect Ca^{2+} and glutamate oscillations in neurons and glial cells.

For 1-photon imaging of theophylline-induced Ca^{2+} and/or glutamate rises in neurons, images were acquired every 0.5 s. Approximately 30 s after the start of the experiment, the superfusate was changed from control ACSF to ACSF containing 10 mM theophylline (Sigma-Aldrich, directly dissolved in ACSF). Approximately 10 min later, the superfusate was changed back to control ACSF. For KCl-evoked depolarization, 10 µL of (2.5 M) KCl was added to raise the concentration of KCl in the recording buffer to 30 mM instantaneously and then left to wash out at the regular rate of the perfusion system at 5 mL/min.

For 1-photon imaging of glutamate-induced Ca^{2+} dynamics in glial cells, images were acquired every 0.5 s. Approximately 30 s after the start of the

experiment, the superfusate was changed from control ACSF to ACSF containing 100 µM glutamate (Sigma-Aldrich, 1 M stock in dH_2O, diluted to final concentration in control ACSF) for 10 min and then switched back to control ACSF.

For two color 2-photon imaging of REX-GECO1 and iGluSnFR, the laser wavelength was set at 940 nm. Fluorescence emission was collected using two photomultiplier tube (PMT) detectors, one of which was equipped with a 460-500 nm bandpass filter, and the other equipped with a 605-680 nm bandpass filter (Semrock Inc, Rochester, New York, USA). Images were acquired every 0.25 s.

3.4.8 REX-GECOs *in vivo*

Albino Xenopus laevis tadpoles were bred by human chorionic gonadotropin-induced mating. Embryos were reared at room temperature in 0.1x modified Barth's saline with HEPES (MBSH). Tadpoles were developmentally staged according to the standard criteria of Nieuwkoop and Faber (*197*). Experiments were approved by the Montreal Neurological Institute Animal Care Committee in accordance with Canadian Council on Animal Care guidelines.

For *in vivo* electroporation, cells in the retina and optic tectum were bulk electroporated as described previously (*198*). In brief, glass micropipettes made from borosilicate capillaries pulled on a PC-10 puller (Narishige, Japan) were loaded with DNA plasmid solution (0.5 to 5 µg/µL) and attached to a custom-made pressure injection system. Plasmid solution was then pressure-injected in the eye or brain ventricle and current was locally delivered across custom-made platinum plate electrodes placed on either side of the eye, or the tectum using 3

pulses (36 Volts, 1.6 ms) in each polarity using a constant voltage stimulator (Grass SD-9) with a 3μF capacitor placed in parallel.

For *in vivo* imaging of Xenopus tadpoles, stage 40 tadpoles for retinal electroporation and stage 43 for tectal electroporation were transfected with plasmids encoding REX-GECO1 alone or mixed with EGFP-encoding plasmid, and given at least 48h to express the protein. Stage 45-47 tadpoles were immobilized by a bath application of pancurinium bromide (2 mM, Sigma) and placed in a custom-made imaging chamber, embedded in 1% agarose, and then immersed in MBSH solution for tectal cell imaging and with ACSF external solution for retinal imaging. The ACSF solution contains 115 mM NaCl, 2 mM KCl, 5 mM HEPES, 3 mM $CaCl_2$, 1.5 mM Mg^{2+}, 10 mM Glucose, 5 μM Glycine; 250 mOsm; pH 7.2. *In vivo* two-photon images of tectal cells or retinal cells were acquired at 2 Hz and 5 Hz respectively, using a Thorlabs multiphoton microscope with resonant scanner and Olympus 20x 1.0NA immersion objective, A MaiTai-BB Ti:sapphire femtosecond pulsed laser set to excite at 910 nm was used for fluorescence excitation. Green (500-550 nm) and red (584-676 nm) emission filters were used for fluorescence detection. For visual stimulation, an A310 Accupulser (WPI) was used to drive a blue LED (447.5 nm, royal-blue Luxeon® Star) to present trains of light flashes.

For *ex vivo* imaging of tadpole brains, stage 45-47 tadpoles were anesthetised by immersion in 0.02% MS-222 and the brain was dissected and perfused with Mg-free external solution containing 115 mM NaCl, 2 mM KCl, 5 mM HEPES, 3 mM $CaCl_2$, 10 mM Glucose, 10 μM Glycine; 250 mOsm; pH 7.2. Imaging was carried out at 910 nm using an Olympus FV300 confocal microscope converted for multiphoton use, with a 40x 1.0 NA immersion

objective. For pharmacological activation of NMDARs, 20 μM NMDA was applied to the bath. To visualize fluorescence intensity changes, images of the tectum were acquired at 2 Hz simultaneously on green (500-550 nm) and red (593-668 nm) channels. At the end of each experiment z-series stacks at 1 μm inteval were collected to obtain full 3D cellular morphologies.

For fluorescence intensity change analysis, ellipsoid regions of interests (ROI) were selected manually around visually identifiable somata, or complex ROIs were drawn around axons or dendrites and the mean intensity of the ROIs in both the green and the red channel was determined for each frame from the time series using ImageJ (NIH) The background intensity was measured by calculating the mean intensity of a large ROI in an area without any fluorescent structures. For each frame the background intensity was subtracted from the intensity of the ROI of the cell compartment of interest. For the *in vivo* visual stimulation F_0 was calculated as an average of the (ROI intensity – background intensity) for the initial 25 frames baseline period before the beginning of the light flashes. The change in fluorescence was measured as $\Delta F/F_0$, where $\Delta F=F_{(t)} - F_0$. For the *ex vivo* pharmacological preparation for each time point the following ratio (R) was calculated: $R = \frac{(ROI-background)_{red}}{(ROI-background)_{green}}$. R_0 was calculated as an average of R during the initial 37 s baseline before application of drug. The change of fluorescence intensity was measured as $\Delta R/R_0$, where $\Delta R = R_{(t)}-R_0$.

Chapter 4 Red fluorescent genetically encoded Ca^{2+} indicators with low affinities for use in mitochondria and endoplasmic reticulum[4]

[4] A version of this chapter has been accepted for publication as J. Wu, D. L. Prole, Y. Shen, Z. Lin, A. Gnanasekaran, Y. Liu, L. Chen, H. Zhou, S. R. W. Chen, Y. M. Usachev, C. W. Taylor and R. E. Campbell, "Red fluorescent genetically encoded Ca^{2+} indicators for use in mitochondria and endoplasmic reticulum", *Biochem. J.* Immediate Publication, doi:10.1042/BJ20140931, (2014). I was responsible for the concept formation, rational design of LAR-GECO1 and 1.2, directed evolution of LAR-GECO1.2 and HeLa cells imaging of ER-LAR-GECO1 and GCaMP3, data collection and analysis, and was contributed to the composition of the manuscript.

4.1 Introduction

As a ubiquitous second messenger, Ca^{2+} has essential physiological roles in a variety of cellular processes including muscle contraction, propagation of action potentials, fertilization, and development (*199*). The development and subsequent application of genetically encoded Ca^{2+} indicators based on FPs revolutionized the study of intracellular Ca^{2+} dynamics. There are two predominant classes of FP-based Ca^{2+} indicators: the cameleon-type based on FRET; and the GCaMP-type based on a single cpFP. Cameleon-type Ca^{2+} indicators are composed of a genetic fusion of the Ca^{2+} binding domain CaM and a short peptide known as M13, flanked by a blue-shifted donor FP and a red-shifted acceptor FP. As FRET is strongly distant dependent, the Ca^{2+}-dependent interaction of CaM and M13 leads to a change in FRET efficiency and a ratiometric change in the fluorescence signal (*3*). GCaMP-type indicators consist of a cpFP genetically fused to an N-terminal M13 peptide and a C-terminal CaM domain (*1*, *2*). The Ca^{2+} interaction of CaM and M13 modifies the FP chromophore environment such that the fluorescent brightness undergoes an intensiometric increase.

The cameleon and GCaMP designs are each associated with specific advantages and disadvantages. GCaMP-type indicators benefit from larger signal changes and a wider range of available fluorescence hues (*144*, *146*, *162*, *200*, *201*). Cameleons tend to have smaller signal changes at any one wavelength, but this is compensated for by the fact that the responses are inherently ratiometric. Of particular relevance to this work, cameleons have traditionally also been more amenable to genetic 'tuning' of the K_d values to provide variants optimized for use in low (*202*) or high (*203*–*205*) Ca^{2+} concentration

environments. Accordingly, certain cameleon-type Ca^{2+} indicators have proven to be particularly useful for imaging of Ca^{2+} dynamics in the high Ca^{2+} concentration environments of the ER and sarcoplasmic reticulum (SR) lumens (*3*, *203*, *206*). These organelles are the intracellular Ca^{2+} reservoirs in eukaryotic organisms and are therefore play central roles in Ca^{2+} signaling (*199*, *207*, *208*).

Although a number of improved cameleon- and GCaMP-type indicators have been reported during the last decade, there remain only a limited number of examples of variants optimized for use in high Ca^{2+} environments of the ER or SR (*207*, *209*). Likewise, there are also relatively few variants optimized for use in the mitochondria, where Ca^{2+} concentrations can change over three orders of magnitude (from ~0.1 μM to ~100 μM) (*204*, *210*, *211*). Of those indicators that have been reported, they are all of the cameleon type. One reason for the lack of appropriate GCaMP-type indicators is that their K_d values ranges from ~100 nM to a few micromolar, and so they are limited to detecting changes in the same concentration range. Furthermore, due to the more intricate sensing mechanism of GCaMP-type indicators, mutations in the CaM domain that could potentially increase the K_d of the indicator are also likely to interfere with the fluorescence modulation mechanism. Indeed, our own previous efforts to decrease the Ca^{2+} affinity of GCaMP-type indicators have been hampered by corresponding, and seemingly unavoidable, dramatic decreases in the performance of the indicator.

Efforts to engineer cameleon-type indicators with decreased Ca^{2+} affinity have been more successful, as illustrated by the example of the popular D1ER (*203*) and D4cpv (*204*) indicators. The Ca^{2+}-sensing domain of both D1ER and D4cpv were engineered by redesigning the interaction between CaM and M13 such that they would interact with each other but not endogenous binding partners. While

the redesign successfully produced an orthogonal CaM plus M13 pair, it also decreased the apparent affinity for Ca^{2+} to ~60 μM for both indicators. However, as this FRET-based Ca^{2+} indicator contains both a cyan and a yellow fluorescent protein, it is generally impractical for combined use with GFP variants in multi-colour imaging. More recently, a green Ca^{2+} indicator, CatchER, based on a single green FP (GFP) was reported (*92*). In this design, three β-strands in GFP were engineered to bind to Ca^{2+} and change the fluorescence intensity of the protein upon binding to Ca^{2+}. Nevertheless, CatchER only displays ~1 fold fluorescence change upon Ca^{2+} binding, which can potentially compromise its sensitivity to Ca^{2+}. Moreover, both of the above Ca^{2+} indicators require the use of blue light for excitation, which leads to higher levels of autofluorescence and phototoxicity. Accordingly, there remains a substantial need for red FP (RFP)-based Ca^{2+} indicators optimized for imaging of Ca^{2+} dynamics in high Ca^{2+} concentration organelles, such as in ER, SR, or mitochondria. There are a number of inherent benefits to longer wavelength indicators (i.e., red as opposed to green fluorescent) as longer wavelength excitation light is associated with lower background fluorescence, lower phototoxicity, and deeper tissue penetration.

In this Chapter, I will describe the engineering of a series of RFP-based Ca^{2+} indicators for detecting mitochondrial and ER Ca^{2+} dynamics by rational design and directed evolution. These new indicators show high sensitivity in organelles with high Ca^{2+} concentrations, such as mitochondria and ER lumen, and are useful for multi-color imaging when paired with green fluorescent indicators.

4.2 Results and discussion

4.2.1 Engineering of LAR-GECO1 and LAR-GECO1.2

To engineer new Ca^{2+} sensors with low affinity, we chose three single RFP-based Ca^{2+} indicators, R-GECO1 (K_d = 0.48 μM) (*144*), R-GECO1.2 (K_d = 1.2 μM) (*162*), and RCaMP1h (K_d = 1.3 μM) (*146*) as templates. We first fused these three indicators with ER-targeting (*212*) and ER-retention sequence (*213*), and expressed them in HeLa cells to check their localization. All three indicators showed the expected pattern of localization for the ER of HeLa cells, however, the fluorescence intensities were very low compared to their cytosolic expression under the same condition. We suspected that the diminished performance and brightness of these indicators might due to interactions between the CaM-M13 moieties and endogenous protein or peptide binding partners, as previously proposed for cameleon-type indicators (*214*, *215*). In an effort to circumvent this problem, we explored the engineering orthogonal CaM-M13 pairs in R-GECO1 and R-GECO1.2 by mutagenesis of residues involved in interactions at the CaM-M13 interface. In addition, we reasoned that disruption or modification of interactions at this interface could potentially decrease the K_d of the Ca^{2+} sensor. To test this idea, mutations were introduced following three different strategies: (1) incorporation of four point mutations (Val51Trp, Phe395Ala, Val411Ala and Leu415Ile; GCaMP numbering as in the PDB file 3EVR (*96*); Figure 4.1) from the computationally designed D4 CaM-M13 pair into R-GECO1 (*204*); (2) library creation by randomization of Ala47 of R-GECO1.2 (together with point mutation Asn45Ile from O-GECO1 (*162*)) with the reasoning that mutating Ala47 could alter the interactions between this residue to the pocket formed by Phe395, Met412 and Leu415 (Figure 4.1) from the third EF-hand of CaM; and (3) library

creation by randomization of Leu57 in R-GECO1 with the reasoning that mutating Leu57 could potentially lead to new interactions of this residue to Met354, Phe366 or Met374 (Figure 4.1). Variants generated from the above strategies were expressed in *E. coli* colonies and screened for red fluorescence and tested for Ca^{2+} response and affinity.

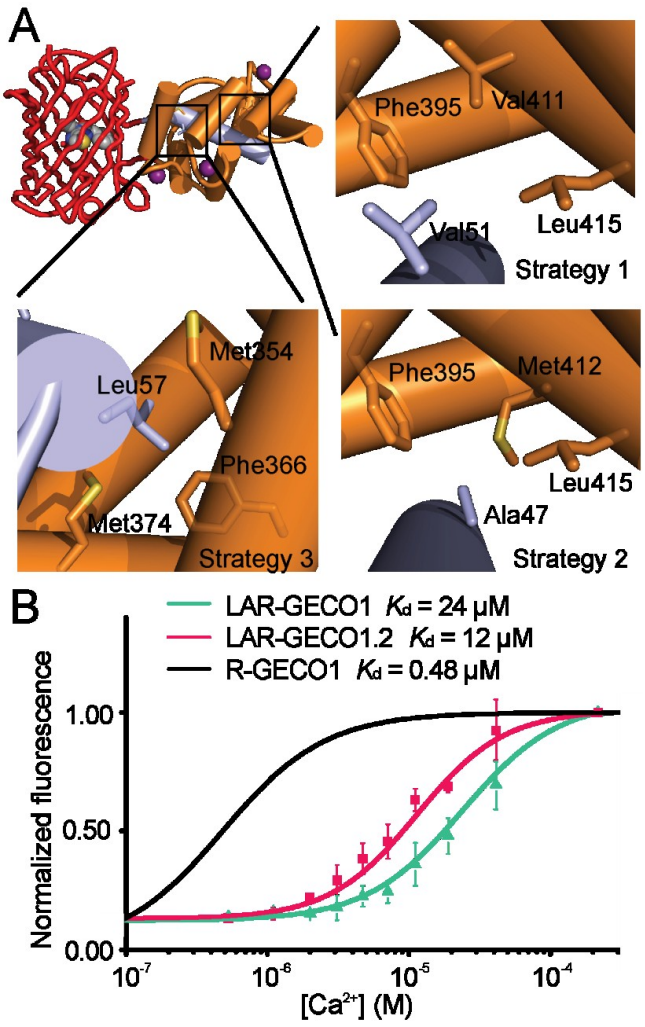

Figure 4.1. Strategies and dissociation constant for LAR-GECO1 and LAR-GECO1.2. (A) Strategy 1, 2 and 3 for making orthogonal CaM (yellow)-M13 (grey) pairs with side chains shown in stick format in R-GECO1 (PDB ID 4I2Y) (*146*). (B)

Normalized fluorescence intensity of LAR-GECO1, LAR-GECO1.2 and R-GECO1 as a function of free Ca^{2+} concentration in buffer (10 mM MOPS, 100 mM KCl, pH 7.2).

Incorporation of the D4 mutations into R-GECO1 (strategy 1) produced a variant, designated as low affinity R-GECO0.1 (LAR-GECO0.1), with a K_d of ~20 μM and a ~10-fold fluorescence intensity increase upon binding to Ca^{2+}. From the R-GECO1.2 Ala47X library (strategy 2) we identified a variant, designated LAR-GECO0.2 (R-GECO1.2 with Asn45Ile and Ala47Arg), with a K_d of ~8 μM and a ~15-fold fluorescence intensity increase upon Ca^{2+} binding. From the R-GECO1 Leu57X library (strategy 3) we identified many functional variants, but none with substantially higher K_d values than R-GECO1. This suggests that modifying Leu57 does not significantly alter the Ca^{2+} affinity or the interactions between CaM and M13.

In an effort to further improve the brightness of LAR-GECO0.1 and LAR-GECO0.2, we performed three and two rounds, respectively, of directed evolution with selection for variants with bright fluorescence. Specifically, we performed random mutagenesis on LAR-GECO0.1 and LAR-GECO0.2 in the pBAD/His B vector (Life Technologies), followed by a colony-based screen for high red fluorescence intensity colonies (with excitation filter 560/40 nm and emission filter 630/60 nm). Selected protein variants were extracted from bacterial cultures and tested for both the magnitude of their response to Ca^{2+} as well as their K_d to Ca^{2+}. Three to five functional variants with bright red fluorescence and K_d ~10 μM or higher were then used as templates for the next round of directed evolution. Our

efforts led to the identification of LAR-GECO1 (derived from LAR-GECO0.1) with 7 mutations compared with R-GECO1, a K_d to Ca^{2+} of 24 μM and a 10-fold fluorescence intensity increase upon binding to Ca^{2+} (dynamic range), and LAR-GECO1.2 (derived from LAR-GECO0.2) with 4 mutations compared with R-GECO1.2, a K_d for Ca^{2+} of 12 μM, and a dynamic range of 8.7 (Figures 4.1B, 4.2 and Tables 4.1, 4.2).

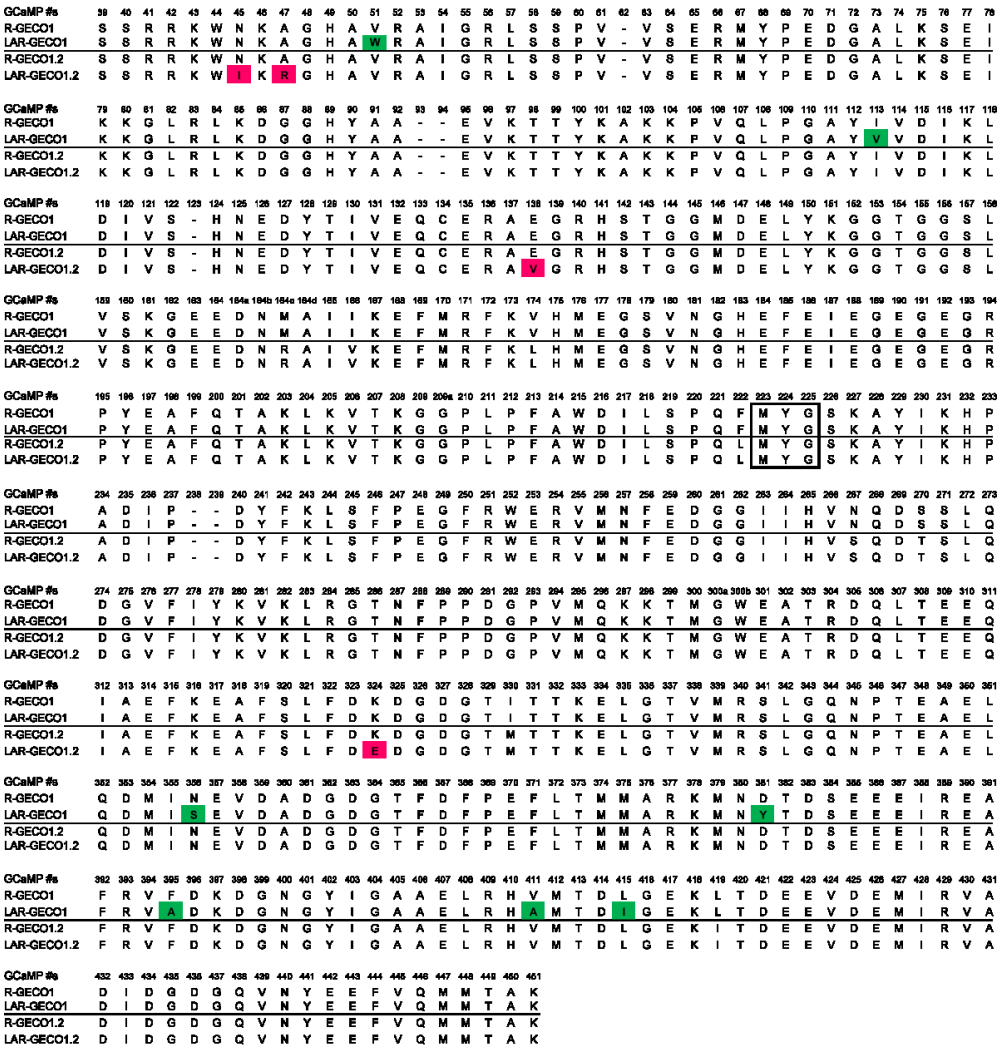

Figure 4.2. Sequence alignment of R-GECO1, LAR-GECO1, R-GECO1.2 and LAR-GECO1.2. Changes in LAR-GECO1 relative to R-GECO1 are shown as green boxes, in LAR-GECO1.2 relative to R-GECO1.2 are shown as pink boxes.

Residue numbering is consistent with the crystal structure of G-CaMP2 (PDB ID 3EVR) (*96*).

Table 4.1. List of substitutions for new GECOs described in this work. Residues are numbered as described in **Figure 4.2.**

Protein	LAR-GECO1's substitutions relative to R-GECO1 LAR-GECO1.2's substitutions relative to R-GECO1.2
LAR-GECO1	V51W, I113V, N356S, D381Y, F395A, V411A, L415I
LAR-GECO1.2	N45I, A47R, E138V, K324E

Table 4.2. Properties of new GECOs described in this work.

Protein	Ca^{2+}	λ_{abs} (nm) (ε) ($mM^{-1}\cdot cm^{-1}$)	λ_{em} (nm) (Φ)	Brightness[1] ($mM^{-1}\cdot cm^{-1}$)	pK_a	Intensity change ± Ca^{2+}	K_d for Ca^{2+} (μM), (Hill coefficient)
LAR-GECO1	-	574 (5.3)	598 (0.13)	0.69	8.6	10×	24 (1.3)
	+	561 (35.8)	589 (0.20)	7.2	5.4/8.8[2]		
LAR-GECO1.2	-	570 (3.6)	594 (0.18)	0.65	9.0	8.7×	12 (1.4)
	+	557 (16.5)	584 (0.34)	5.6	5.8/8.9[2]		
LAR-GECO2	-	574 (5.0)	598 (0.13)	0.65	8.9	5.7×	60 (1.2)
	+	561 (19.7)	589 (0.19)	3.7	6.4/9.0[2]		
LAR-GECO3	-	574 (5.5)	598 (0.11)	0.61	9.4	7.5×	110 (1.1)
	+	561 (23.2)	589 (0.20)	4.6	5.9/8.8[2]		
LAR-GECO4	-	574 (5.3)	598 (0.10)	0.53	9.1	13×	>540 (1.2)
	+	561 (35.2)	589 (0.19)	6.7	6.5/8.8[2]		

[1]Brightness is defined as the product of ε and Φ. [2]In the Ca^{2+}-bound state, all LAR-GECOs show biphasic p*K*a.

4.2.2 Engineering of non-cp LAR-GECOs

Even though LAR-GECO1 has a reasonably low Ca^{2+} affinity of 24 μM, and exhibits correct ER-localization in HeLa cells, its Ca^{2+} K_d might not be optimal for detecting the Ca^{2+} dynamics in high Ca^{2+} environments of the ER or SR (*207*, *209*). Furthermore, there are numerous endogenous proteins in the ER or SR that might interact with CaM or M13 of the Ca^{2+} indicator. To address this problem, we reasoned that by fusing the N-terminus of M13 to the C-terminus of CaM by a short polypeptide linker will limit the freedom of both modules and create a certain steric hindrance to prevent them from interacting with endogenous proteins. To test this idea, we applied circularly permutation to LAR-GECO1 by using a Gly-Gly-Gly-Gly-Ser linker to fuse the N-terminus of M13 to the C-terminus of CaM and created a new N- and C-termini between position 151 and 159 (Figure 4.2), the resulting variant was named as non-cp LAR-GECO1. Non-cp LAR-GECO1 shares the same *in vitro* performance to LAR-GECO1, which suggests linker M13 to CaM does not perturb the function of the Ca^{2+} indicator.

To engineer red Ca^{2+} indicators with lower affinity for detecting the Ca^{2+} dynamics in the ER or SR, we explored the possibility of tuning the apparent K_d of non-cp LAR-GECO1 by altering its CaM-M13 interaction or by changing its CaM's affinity to bind Ca^{2+}. Specifically, mutations based on the following three rationales were introduced to non-cp LAR-GECO1, respectively (Figure 4.3): (1) Alanine-scanning of the CaM-M13 interface to weaken their interactions (Table 4.3); (2) incorporation of mutations from previously reported Ca2+ indicators to decrease the apparent K_d (Table 4.3); (3) incorporation of mutations in the EF-hands in CaM, and combine with strategy (2) to decrease its Ca^{2+} affinity (Table

4.3). The resulting variants were then expressed in *E.coli* colonies and tested for their Ca^{2+} response and affinity.

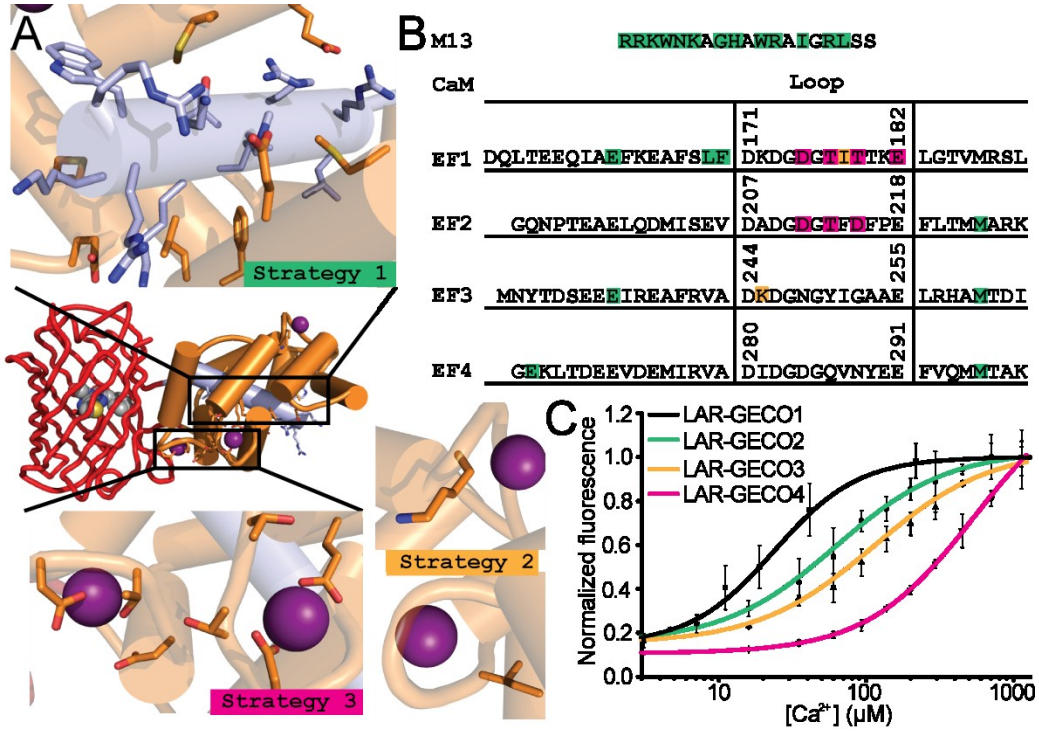

Figure 4.3. Strategies and dissociation constant for LAR-GECO2, LAR-GECO3, and LAR-GECO4. (A) Strategy 1, 2, and 3 for tuning the Ca^{2+} affinity of non-cp LAR-GECO1. (B) Residues targeted based on strategies 1, 2, and 3 in (A), residues are numbered as described in Figure 4.4. (C) Normalized fluorescence intensity of LAR-GECO1, LAR-GECO2, LAR-GECO3, and LAR-GECO4 as a function of free Ca^{2+} concentration.

Table 4.3. Mutations introduced into non-cp LAR-GECO1. Residues are numbered as described in **Figure 4.4**.

Strategy	Variant	Mutations	Reference
Strategy 1 Alanine-scanning M13-CaM interface	M01	R309A	This work
	M02	R310A	This work
	M03	K311A	This work
	M04	W312A	This work
	M05	N313A	This work
	M06	K314A	This work
	M06	G316A	This work
	M08	H317A	This work
	M09	W319A	This work
	M10	R320A	This work
	M11	I321A	This work; designated as **LAR-GECO2**
	M12	R323A	This work
	M13	L324A	This work
	M14	E162A	This work
	M15	L169A	This work
	M16	F170A	This work
	M17	M223A	This work
	M18	E235A	This work
	M19	M260A	This work
	M20	E265A	This work
	M21	M296A	This work
Strategy 2 CaM mutations from O-GECO1 and R-GECO1.2	M22	I178M	R-GECO1.2; designated as **LAR-GECO3**
	M23	K245N	O-GECO1
Strategy 3 mutations in the EF-hands of CaM	M24	T177D/T213D/D215N	Fast GCaMPs
	M25	T213D/D215N	Fast GCaMPs
	M26	T177D /T179D/ T213D	Fast GCaMPs
	M27	T211D	Fast GCaMPs
	M28	T177D/T179D	Fast GCaMPs
	M29	D211N/D215N	Fast GCaMPs
	M30	D175N/ I178M	Fast GCaMPs and R-GECO1.2
	M31	D175N/ I178M/D211N	Fast GCaMPs and R-GECO1.2; designated as **LAR-GECO4**
	M32	E182A	Fast GCaMPs
	M34	T213D	Fast GCaMPs

In the alanine-scanning library, we identified a variant that harbors a mutation of Ile321Ala with a Ca^{2+} K_d of 60 μM (Figure 4.4, Table 4.2 and 4.4) while still enjoys a Ca^{2+} response of 5.7-fold. We designated this variant as LAR-GECO2. When testing the library of non-cp LAR-GECO1 with different mutations from previously reported GECOs, we found a single mutation, Ile178Met, can decrease its Ca^{2+} affinity from 24 μM to 110 μM (Figure 4.4, Table 4.2 and 4.4). This new variant has a Ca2+ response of 7.5-fold, and was designated as LAR-GECO3. In the last library of non-cp LAR-GECO1 with modified EF-hands combining mutations from strategy (2), a variant with a drastically decreased K_d of more than 540 μM, was discovered. This variant harbors mutations Asp175Asn/ Ile178Met/Asp211Asn was later named as LAR-GECO4, which exhibits a Ca^{2+} response of 13-fold *in vitro* (Figure 4.4, Table 4.2 and 4.4). In addition, all three newly discovered LAR-GECOs were express in HeLa cells and all of them showed correct ER-localization and bright red fluorescence.

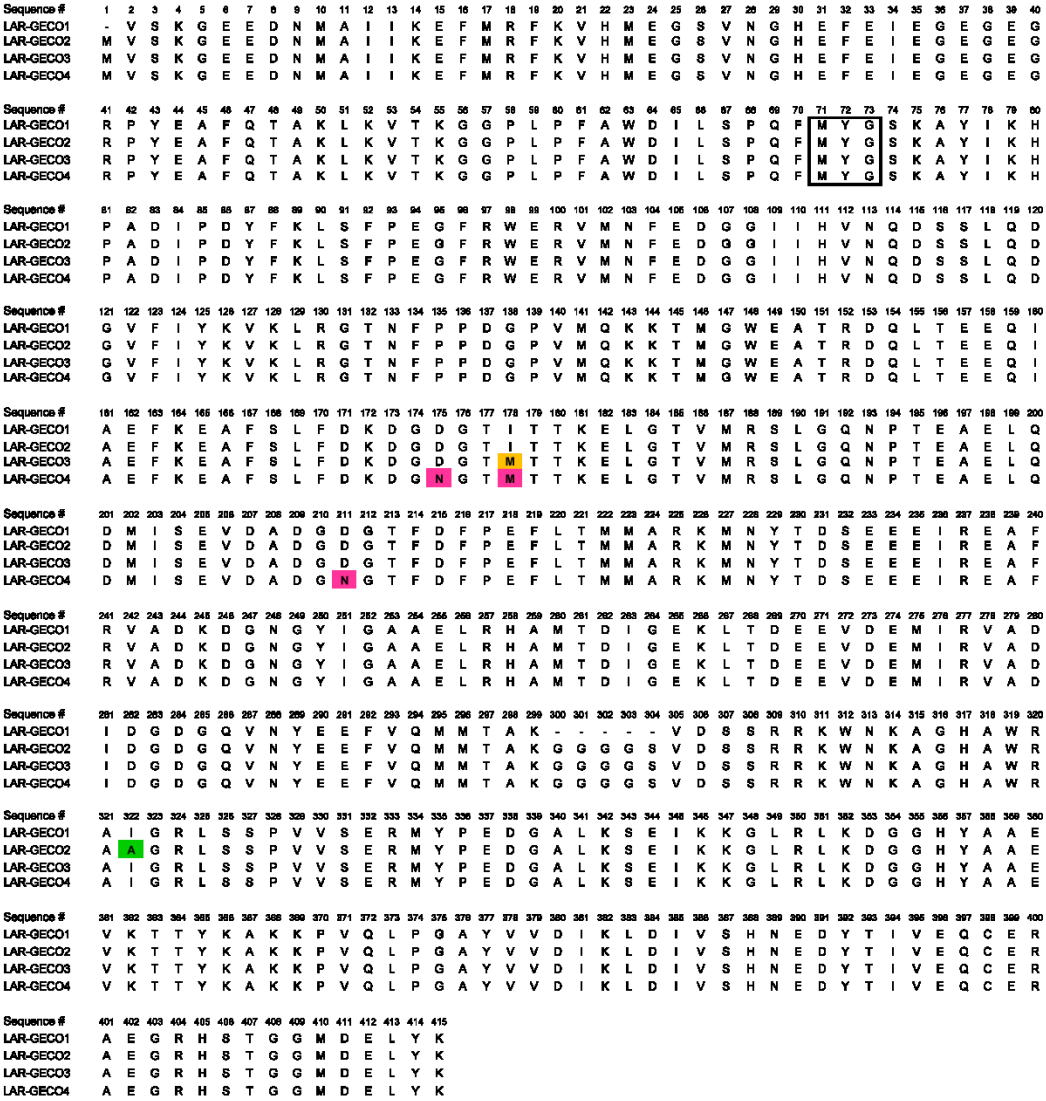

Figure 4.4. Sequence alignment of non-cp LAR-GECO1, LAR-GECO2, LAR-GECO3, and LAR-GECO4. Changes in LAR-GECO2, LAR-GECO3, and LAR-GECO4 relative to non-cp LAR-GECO1 are shown as green, orange, and pink boxes, respectively.

Table 4.4. List of substitutions for new GECOs described in this work. Residues are numbered as described in **Figure 4.4**.

Protein	Substitutions relative to non-cp LAR-GECO1
LAR-GECO2	I321A
LAR-GECO3	I178M
LAR-GECO4	D175N, I178M, D211N

4.2.3 *In vitro* characterization

Undergraduate researchers, Hang Zhou and Lidong Chen, performed systematic *in vitro* characterization of LAR-GECO1 and LAR-GECO1.2. It revealed that both proteins had similar spectral properties to their progenitors R-GECO1 and R-GECO1.2, respectively (Figure 4.5, Table 4.2). In addition, LAR-GECO1 and LAR-GECO1.2 exhibit monophasic pH dependences with apparent pK_as of 8.6 and 9.0, respectively, in the Ca^{2+}-free state. In the Ca^{2+}-bound state both proteins exhibited a biphasic pH dependence with apparent pK_as of 5.4/8.8 and 5.8/8.9, respectively (Figure 4.5BF, Table 4.2). As a result, both these Ca^{2+} indicators show high fluorescence change around physiological pH, yet these fluorescence changes decrease significantly at pH values lower than 6 or higher than 8.

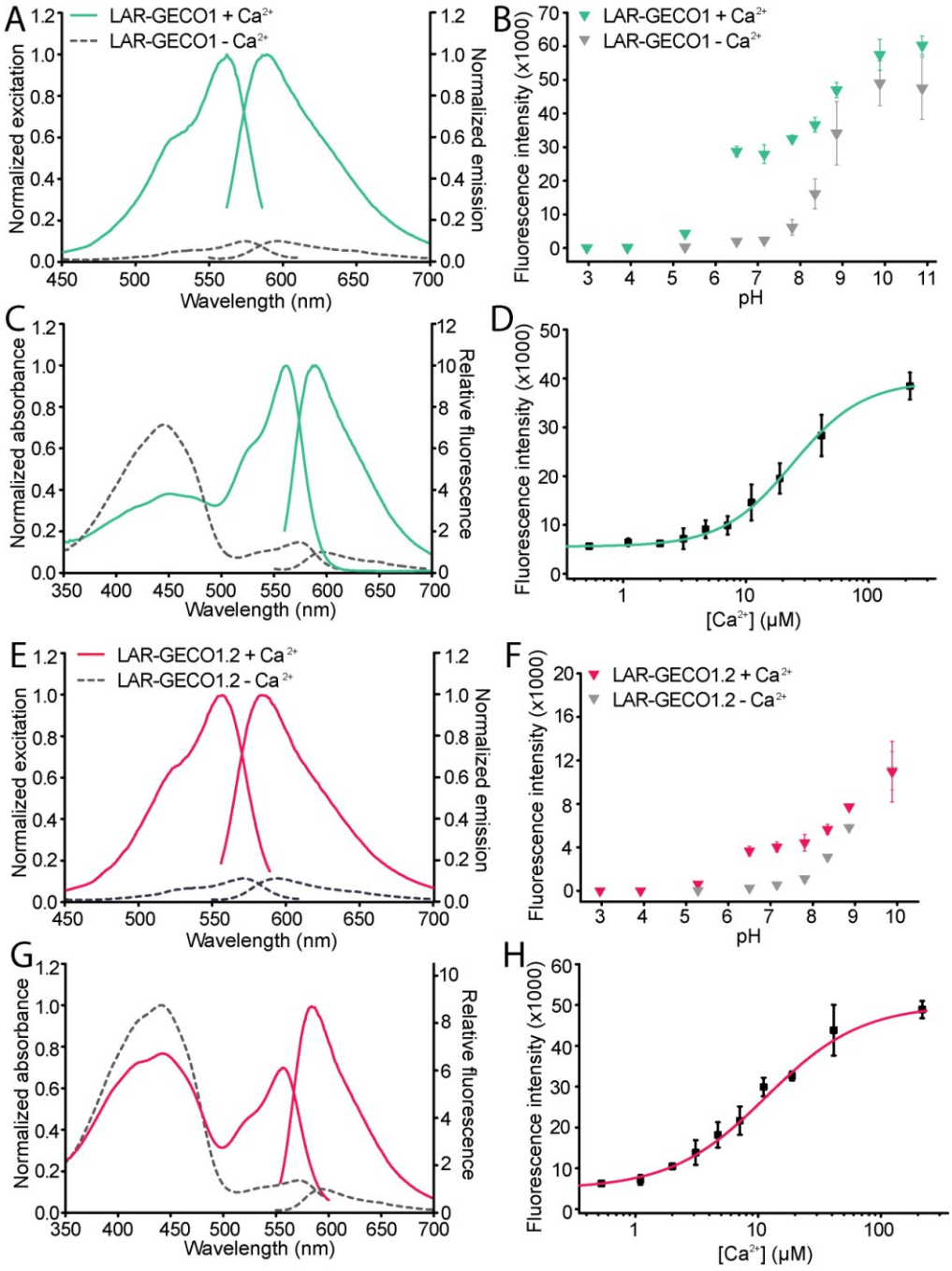

Figure 4.5. Characterization of LAR-GECO1 and LAR-GECO1.2. (A and E) Excitation and emission spectra of LAR-GECO1 (A) and LAR-GECO1.2 (E). (C and G) Absorbance and emission spectra of LAR-GECO1 (C) and LAR-GECO1.2 (G) in both the Ca^{2+}-free state and the Ca^{2+}-bound state. (B and F) Fluorescence intensity of LAR-GECO1 (B) and LAR-GECO1.2 (F) as a function

of pH. (D and H) Fluorescence intensity of LAR-GECO1 (D) and LAR-GECO1.2 (H) as a function of free Ca^{2+}.

Furthermore, *in vitro* characterization on LAR-GECO2, LAR-GECO3, and LAR-GECO4 showed that all of these three non-cp Ca^{2+} indicators share identical spectral properties with their progenitor, LAR-GECO1 (Figure 4.6, Table 4.2). Besides spectral properties, these non-cp LAR-GECOs also exhibit a similar monophasic dependence on pH in the Ca^{2+}-free state (Figure 4.6, Table 4.2). Upon binding to Ca^{2+}, this dependence on pH switches from monophasic to biphasic, which is very similar to LAR-GECO1's (Figure 4.6, Table 4.2).

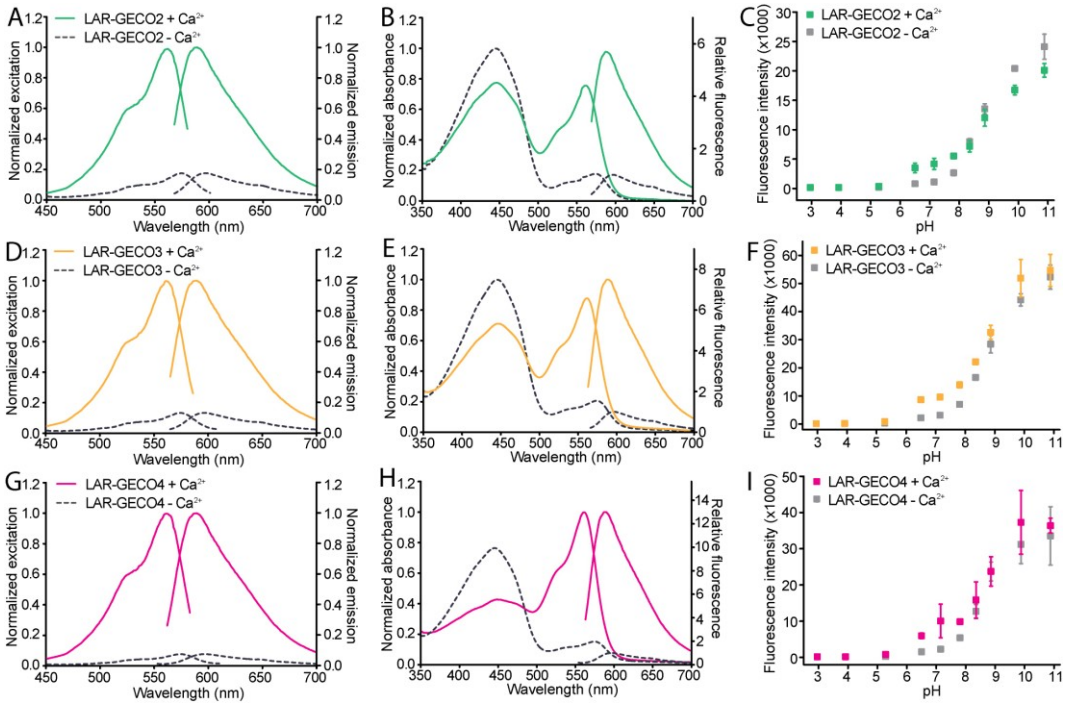

Figure 4.6. Characterization of LAR-GECO2, LAR-GECO3, and LAR-GECO4. (A, D, and G) Excitation and emission spectra of LAR-GECO2 (A), LAR-GECO3 (D),

and LAR-GECO4 (G). (B, E and H) Absorbance and emission spectra of LAR-GECO2 (B) and LAR-GECO3 (E), and LAR-GECO4 (H) in both the Ca^{2+}-free state and the Ca^{2+}-bound state. (C, F, and I) Fluorescence intensity of LAR-GECO2 (C), LAR-GECO3 (F), and LAR-GECO4 (I) as a function of pH.

The decreased Ca^{2+} affinity of LAR-GECO1 (24 μM) compared with its progenitor, R-GECO1 (0.48 μM), is mainly attributed to the D4 mutations (Val51Trp, Phe395Ala, Val411Ala and Leu415Ile) as they create a new complementary bump and hole interaction between M13 and CaM (*204*). In LAR-GECO1.2, we attributed the 10-fold decreased Ca^{2+} affinity (from 1.2 μM to 12 μM) to the single mutation, Ala47Arg, as the bulky and hydrophilic Arg47 residue would perturb the interactions originally present between the side chain of Ala47 and the pocket formed by Phe395, Met412 and Leu415 from the third EF-hand of CaM.

Since the change of topology from LAR-GECO1 to non-cp LAR-GECO1 does not change its affinity to Ca^{2+}, we attribute the decrease of Ca^{2+} affinity of LAR-GECO2 to the single point mutation, Ile321Ala. In the x-ray crystal structure of the Ca^{2+}-bound R-GECO1 (*146*), Ile321 is pointing to a potential binding pocket formed by Met187, Leu190, and Gln192 from CaM. Mutating this relatively bulky Ile residue to a small Ala residue might potentially weaken the interaction between M13 and CaM in the Ca^{2+}-bound state, which leads to a decrease of Ca^{2+} affinity. In LAR-GECO3, mutating Ile178 to Met in the loop of the first EF-hand in CaM might potentially alter the Ca^{2+} binding affinity, which is consistent with the decreased Ca^{2+} affinity of R-GECO1.2 from R-GECO1 (*162*). In LAR-GECO4, the drastic decreased of affinity comes from the combination of removal

of the acidic chelating residues in the first and second EF-hands of CaM (*216*) and the Ile178Met from R-GECO1.2 (*162*).

4.2.4 Dual-color ER and cytosolic Ca^{2+} imaging using LAR-GECO1

To explore the possibility of using LAR-GECO1 and a green fluorescent indicator for dual-color imaging of the cytosolic and ER luminal Ca^{2+} dynamics, we co-expressed a green, cytosolic Ca^{2+} indicator, GCaMP3 (*217*) (henceforth termed Cyto-GCaMP3), and ER-LAR-GECO1 in cells. Co-expression of both ER-LAR-GECO1 and Cyto-GCaMP3 in HeLa cells showed correction localization (Figure 4.7). Upon stimulation of histamine, we observed simultaneous increase of the green channel (Cyto-GCaMP3) and decrease of the red channel (ER-LAR-GECO1) (Figure 4.7), which indicates the Ca^{2+} oscillations between the ER and cytosol of HeLa cells.

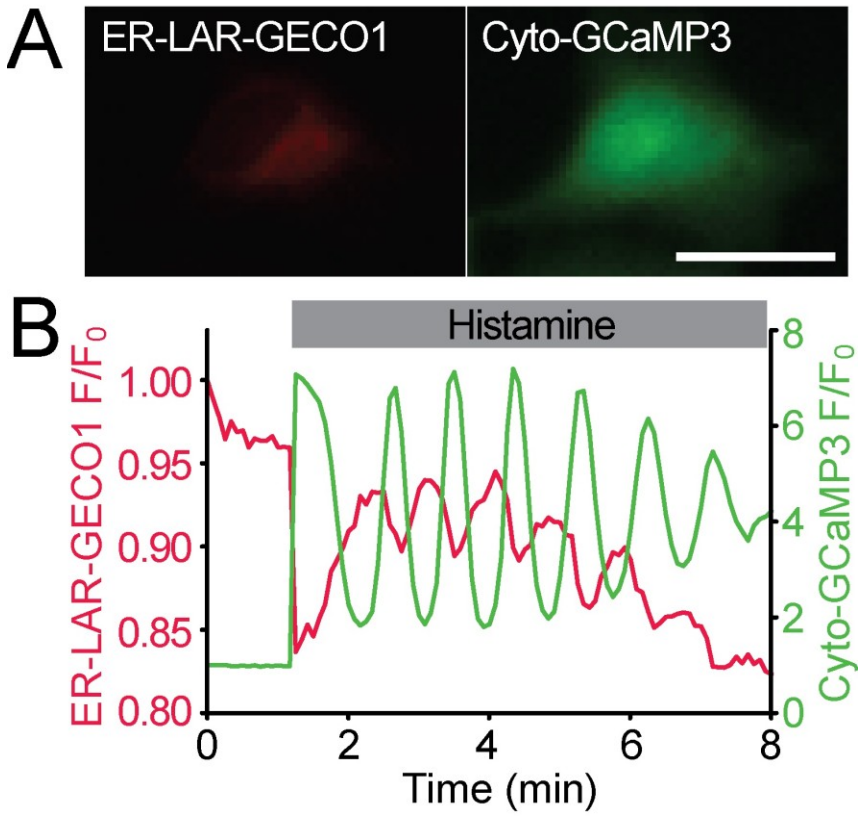

Figure 4.7. Dual-color imaging of cytosolic and ER luminal Ca^{2+} using ER-LAR-GECO1 and Cyto-GCaMP3. (A) A HeLa cell co-expressing ER-LAR-GECO1 (left panel) and Cyto-GCaMP3 (right panel). Scale bar = 20 μm. (B) Change of fluorescence intensity of ER-LAR-GECO1 (pink trace) and Cyto-GCaMP3 (green trace) of the HeLa cell in (A) upon treatment of histamine.

4.2.5 Imaging LAR-GECO1.2 in mitochondria of neurons

With an affinity to Ca^{2+} of 12 μM, we reasoned that LAR-GECO1.2 would be optimal for detecting the Ca^{2+} dynamics in the mitochondria, which usually has Ca^{2+} changes from ~0.1 μM to ~100 μM (*204*, *210*, *211*). Neuronal mitochondria efficiently buffer Ca^{2+} influx during excitation via the Ca^{2+} uniporter, and then release Ca^{2+} back into the cytosol via Na^{+}/Ca^{2+} and H^{+}/Ca^{2+} exchangers, which

results in transient elevations of mitochondrial Ca^{2+} concentration ($[Ca^{2+}]_{mt}$) during neuronal activity (*218*, *219*). These mitochondrial Ca^{2+} signals play important role in the ATP synthesis, neuronal plasticity and survival (*220*, *221*), and these $[Ca^{2+}]_{mt}$ transients can be detected using Ca^{2+}-sensitive probes. Thus, to further characterize LAR-GECO1.2 in the cellular systems, our collaborators, Zhihong Lin, Aswini Gnanasekaran, from Dr. Yuriy M. Usachev's group at the University of Iowa, performed measurements of $[Ca^{2+}]_{mt}$ in cultured peripheral and central neurons using a mitochondria-targeted LAR-GECO1.2 (mito-LAR-GECO1.2). To provide additional control for neuronal responses to depolarization and glutamate, $[Ca^{2+}]_{mt}$ signals were monitored simultaneously with cytosolic Ca^{2+} ($[Ca^{2+}]_i$) using Fura2. Dorsal root ganglion (DRG) sensory neurons were evoked by depolarization pulses of incremental magnitude (15, 20, 30 or 50 mM of extracellular KCl for 30 s), mito-LAR-GECO1.2 and Fura2 were used for measuring $[Ca^{2+}]_{mt}$ and $[Ca^{2+}]_i$, respectively (Figure 4.8AB). As predicted, the mitochondrial Na^+/Ca^{2+} inhibitor CGP37157 (10 μM) slowed Ca^{2+} removal from mitochondria (Figure 4.8A). The effect of CGP37157 was fully reversible. In hippocampal neurons, depolarization or glutamate also produced $[Ca^{2+}]_i$ and $[Ca^{2+}]_{mt}$ elevations, although the amplitudes of $[Ca^{2+}]_{mt}$ increases were smaller than those produced by similar stimuli in DRG neurons (Figure 4.8CD). Overall, our observations using mito-LAR-GECO1.2 are consistent with the known properties of mitochondrial Ca^{2+} transport in neurons (*218*, *221*, *222*).

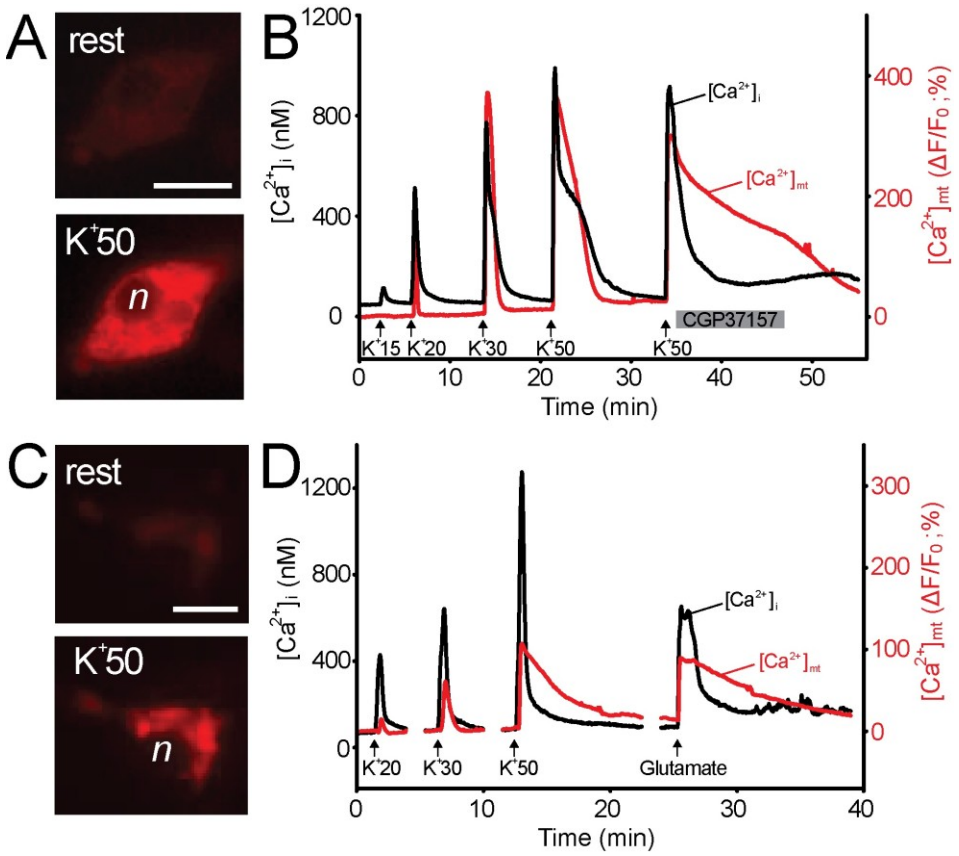

Figure 4.8. LAR-GECO1.2 for imaging mitochondrial Ca^{2+} in DRG and hippocampal neurons. (A) Images show mito-LAR-GECO1.2 fluorescence in a DRG neuron from which recordings were made under resting conditions (top) and at the peak of the $[Ca^{2+}]_{mt}$ response to 50 mM extracellular K^+ (bottom; *n* = nucleus), scale bar = 20 µm. (B) DRG sensory neurons were transfected with a mitochondrially targeted form of LAR-GECO1.2 (mito-LAR-GECO1.2), and subsequently loaded with fura-2 to enable simultaneous measurements of Ca^{2+} concentrations within mitochondria ($[Ca^{2+}]_{mt}$; red trace) and cytosol ($[Ca^{2+}]_i$; black trace). DRG neurons were depolarized using 15, 20, 30 and 50 mM KCl (30 s) in extracellular solution (vertical arrows). The inhibitor of mitochondrial Na^+/Ca^{2+} exchange, CGP37157 (10 µM), reversibly inhibited extrusion of Ca^{2+} from mitochondria (red) and eliminated the $[Ca^{2+}]_i$ plateau that immediately followed

the peak rise in $[Ca^{2+}]_i$ in control cells. (C) Images show mito-LAR-GECO1.2 fluorescence in a hippocampal neuron from which recordings were made in the resting state (top) and at the peak elevation of $[Ca^{2+}]_{mt}$ induced by 50 mM extracellular K^+ (bottom; *n* = nucleus), scale bar = 10 μm. (D) Simultaneous imaging of cytosolic ($[Ca^{2+}]_i$, black) and mitochondrial ($[Ca^{2+}]_{mt}$, red) concentrations of Ca^{2+} in mouse hippocampal neurons using fura-2 and mito-LAR-GECO1.2, respectively. Elevation of $[Ca^{2+}]_i$ and $[Ca^{2+}]_{mt}$ were induced by 30-s depolarizations evoked by KCl (20, 30 or 50 mM) or 100 μM glutamate (+10 μM glycine). 200 nM tetrodotoxin was present throughout the recordings to block action potentials.

4.2.6 Detecting store overload-induced Ca^{2+} release using LAR-GECO3

To further investigate the utility of the non-cp LAR-GECOs, our collaborator, Yingjie Liu, from Dr. Wayne Chen's group expressed LAR-GECO3 in the ER of HEK-293 for monitoring the ER luminal Ca^{2+} dynamics. We chose LAR-GECO3 with a K_d to Ca^{2+} of 110 μM, reasoning that this Ca^{2+} affinity might be most suitable for the high Ca2+ concentration dynamics within the ER lumen. HEK-293 cells stably expressing ryanodine receptor 2 (RyR2) were transiently transfected with ER-LAR-GECO3 (LAR-GECO3 with ER-targeting and ER-retention sequence). By perfusing with elevating extracellular Ca^{2+} (from 0.0-2.0 mM), we observed store overload-induced Ca^{2+} release (SOICR) as transient decrease of red fluorescence of ER-LAR-GECO3 (Figure 4.9). Overall, we demonstrate that ER-LAR-GECO3 is capable of monitoring ER Luminal Ca^{2+} in RyR2-expressing HEK-293 cells.

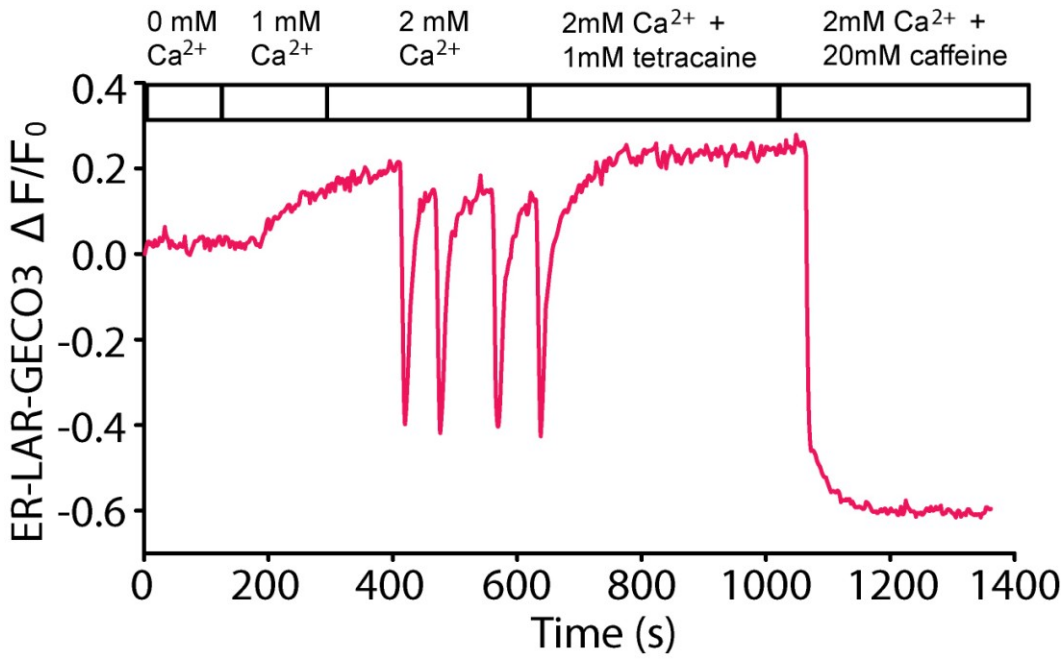

Figure 4.9. LAR-GECO3 in RyR2-expressing HEK-293 cells. Changes of fluorescence intensity of ER-LAR-GECO3 from a HEK-293 cell expressing RyR2. This HEK-293 cell was first perfused with elevating extracellular Ca^{2+} (from 0.0-2.0 mM) to induce store overload-induced Ca^{2+} release (SOICR). Perfusion of 2 mM Ca^{2+} and 1 mM tetracaine was then followed to block the Ca^{2+} release from the ER store. 2 mM Ca^{2+} and 20 mM caffeine were last applied to induce Ca^{2+} depletion from the ER store.

4.3 Conclusion

By utilizing rational design and directed evolution, we have developed a series of low-affinity red fluorescent Ca^{2+} indicators with K_d values for binding to Ca^{2+} ranging from 12 μM and more than 540 μM, respectively. These indicators enable robust detection of Ca^{2+} dynamics in organelles containing relatively high Ca^{2+} concentrations, as we demonstrate for the mitochondria in primary neurons and the ER in cultured human cells. Furthermore, LAR-GECO1 enables

simultaneous dual-color imaging with GFP-based fluorescent probes. We expect that these new series of LAR-GECOs will open up new avenues for interrogating Ca^{2+} dynamics during cell signaling and their roles in cell biology.

4.4 Materials and methods

4.4.1 Engineering of LAR-GECOs

R-GECO1 and R-GECO1.2 in pTorPE1 (*144*) were used as the initial templates for engineering LAR-GECOs. Point mutations and randomizations of specific amino acid were introduced using Quikchange Lightning Site-Directed Mutagenesis Kit (Agilent) as per manufacturer's instructions. Oligonucleotides containing specific mutations were designed in the aid of Agilent online mutagenesis primer design program. Random mutagenesis was performed by error-prone PCR amplification. To construct mammalian expression plasmids, LAR-GECOs in pBAD/His B vector (Life Technologies) were used as the templates. The ER targeted GECO genes were generated using primers containing ER targeting sequence (MLLPVLLLGLLGAAAD) (*212*) and ER retention signal sequence (KDEL) (*213*). The PCR products were subjected to digestion with the BamHI and EcoRI restriction enzymes (Thermo). The digested DNA fragments were ligated with a modified pcDNA3 plasmid that had previously been digested with the same two enzymes. For mito-LAR-GECO1.2, 2 copies of the targeting sequence (MSVLTPLLLRGLTGSARRLPVPRAKIHSLGDP) from cytochrome c oxidase VIII was added to the 5' end of LAR-GECO1.2. Plasmids were purified with the GeneJET miniprep kit (Thermo) and then sequenced using the BigDye Terminator Cycle Sequencing kit (Applied Biosystems).

An imaging system as previously described (*155*) was used for LAR-GECO variants screening. Specifically, LAR-GECO variants in pBAD/His B vector (Life Technologies) variants were electroporated into *E. coli* strain DH10B (Invitrogen). *E. coli* containing these variants were then cultured on 10 cm LB-agar Petri dishes supplemented with 400 μg/mL ampicillin (Sigma) and 0.02% (wt/vol) L-arabinose (Alfa Aesar) at 37 °C overnight. These Petri dishes were then placed at room temperature for 24 h before screening. During screening, an image was captured for each Petri dish by using excitation filter of 542/27 nm to illuminate *E. coli* colonies expressing LAR-GECO variants and emission filter of 609/57 nm. Colonies showed the highest 0.1% emission intensities in each image were then picked and cultured in 4 mL liquid LB with 100 μg/mL ampicillin and 0.02% (wt/vol) L-arabinose at 37 °C overnight. Proteins were then extracted from the liquid LB culture and subjected to a secondary screen by using a Safire2 fluorescence microplate reader (Tecan).

4.4.2 *In vitro* characterization

For detailed characterization of LAR-GECOs, proteins were expressed and purified as previously described (*162*). Spectral measurements were performed in solutions containing 10 mM EGTA or 10 mM CaNTA, 30 mM MOPS, 100 mM KCl, pH 7.2. For determination of fluorescence quantum yield, mCherry was used as a standard. Procedures for measurement of fluorescence quantum yield, extinction coefficient, p*K*a, K_d for Ca^{2+}, and Ca^{2+}-association kinetics have been described previously (*162*). For Ca^{2+} titration, Ca^{2+}/EDTA , Ca^{2+}/HEDTA, and Ca^{2+}/NTA buffers were prepared by by mixing Ca^{2+}-saturated and Ca^{2+}-free buffers (30 mM MOPS, 100 mM KCl, 10 mM chelating reagent, pH 7.2, either

with or without 10 mM Ca^{2+}) to achieve the buffer Ca^{2+} concentrations from 0 to 1.13mM.

4.4.3 Dual-color ER and cytosolic Ca^{2+} imaging using LAR-GECO1

HeLa cells (40-60% confluent) on collagen-coated 35 mm glass bottom dishes (Mastumami) were transfected with 1 μg of plasmid DNA and 4 μL Lipofectamine 2000 (Life technologies) according to the manufacturer's instructions. After 2 h incubation the media was exchanged to Dulbecco's Modified Eagle Medium (DMEM) with 10% fetal bovine serum (FBS) and the cells were incubated for an additional 24 h at 37 °C in a CO_2 incubator. Immediately prior to imaging, cells were washed twice with Hank's Balanced Salt Solution (HBSS) and then 1 ml of 20 mM HEPES buffered HBSS (HHBSS) was added.

Widefield imaging was performed on an inverted Nikon Eclipse Ti microscope equipped with a 200 W metal halide lamp (PRIOR Lumen), 20× and 40× objectives (Nikon), and a 16-bit QuantEM 512SC electron-multiplying CCD camera (Photometrics). A filter set of 470/40 nm (excitation), 525/50 nm (emission), and 495 nm (dichroic) was used for imaging GCaMP3. Another filter set of 545/30 nm (excitation), 620/60 nm (emission), and 570 nm (dichroic) was used for ER-LAR-GECO1. For time-lapse imaging, HeLa cells were treated with 5 μM (final concentration) histamine.

4.4.4 Imaging LAR-GECO1.2 in mitochondria of neurons

Primary dorsal root ganglion (DRG) neuron cultures were prepared from adult C57BL/6J adult mice (8-12 weeks of age) and transfected with cDNA

plasmids using an Amaxa nucleofection system (Lonza), as previously described (*223*, *224*). Primary culture of hippocampal neurons was prepared from neonatal (P0-P1) C57BL/6J mice and transfected with cDNA using Lipofectamine 2000 (Life Technologies) using the same protocol as previously described (*223*). Transfected with the mito-LAR-GECO1.2 plasmid DRG or hippocampal neurons were loaded with Fura2/AM (2 μM for 30 min) to perform simultaneous monitoring of Ca^{2+} concentration in mitochondria ($[Ca^{2+}]_{mt}$) and cytosol ($[Ca^{2+}]_i$). Cells were then placed in a chamber for flow-through perfusion and mounted onto an inverted IX-71 microscope (Olympus, Japan). Cells were perfused with a standard extracellular HEPES buffered Hank's salt solution composed of 140 mM NaCl, 5 mM KCl, 1.3 mM $CaCl_2$, 0.4 mM $MgSO_4$, 0.5 mM $MgCl_2$, 0.4 mM KH_2PO_4, 0.6 mM $NaHPO_4$, 3 mM $NaHCO_3$, 10 mM glucose, 10 mM HEPES, pH 7.4, with NaOH (310 mOsm/kg with sucrose). Fluorescence was sequentially excited at 340 nm (12 nm bandpass), 380 nm (12 nm bandpass), and 550 nm (12 nm bandpass) using a Polychrome V monochromator (TILL Photonics, Germany) and focused on the cells via a 40x oil-immersion objective (NA=1.35, Olympus). Fluorescence emission was separated from excitation by using a dual fluorophore beamsplitter FF493/574-Di01 (Semrock; Rochester NY) and collected with a dual band emission filter FF01-512/630 (Semrock) using an IMAGO CCD camera (640x480 pixels; TILL Photonics, Germany). A 2x2 binning was used for acquisition (1 pixel ~500 nm). Series of 340 nm, 380 nm, and 550 nm images were acquired every 2 sec. $[Ca^{2+}]$ was calculated by converting the fluorescence ratio ($R=F_{340}/F_{380}$) using the formula $[Ca^{2+}]=K_d\beta(R-R_{min})/(R_{max}-R)$. R_{min}, R_{max}, and β were calculated by application of 10 μM ionomycin in either Ca^{2+}-free buffer (1 mM EGTA) or in HEPES buffered Hank's salt solution (1.3 mM Ca^{2+}). $[Ca^{2+}]_{mt}$ changes were quantified as $\Delta F/F_0=(F-F_0)/F_0*100\%$ where F is the

current fluorescence intensity (λ_{Ex}=550 nm) and F_0 is the fluorescence intensity in the resting cell. $[Ca^{2+}]_i$ data were analyzed using TILLvisION (TILL photonics, Germany) software. To stimulate neurons by depolarization, extracellular KCl concentration was elevated by substituting the equimolar amount of extracellular NaCl with KCl.

4.4.5 Imaging LAR-GECO3 in the ER of HEK-293

HEK-293 cells stably expressing wild type RyR2 were grown to 95% confluence in a 75 cm^2 flask, split with PBS, and plated in 100 mm tissue culture dishes at ~10% confluence 18~20 hours before transfection with ER-LAR-GECO3 cDNA using calcium phosphate precipitation method. After transfection for 24 hours, the growth medium was then changed to an induction medium containing 1 μg/ml tetracycline (Sigma). After induced for ~22 hours, the cells were perfused continuously with KRH buffer (125 mM NaCl, 5 mM KCl, 1.2 mM KH_2PO_4, 6 mM glucose, 1.2 mM $MgCl_2$, 25 mM Hepes, pH 7.4) containing various concentrations of $CaCl_2$ (0, 1, and 2 mM) and tetracaine (1 mM) for estimating the store capacity or caffeine (20 mM) for estimating the minimum store level by depleting the ER Ca^{2+} stores at room temperature (23 °C). For ER-LAR-GECO3 recordings, images were captured using the Nikon A1R confocal system. The cells were excited using the diode laser (561 nm) and fluorescence emission was detected at 570-620 nm. The fluorescent signal was normalized and expressed as the change of fluorescence divided by the resting fluorescence: $(F-F_0)/F_0$.

Chapter 5 Development of a red fluorescent probe for glutamate detection

5.1 Introduction

As one of the most common molecules found in living cells, glutamate is a major player in numerous activities in the cells ranging from regulating metabolism, to protein synthesis, to mediating communication between neurons. As a neurotransmitter, glutamate's concentration can greatly affect the growth of neuron cells and play an important role in learning and memory. Brain diseases such as Parkinson's disease, Alzheimer disease, and epilepsies are highly related to cell damage due to the accumulation of high concentrations of glutamate near neuron cell (*225*). Therefore, understanding the dynamics of glutamate in the nervous system would greatly facilitate efforts to decipher how our brain works and shine light on the mechanism of various brain diseases.

FPs, as a revolutionary tool for cell biology, provides an excellent opportunity to look into various previously unseen static and dynamic processes in living organisms. An elegant example involving an FP based biosensor to study glutamate dynamics in neurons was designed by Okumoto and coworkers (*8*) in 2005. This biosensor was used for measuring glutamate secretion in cultured neurons in real time (*8*). In their design, an *E. coli* derived glutamate binding domain, GltI (*226*), was fused between a CFP-YFP FRET pair. Upon glutamate binding, the two lobes of GltI undergo a conformational change, which changes the distance between the two FPs. As a result, the FRET efficiency changes and provides a spectral readout. This sensor enables us to measure subcellular glutamate concentration in real time with high spatial resolution. In addition, the glutamate-binding pocket was further modified to generate a series of biosensors with different glutamate affinities ranging from 600 nM to 1 mM (*8*). This FP-

based glutamate indicator has opened a new frontier for visualizing the glutamate dynamics in the cells.

One drawback of this FRET-based glutamate biosensor, however, comes from its relatively low sensitivity and signal-to-noise ratio. To improve these properties, Looger and coworkers recently engineered a single FP-based glutamate biosensor called iGluSnFR (*9*). Similar to the GCaMP-type indicators, iGluSnFR was constructed by fusing a cpGFP to the glutamate binding domain GltI, and was shown to exhibit a maximal fluorescence intensity change of 4-fold upon binding to glutamate. In addition, the utility of this sensor was demonstrated by measuring glutamate transients in mouse forelimb motor cortex (*9*). This cpGFP-based glutamate sensor not only exhibits higher sensitivity compared to the previous FRET-based designs, but also shows great potential for multi-color imaging together with red FPs.

Given the well developed plethora of GFP-based probes and indicators for various analytes such as Ca^{2+} (*1*, *2*), H^{+} (*4*) and ATP (*10*, *11*), an RFP-based glutamate indicator would be highly beneficial for multi-color imaging for multi-analyte. Inspired by the X-ray crystal structure of the intensiometric Ca^{2+} indicator R-GECO1 (PDB ID 4I2Y) (*146*) and our previous experience on engineering RFP-based indicators, we reasoned that we could engineer an RFP-based glutamate indicator by properly fusing the glutamate binding domain to the cpRFP from R-GECO1 (*144*). In this Chapter, I will describe our successful efforts to engineer the first single RFP-based glutamate indicator. This glutamate indicator, designated as GltR1, was demonstrated to be functional in HEK-293 cells and dissociated hippocampal neurons.

5.2 Results and discussion

5.2.1 Initial engineering of GltR0.1

To engineer a RFP-based glutamate indicator, we explored the possibility of inserting the cp-RFP from R-GECO1 (*144*) into the glutamate binding domain, GltI (*226*), from iGluSnFR (*9*). We chose position 248 and 496 (Figure 5.1) of cp-RFP for the insertion, reasoning that the same glutamate-dependent conformational change of GltI in iGluSnFR might be sufficient to render Lys270 (Figure 5.1) to interact with the chromophore of the cp-RFP as we observed in the X-ray crystal structure of R-GECO1 (PDB ID 4I2Y) (*146*). To test this hypothesis, we created a library in which the cp-RFP was fused between position 247 and 497 of GltI, with Pro248 and Ala494 of the cp-RFP linker fully randomized. The resulting library was expressed in a pBAD/His B vector (Life Technologies) in *E.coli*. Screening this library lead us to the identification of GltR0.1, a variant with ~50% decrease of fluorescence intensity, or a ~1 fold dynamic range (dynamic range = $(F_{max}-F_{min}) / F_{min}$), upon binding to glutamate (Figure 5.2). GltR0.1 carries mutations Pro248Glu and Ala494Pro in the linkers (Figure 5.1), in addition, we noticed its emission peak shifts from 594 nm to 600 nm upon binding to glutamate, which indicates there is a change of chromophore environment.

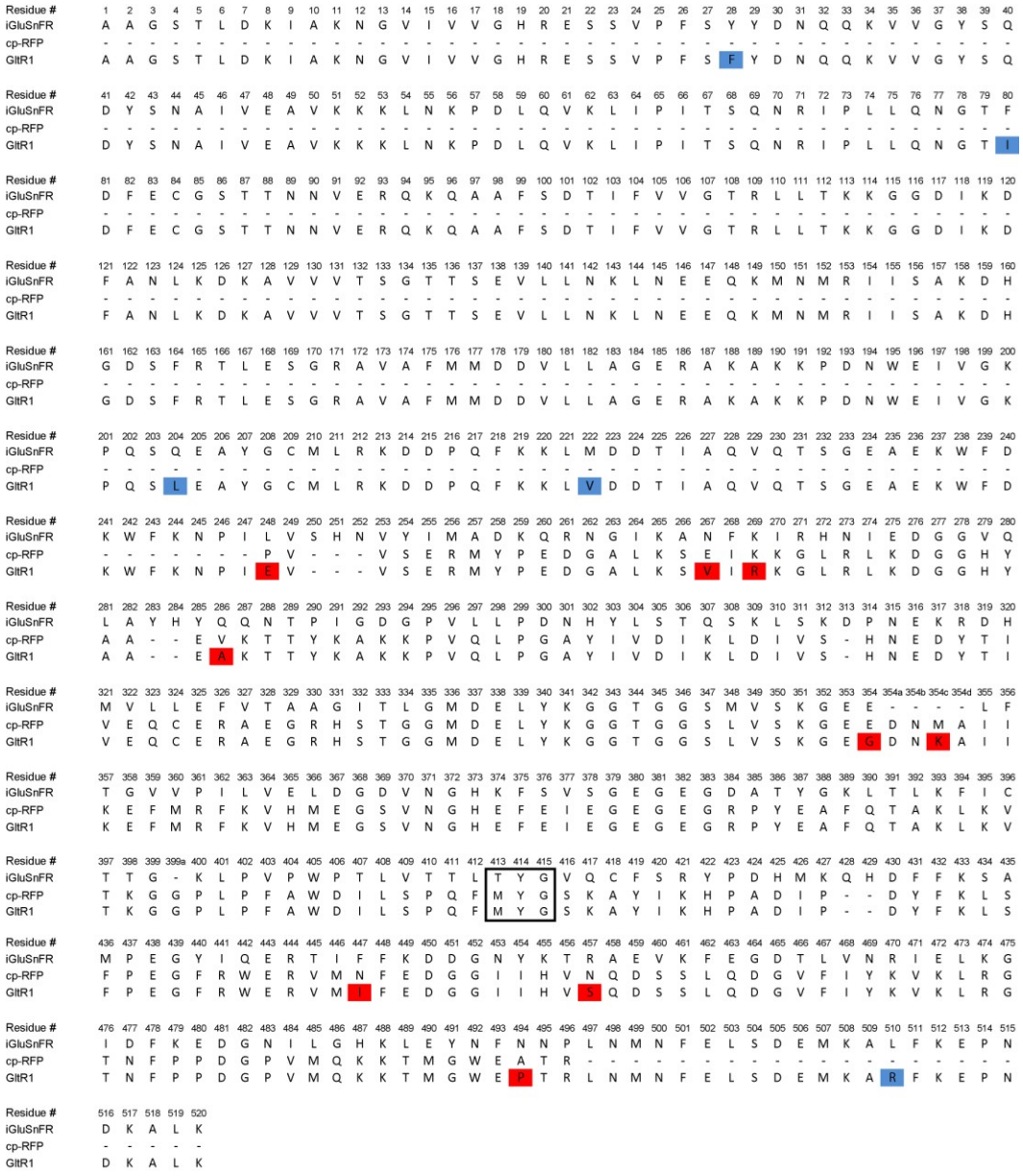

Figure 5.1. Sequence alignment of iGluSnFR, cp-RFP (from R-GECO1) and GltR1.Changes of GltR1 relative to iGluSnFR and cp-RFP (from R-GECO1) are shown as blue and red boxes, respectively.

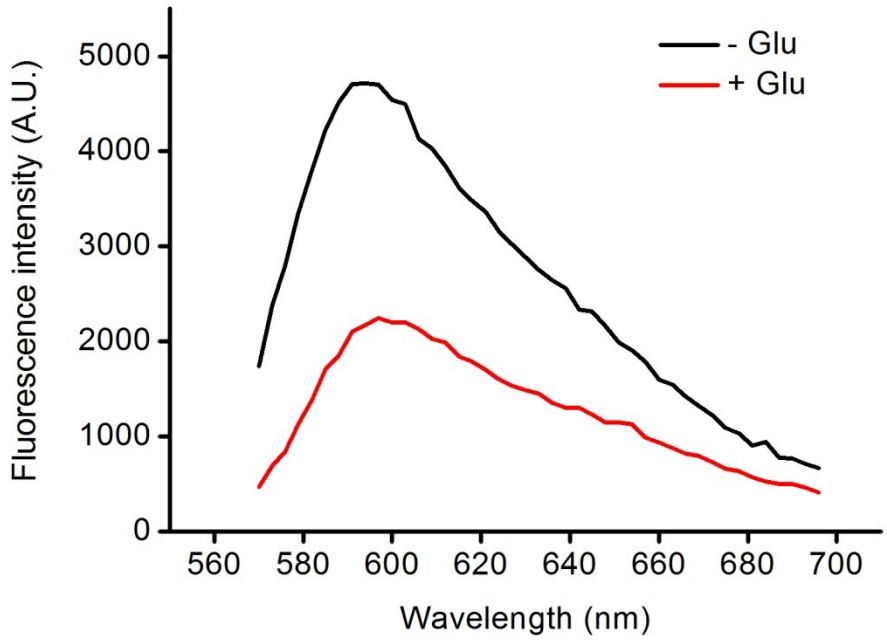

Figure 5.2. Emission spectra of GltR0.1 from bacterial protein extract with or without 2 mM glutamate. Glutamate-free state is shown as black line, and glutamate-bound state is shown as red line.

5.2.2 Directed evolution of GltR0.1 for improved function

Even though exhibiting a 1-fold dynamic range, GltR0.1's fluorescence intensity is relatively low when expressed in *E. coli*. To improve GltR0.1's fluorescence brightness and dynamic range, undergraduate researcher, Hang Zhou, and I performed 7 rounds of directed evolution and screened for variants with high dynamic range and fluorescence intensity in *E. coli*. During the first 5 rounds of directed evolution, we aimed to rescue the fluorescence brightness of GltR0.1. Specifically, we performed random mutagenesis on GltR0.1 in the pBAD/His B vector (Life Technologies). The resulting libraries were screened for

high red fluorescence intensity colonies (with excitation filter 560/40 nm and emission filter 630/60 nm), potential variants were then cultured and their extracted proteins were subjected to test for response to glutamate. The best variants from round 5 of directed evolution exhibited brighter fluorescence and fast protein folding in *E. coli* as well as a ~2-fold dynamic range.

Since the endogenous glutamate concentration in *E. coli* might saturate part or most of the indicators (*227*), the above screening strategy is mainly selecting glutamate indicators in their low fluorescence state (glutamate-bound state). Given our previous experience on engineering intensiometric indicators, we reasoned that screening the GltR variants in the high fluorescence state (glutamate-free state) will be more effective in terms of improving their fluorescence brightness and dynamic range. To achieve this, we performed directed evolution on the best variants from round 5 and expressed the libraries using a periplasmic expression vector (*144*). The resulting *E. coli* libraries were grown on a glutamate-free M9 medium with a rationale that the GltR variants expressed in the periplasmic space in *E. coli* will be rendered in the high fluorescence state (glutamate-free state). These libraries were then screened for high red fluorescence intensity colonies and the selected variants were tested for their glutamate response. Two more rounds of directed evolution using this scheme lead us to the identification of our best variant, designated as GltR1, which exhibits a 3-fold glutamate-dependent dynamic range (Figure 5.3). GltR1 has 12 mutations compared with GltR0.1 (Table 5.1). Among there 12 mutations, 5 of them are in the glutamate binding domain, GltI, and the rest are in the cp-RFP.

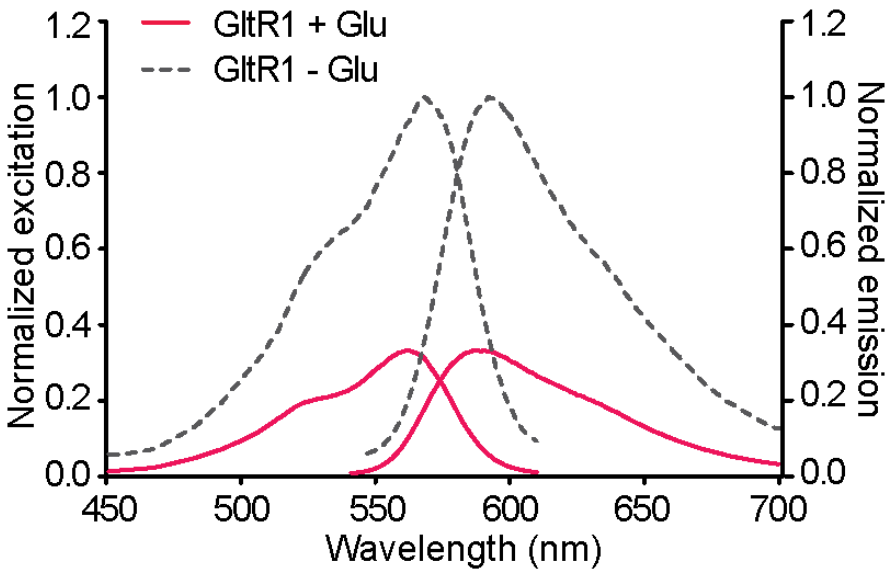

Figure 5.3. Normalized excitation and emission spectra of GltR1 with or without 2 mM glutamate. Glutamate-free state is shown as dotted grey line, and glutamate-bound state is shown as solid pink line.

Table 5.1 Substitutions for GltR1 described in this work. Residues are numbered as described in **Figure 5.1**.

Protein	Substitutions relative to GltI (blue) or cp-RFP (red)
GltR1	Y28F F80I Q204L M222V P248E E267V K269R V286A E354G M354cK N447I N457S A494P L510R

5.2.3 *In vitro* characterization of GltR1

Next, Hang Zhou and I performed systematic *in vitro* characterization on GltR1. GltR1 has an excitation and emission peak at 562 nm and 588 nm, respectively, in the glutamate-free state. Upon binding to glutamate, both peaks shift to 564 nm and 592 nm, respectively (Table 5.2). Interestingly, GltR1 has very similar quantum yields in both the glutamate-free and -bound states, which is 0.20 and

0.21, respectively (Table 5.2), which suggests the change of fluorescence intensity upon binding to glutamate mainly comes from the change of extinction coefficients. Furthermore, GltR1 exhibits the largest change of fluorescent from pH values from 5.5 to 8 (Figure 5.4), which is suitable for most physiological conditions. In addition, to determine the specificity of GltR1, we titrated purified GltR1 proteins against different concentrations of glutamate, aspartate, glutamine and asparagines. The results showed that GltR1 has a K_d of 11 μM for glutamate, 38 μM for aspartate, > 1 mM for glutamine or asparagine (Figure 5.5) at pH 7.4.

Table 5.2. Properties of GltR1.

Protein	Glu	λ_{abs} (nm) (ε) ($mM^{-1} \cdot cm^{-1}$)	λ_{em} (Φ)	Brightness[1] ($mM^{-1} \cdot cm^{-1}$)	Intensity change ± Ca^{2+}	K_d for Glu (μM), and (Hill coefficient)
GltR1	-	562 (35)	588 (0.20)	7.0	3×	11.0 (1)
	+	564 (11)	592 (0.21)	2.3		

[1]Brightness is defined as the product of ε and Φ.

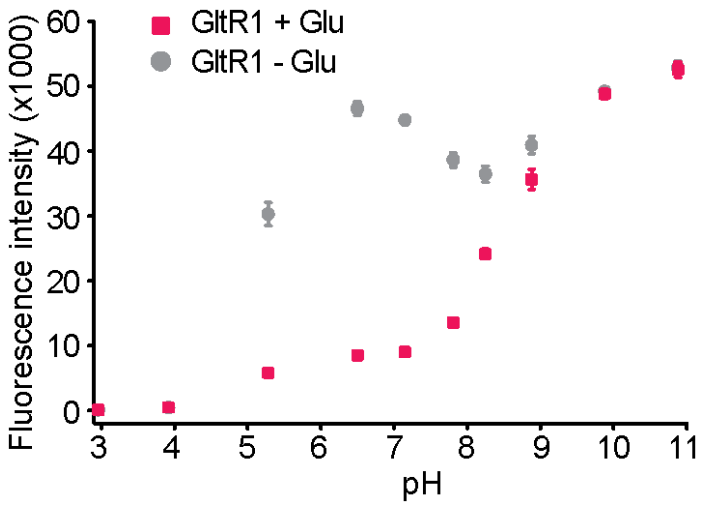

Figure 5.4. Fluorescence intensities of GltR1 with (pink) and without (grey) glutamate as a function of pH.

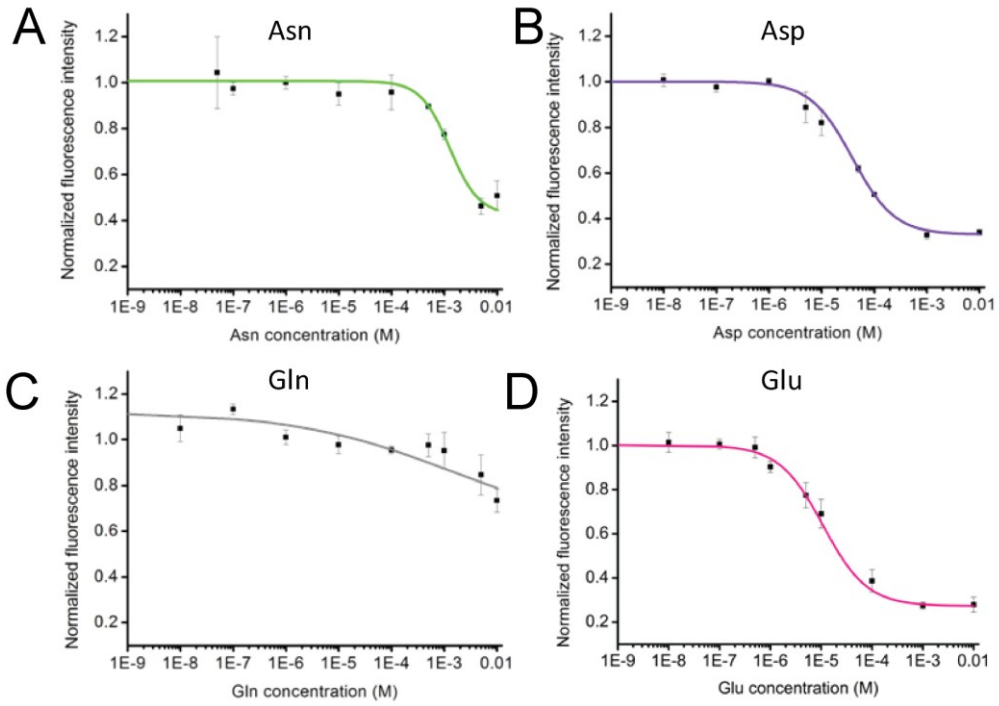

Figure 5.5. Normalized fluorescence intensity of GltR1 as a function of different concentrations of analytes: (A) asparagine (Asn), (B) aspartate (Asp), (C) glutamine (Gln) and (D) glutamate (Glu).

5.2.4 Live cells performance of GltR1

To explore its utility, we expressed GltR1 on the surface of human embryonic kidney HEK-293 cells and tested for its response to glutamate under pH 7.4. When expressed on the surface of HEK-293 cells, GltR1 showed correct membrane localization (Figure 5.6). Upon addition of 2 mM glutamate, GltR1 displayed a 30 % decrease of fluorescence intensity (Figure 5.6), due to the binding to glutamate on the surface of the cell membrane. Next, we expressed GltR1 on the surface of dissociated rat hippocampal neurons to monitor the glutamate dynamics. Indeed, we observed ~10 % and ~25% of fluorescence intensity decrease in the cell body and the neuron processes, respectively, during spontaneous activity (Figure 5.7).

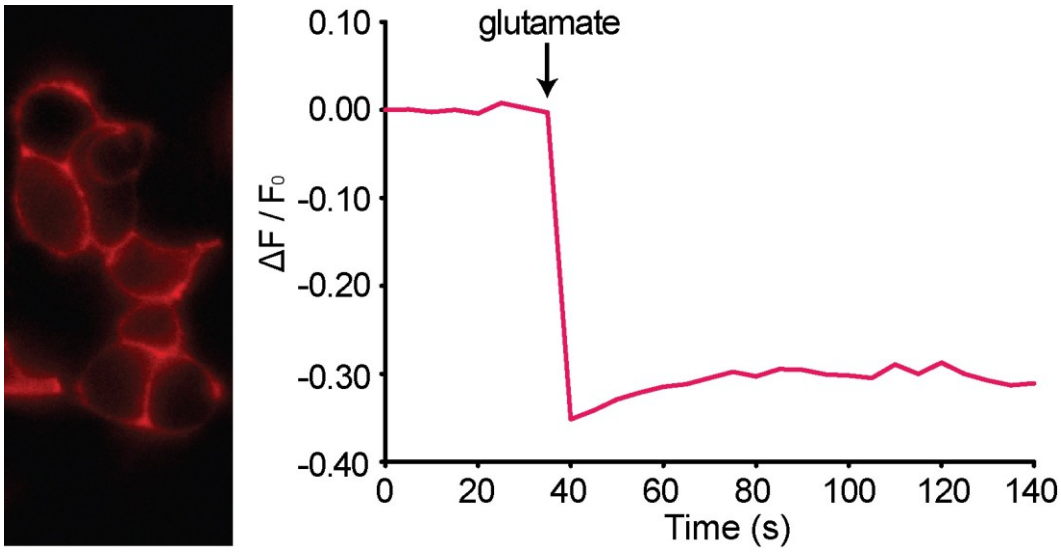

Figure 5.6. Performance of GltR1 expressed on the surface of HEK-293 cells. Left panel: HEK-293 cells expressing GltR1 on the surface of their plasma

membrane. Right panel: change of fluorescence intensity of GltR1 upon addition of 2mM glutamate.

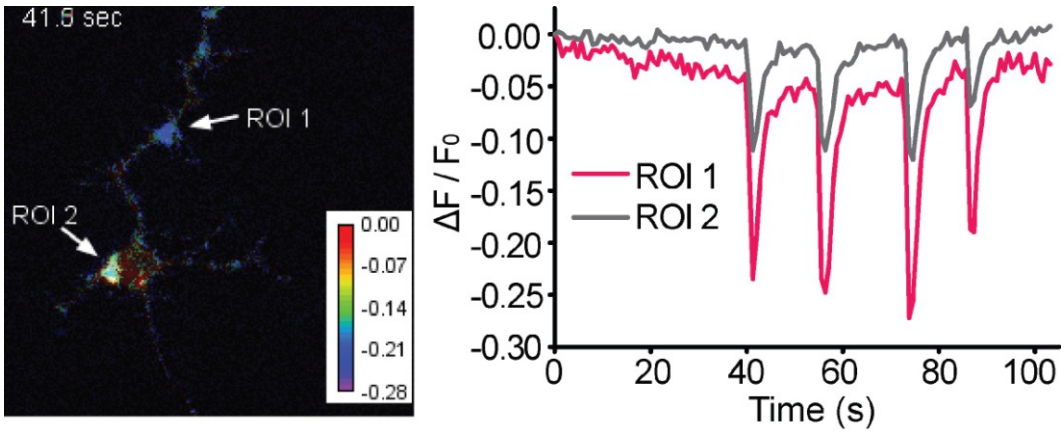

Figure 5.7. Detection of spontaneous glutamate dynamics on the surface of dissociated rat hippocampal neurons. Left panel: a dissociated rat hippocampal neuron expressing GltR1 on its surface. Two region-of-interest (ROI) are labeled. Right panel: change of fluorescence intensity of GltR1 as a function of time. The two traces are the two ROIs in the left panel.

5.3 Conclusion

In summary, inspired by the X-ray crystal structure of the intensiometric Ca^{2+} indicator R-GECO1, we have successfully engineered the first single RFP-based glutamate indicator, GltR1, by combining rational design and directed evolution. GltR1 exhibits a reasonable dynamics range of 3-fold upon binding to glutamate. Furthermore, GltR1 enables detection of glutamate changes on the surface of HEK-293 cells, and is capable of sensing the glutamate dynamics during spontaneous activities of dissociated hippocampal neurons. We expect GltR1

would open new doors for performing multi-color and multi-analyte imaging when combined with the well-developed plethora of GFP-based probes and indicators.

5.4 Materials and methods

5.4.1 Engineering of GltR1

For assembling GltR0.1, the cp-RFP from R-GECO1 in pTorPE (*144*) and the glutamate binding domain GltI from iGluSnFR (Addgene plasmid 41732) were used as template. Overlap PCR was performed with complete randomization at residue 248 and 496 (Figure 5.1) of the cp-RFP. To screen for functional variants from this initial library, An imaging system as previously described (*155*) was used. Specifically, GltR variants in the pBAD/His B vector (Life Technologies) were electroporated into the *E. coli* strain DH10B (Invitrogen). *E. coli* containing these variants were then cultured on 10 cm LB-agar Petri dishes supplemented with 400 μg/mL ampicillin (Sigma) and 0.02% (wt/vol) L-arabinose (Alfa Aesar) at 37 °C overnight. During screening, an excitation filter of 542/27 nm to illuminate *E. coli* colonies expressing GltR variants, an image was captured for each Petri dish by using an emission filter of 609/57 nm. Colonies that showed the highest 0.1% emission intensities in each image were then picked and cultured in 4 mL liquid LB with 100 μg/mL ampicillin and 0.02% (wt/vol) L-arabinose at 37 °C overnight. Proteins were then extracted from the liquid LB culture and subjected to a secondary test by using a Safire2 fluorescence microplate reader (Tecan).

Once we identified GltR0.1, it was objected to directed evolution using a pBAD/His B vector (Life Technologies) for the first 5 rounds to improve its fluorescence intensity and folding efficiency. Random mutagenesis on GltR0.1 was carried out by error-prone PCR. The screening procedure in these 5 rounds

of directed evolution was the same as mentioned above. After this, we performed 2 more rounds of directed evolution using the pTorPE vector (*144*). Specifically, GltR variants produced by error-prone PCR were expressed in *E. coli* using the pTorPE vector (*144*). Next, *E. coli* containing these variants were then cultured on 10 cm M9-agar (containing 2 mM $MgSO_4$, 0.1 mM $CaCl_2$ and 0.4% glycerol) Petri dishes supplemented with 400 μg/mL ampicillin (Sigma) and 0.0016% (wt/vol) L-arabinose (Alfa Aesar) at 37 °C overnight. *E. coli* colonies from these Petri dishes were incubated under room temperature for 24 h before screening. The screening procedure was the same as mentioned above.

5.4.2 *In vitro* characterization of GltR1

To purify GltR1 proteins for characterization, DH10B *E. coli* expressing GltR1 in pTorPE were picked and cultured in 4 mL liquid LB medium (100 μg/mL ampicillin) at 37 °C overnight. This 4 mL culture was then inoculated into 500 mL liquid LB medium (100 μg/mL ampicillin, 0.0016% L-arabinose) and cultured at 22 °C for 48 h. After culture, bacteria were harvested by centrifugation and resuspended in 30 mM Tris-HCl buffer (pH 7.3). GltR1 proteins were extracted from bacteria by French press and centrifugation, followed by Ni-NTA affinity chromatography (Agarose Bead Technologies) for purification. Purified GltR1 proteins were subjected to buffer exchange to 10 mM MOPS, 100 mM KCl (pH 7.2) by centrifugal concentrators (GE Healthcare Life Sciences).

To determine the absorbance and fluorescence spectra of GltR1, we used a DU-800 UV-visible spectrophotometer (Beckman) and a QuantaMaster spectrofluorometer (Photon Technology International). To measure its quantum yield (Φ), GltR1 protein solutions were first diluted to have absorbance values at

the excitation wavelength ranging from 0.01 to 0.05 using 10 mM MOPS, 100 mM KCl (pH 7.2) buffer. Purified mCherry protein was used as a standard. Next, fluorescence spectra of GltR1 and mCherry were measured, and the total fluorescence intensities were obtained by integration. These integrated fluorescence intensities were plotted against their absorbances, and the slope (S) of each line was determined. Quantum yield of GltR1 was then determined by using the following equation: $\Phi_{protein} = \Phi_{standard} \times (S_{protein}/S_{standard})$. To measure its extinction coefficient (ε), purified proteins of GltR1 was first subjected to alkaline denaturation, and its concentration was determined by the following equation: c = A/(ε × b), where A is absorbance at 450 nm, ε = 44,000 $M^{-1}cm^{-1}$, b = 1 cm. Then, its extinction coefficient was calculated by ε = A/(b × c), where A is peak absorbance before denaturation, b = 1 cm, c is the protein concentration. To determine the pH sensitivity of GltR1, a series of buffers (containing 30 mM trisodium citrate and 30 mM borax) with pH ranging from 3 to 11 were prepared. Fluorescence intensities of GltR1 were measured in this set of pH buffers with and without the present of glutamate, respectively. To measure the affinity and specificity of GltR1, a series of glutamate, glutamine, aspartate and asparigine buffers with concentrations ranging from 10 nM to 10 mM in 10 mM MOPS, 100 mM KCl (pH 7.2) were prepared respectively. GltR1 proteins were added into this series of buffers, and their fluorescence intensities were measured. These fluorescence intensities were then plotted against different concentrations of different analytes and fitted by Hill equation.

5.4.3 Live cell imaging of GltR1 in HEK-293 cells and dissociated hippocampal neurons

For GltR1 plasmid used for imaging, the gene of GltR1 was cloned into the pDisplay vector from iGluSnFR (Addgene plasmid 41732) by PCR as previously described (*162*) to obtain pDisplay-GltR1. Widefield imaging was performed on an inverted Nikon Eclipse Ti microscope equipped with a 200 W metal halide lamp (PRIOR Lumen), 20× and 40× objectives (Nikon), and a 16-bit QuantEM 512SC electron-multiplying CCD camera (Photometrics). A filter set of 545/30 nm (excitation), 620/60 nm (emission), and 570 nm (dichroic) was used for GltR1.

To test the function of GltR1 on the surface of plasma membrane, HEK-293 cells were cultured on collagen-coated 35 mm glass bottom dishes (Mastumami) until they reached 40-60% confluency. To transfection HEK-293 cells, 1 μg of plasmid DNA containing pDisplay-GltR1 and 3 μL of Lipofectamine 2000 (Life technologies) were mixed and added into the collagen-coated 35 mm glass bottom dishes (Mastumami). After 2 h incubation, the medium was exchanged to Dulbecco's modified Eagle's medium (DMEM) (supplemented with 10% fetal bovine serum (FBS) (Sigma), 2 mM GlutaMax (Invitrogen) and penicillin-streptomycin) and the cells were incubated for 48 h at 37 °C in a CO_2 incubator. Prior to imaging, culture medium was changed to HEPES (25 mM) buffered Hanks' Balanced Salt Solution (HBSS). For time-lapse imaging, HEK-293 cells were treated with 2 mM (final concentration) of glutamate.

To detect spontaneous activity of dissociated rat hippocampal neurons, dissociated E18 Sprague Dawley Hippocampal Cells in Hibernate® EB Complete Media were purchased from BrainBits LLC. The cells were grown on (In Vitro Scientific) 35 mm glass bottom dish containing NbActiv4 (BrainBits LLC) supplemented with 2% FBS, penicillin-G potassium salt (50 units/mL), and streptomycin sulfate (50 μg/mL). Half of the culture media is replaced every 4-5

days. Neuronal cells were transfected on day 7 with plasmids of pDisplay-GltR1 using Lipofectamine 2000 as described above.

Chapter 6 Conclusions and future directions

6.1 Summary of the thesis

Small ions and molecules play an indispensable role as signals in most biological activities. The ability to visualize the dynamics of these signals can allow one to decipher the 'language' communicated between or within cells in various biological processes. Among these signaling molecules, Ca^{2+} and glutamate are two of the most important ones. As a result, there has been an increasingly growing demand for Ca^{2+} and glutamate indicators. The focus of this thesis was to develop various FP-based Ca^{2+} and glutamate indicators with high sensitivity and useful spectral properties as versatile tools for interrogating cell signaling in cell biology.

As a ubiquitous second messenger, Ca^{2+} has essential physiological roles in a variety of cellular processes including muscle contraction, propagation of action potentials, fertilization, and development (*199*). The development and subsequent application of genetically encoded Ca^{2+} indicators based on fluorescent proteins has revolutionized the study of intracellular Ca^{2+} dynamics (*1*–*3*). However, despite many significant developments during the last decade, genetically encoded Ca^{2+} indicators with more hues are still in great demand. In Chapter 2 we report our successful efforts to develop a series of genetically encoded Ca^{2+} indicators with colors ranging from orange, improved red and far red, featuring O-GECO with a Ca^{2+} dependent intensiometric signal change of 14600%. Furthermore, we discovered and characterized a photoactivation phenomenon in these orange and red fluorescent Ca^{2+} indicators in the course of this work. In close collaboration with Dr. Takeharu Nagai's group and Dr. Wen-hong Li's group, we demonstrated, in both a beta cell line and slice culture of developing mouse neocortex, that the potential artifacts from this photoactivation

phenomenon can be avoided by using an appropriately low intensity of blue light for ChR2 activation.

In the past two decades, many advances in neuroscience have been propelled forward by the use of two-photon excitation fluorescence microscopy. As one of the most powerful imaging techniques for probing neuronal dynamics, genetically encoded Ca^{2+} indicators optimized for two-photon excitation microscopy applications have great potential (*142*). After our efforts in developing and optimizing a series of orange and red genetically encoded Ca^{2+} indicators, we noticed a drawback of these indicators is that their peak two-photon excitation cross-sections are outside of the near-infrared optical window. Specifically, their peak excitation is often at 1000 nm or more, making them sub-optimal in many applications and imaging systems. To address this shortcoming, in Chapter 3, we described our successful efforts in developing a long Stokes shift RFP-based Ca^{2+} indicator, REX-GECO1, with optimal 2-photon excitation at less than 1000 nm. REX-GECO1 fluoresces at 585 nm when excited at 480 nm or 910 nm by a 1- or 2-photon process, respectively. We demonstrate that REX-GECO1 can be used as either a ratiometric or intensiometric Ca^{2+} indicator in organotypic hippocampal slice cultures (1- and 2-photon) and the visual system of albino tadpoles (2-photon). Furthermore, we demonstrate single excitation wavelength two-color Ca^{2+} and glutamate imaging in organotypic cultures.

As a key intermediary in a variety of signaling pathways, Ca^{2+} undergoes dynamic changes in its cytoplasmic concentration due to release from stores within the endoplasmic reticulum (ER) and influx from the extracellular environment. As we demonstrate, single FP-based Ca^{2+} indicators are powerful tools for imaging changes in the concentration of Ca^{2+} associated with

intracellular signaling pathways. Most GCaMP-type indicators have K_ds for Ca^{2+} in the high nanomolar to low micromolar range and are therefore optimal for measuring cytoplasmic Ca^{2+} concentrations, but poorly suited for use in mitochondria and ER where Ca^{2+} concentrations can reach hundreds of micromolar. To bridge this gap, in Chapter 4, we report a series of GCaMP-type low-affinity red fluorescent genetically encoded Ca^{2+} indicators for optical imaging, engineered to have K_d values ranging from 12 μM to more than 540 μM. We demonstrate that these indicators can be used to image mitochondrial and ER Ca^{2+} dynamics in several cell types. In addition, we perform two-color imaging of intracellular Ca^{2+} dynamics in cells expressing both cytoplasmic GCaMP and ER-targeted LAR-GECO. The development of these low-affinity intensiometric red fluorescent Ca^{2+} indicators enables a range of new opportunities for monitoring of ER and mitochondrial Ca^{2+} in combination with a GFP-based marker or reporter.

Besides Ca^{2+}, glutamate is another common, yet essential molecule found in all living organisms. It plays an indispensable role in various cell activities from regulating metabolism, to protein synthesis, to mediating communication between neurons. Accordingly, FP-based indicators for visualizing glutamate in living cells are in great need. Given the well-developed plethora of GFP-based probes and indicators for various analytes, an RFP-based glutamate indicator would be highly beneficial for multi-color imaging for multi-analyte. In Chapter 5, we describe our endeavour in developing the first RFP-based glutamate indicator, GltR1. We demonstrate GltR1 can detect glutamate changes on the surface of cultured human cells, as well as the glutamate dynamics during spontaneous activities of dissociated rat hippocampal neurons.

6.2 Future directions

6.2.1 Optimization of the GECOs

Despite the tremendous expansion of the color palette, all of the GECOs described in this thesis still have some potential problems that might hamper their applications in neuroscience. One major problem of the orange and red GECOs is their tendency to aggregate when expressed in neural cells. This problem seems to originate with mRFP1 (*55*), where mRFP1 and its derivatives all exhibit different extent of aggregation in neural cells for yet unknown reasons. Since all of our orange and red GECOs employed mRFP1's derivatives as the transducer, the same aggregation problem is preserved in all of our orange and red GECOs. The tendency to aggregate in neural cells complicates the interpretation of the real fluorescence signal from these indicators, and also severely limits their applications in transgenic animals, since the aggregated proteins are likely to cause toxic effects to the host cells. We speculate that the cause of this problem is due to the stability of the FP domain in these indicators. The FP domain slows down the degradation rate of these indicators, as a result, causing their accumulation in cells. Further investigations to solve this issue would greatly enhance the versatility of the GECOs in neuroscience research. Another problem of the GECOs described in this thesis is the photoactivation problem. Although we have discussed in Chapter 2, this problem could be avoided by using a lower laser power for photoactivation, however, it would be ideal to completely eliminate this problem.

Another aspect of improving the GECO series will be to engineer a bright far-red GECO. Despite in Chapter 3, we demonstrate using 2-photon excitation to achieve NIR excitation of REX-GECO1, however, its 2-photon cross section is

still limited. Further efforts to enhance the 2-photon cross section of REX-GECO1 will definitely be beneficial. An alternative will be to utilize a far-red FP as the transducer and engineer a new far red Ca^{2+} indicator. As the recent developments on NIR FPs, variants, such as mCardinal (*169*), IFP2.0 (*228*), iFPs (*229*) are all promising potential candidates.

6.2.2 Optimization of GltR1

In Chapter 5, we demonstrate the utility of the first red glutamate indicator, GltR1, in HEK-293 cells and dissociated rat hippocampal neurons. However, we also notice that there is substantial room for improving this indicator's fluorescence brightness. Further optimization to enhance the brightness of GltR1 will be beneficial for its applications in neuroscience research. Furthermore, since GltR1 utilized the cpRFP from R-GECO1 as the transducer, it is possible to borrow REX-GECO1's key mutations to GltR1 to engineer a red ratiometric glutamate indicator that will be more suitable for quantitative experiments. One possible way to carry out this optimization is to employ directed evolution by using dissociated neurons or even brain slices for screening. Since all of the indicators described in this thesis were engineered and optimized using *E. coli*, their protein folding efficiency, fluorescence brightness and even protein trafficking are optimized in the context of *E. coli*, but not in the actual host cells, in most cases neural cells, during their applications.

References

1. T. Nagai, A. Sawano, E. S. Park, A. Miyawaki, Circularly permuted green fluorescent proteins engineered to sense Ca^{2+}. *Proc. Natl. Acad. Sci. U.S.A.* **98**, 3197–3202 (2001).

2. J. Nakai, M. Ohkura, K. Imoto, A high signal-to-noise Ca^{2+} probe composed of a single green fluorescent protein. *Nat. Biotechnol.* **19**, 137–141 (2001).

3. A. Miyawaki *et al.*, Fluorescent indicators for Ca^{2+} based on green fluorescent proteins and calmodulin. *Nature*. **388**, 882–887 (1997).

4. G. Miesenbock, D. A. De Angelis, J. E. Rothman, Visualizing secretion and synaptic transmission with pH-sensitive green fluorescent proteins. *Nature*. **394**, 192–195 (1998).

5. S. Jayaraman, P. Haggie, R. M. Wachter, S. J. Remington, A. S. Verkman, Mechanism and cellular applications of a green fluorescent protein-based halide sensor. *J. Biol. Chem.* **275**, 6047–6050 (2000).

6. L. J. V Galietta, P. M. Haggie, A. S. Verkman, Green fluorescent protein-based halide indicators with improved chloride and iodide affinities. *FEBS Lett.* **499**, 220–224 (2001).

7. T. Kuner, G. J. Augustine, A genetically encoded ratiometric indicator for chloride. *Neuron*. **27**, 447–459 (2014).

8. S. Okumoto *et al.*, Detection of glutamate release from neurons by genetically encoded surface-displayed FRET nanosensors. *Proc. Natl. Acad. Sci. U.S.A.* **102**, 8740–8745 (2005).

9. J. S. Marvin *et al.*, An optimized fluorescent probe for visualizing glutamate neurotransmission. *Nat. Methods*. **10**, 162–70 (2013).

10. J. Berg, Y. P. Hung, G. Yellen, A genetically encoded fluorescent reporter of ATP:ADP ratio. *Nat. Methods*. **6**, 161–166 (2009).

11. M. Tantama, J. R. Martínez-François, R. Mongeon, G. Yellen, Imaging energy status in live cells with a fluorescent biosensor of the intracellular ATP-to-ADP ratio. *Nat. Commun.* **4**, 2550 (2013).

12. O. Shimomura, F. H. Johnson, Y. Saiga, Extraction, purification and properties of Aequorin, a bioluminescent protein from the luminous hydromedusan, Aequorea. *J. Cell. Comp. Physiol.* **59**, 223–239 (1962).

13. D. C. Prasher, V. K. Eckenrode, W. W. Ward, F. G. Prendergast, M. J. Cormier, Primary structure of the Aequorea victoria green-fluorescent protein. *Gene*. **111**, 229–233 (1992).

14. M. Chalfie, Y. Tu, G. Euskirchen, W. W. Ward, D. C. Prasher, Green fluorescent protein as a marker for gene expression. *Science*. **263**, 802–805 (1994).

15. M. V Matz *et al.*, Fluorescent proteins from nonbioluminescent Anthozoa species. *Nat. Biotechnol.* **17**, 969–973 (1999).

16. N. C. Shaner *et al.*, Improved monomeric red, orange and yellow fluorescent proteins derived from Discosoma sp. red fluorescent protein. *Nat. Biotechnol.* **22**, 1567–1572 (2004).

17. H. Masuda, Y. Takenaka, A. Yamaguchi, S. Nishikawa, H. Mizuno, A novel yellowish-green fluorescent protein from the marine copepod, Chiridius poppei, and its use as a reporter protein in HeLa cells. *Gene*. **372**, 18–25 (2006).

18. D. D. Deheyn *et al.*, Endogenous green fluorescent protein (GFP) in Amphioxus. *Biol. Bull.* **213**, 95–100 (2007).

19. D. Baumann *et al.*, A family of GFP-like proteins with different spectral properties in lancelet Branchiostoma floridae. *Biol. Direct*. **3**, 28 (2008).

20. D. A. Shagin *et al.*, GFP-like proteins as ubiquitous metazoan superfamily: evolution of functional features and structural complexity. *Mol. Biol. Evol.* **21**, 841–850 (2004).

21. C. W. Cody, D. C. Prasher, W. M. Westler, F. G. Prendergast, W. W. Ward, Chemical structure of the hexapeptide chromophore of the Aequorea green-fluorescent protein. *Biochemistry*. **32**, 1212–1218 (1993).

22. O. Shimomura, Structure of the chromophore of Aequorea green fluorescent protein. *FEBS Lett.* **104**, 220–222 (1979).

23. R. Heim, D. C. Prasher, R. Y. Tsien, Wavelength mutations and posttranslational autoxidation of green fluorescent protein. *Proc. Natl. Acad. Sci. U.S.A.* **91**, 12501–12504 (1994).

24. S. Delagrave, R. E. Hawtin, C. M. Silva, M. M. Yang, D. C. Youvan, Red-shifted excitation mutants of the green fluorescent protein. *Nat. Biotechnol.* **13**, 151–154 (1995).

25. R. Y. Tsien, The green fluorescent protein. *Annu. Rev. Biochem.* **67**, 509–544 (1998).

26. F. Yang, L. G. Moss, G. N. Phillips, The molecular structure of green fluorescent protein. *Nat. Biotechnol.* **14**, 1246–1251 (1996).

27. M. Ormö *et al.*, Crystal structure of the Aequorea victoria green fluorescent protein. *Science*. **273**, 1392–1395 (1996).

28. M. A. Wall, M. Socolich, R. Ranganathan, The structural basis for red fluorescence in the tetrameric GFP homolog DsRed. *Nat. Struct. Mol. Biol.* **7**, 1133–1138 (2000).

29. B. R. Branchini, A. R. Nemser, M. Zimmer, A computational analysis of the unique protein-induced tight turn that results in posttranslational chromophore formation in green fluorescent protein. *J. Am. Chem. Soc.* **120**, 1–6 (1998).

30. D. P. Barondeau, C. D. Putnam, C. J. Kassmann, J. A. Tainer, E. D. Getzoff, Mechanism and energetics of green fluorescent protein chromophore synthesis revealed by trapped intermediate structures. *Proc. Natl. Acad. Sci. U.S.A.* **100**, 12111–12116 (2003).

31. A. B. Cubitt *et al.*, Understanding, improving and using green fluorescent proteins. *Trends Biochem. Sci.* **20**, 448–455 (1995).

32. D. P. Barondeau, J. A. Tainer, E. D. Getzoff, Structural evidence for an enolate intermediate in GFP fluorophore biosynthesis. *J. Am. Chem. Soc.* **128**, 3166–3168 (2006).

33. L. Zhang, H. N. Patel, J. W. Lappe, R. M. Wachter, Reaction progress of chromophore biogenesis in green fluorescent protein. *J. Am. Chem. Soc.* **128**, 4766–4772 (2006).

34. M. A. Rosenow, H. A. Huffman, M. E. Phail, R. M. Wachter, The crystal structure of the Y66L variant of green fluorescent protein supports a cyclization−oxidation−dehydration mechanism for chromophore maturation. *Biochemistry*. **43**, 4464–4472 (2004).

35. M. A. Rosenow, H. N. Patel, R. M. Wachter, Oxidative chemistry in the GFP active site leads to covalent cross-linking of a modified leucine side chain with a histidine imidazole: Implications for the mechanism of chromophore formation. *Biochemistry*. **44**, 8303–8311 (2005).

36. L. J. Pouwels, L. Zhang, N. H. Chan, P. C. Dorrestein, R. M. Wachter, Kinetic isotope effect studies on the de novo rate of chromophore formation in fast- and slow-maturing GFP variants. *Biochemistry*. **47**, 10111–10122 (2008).

37. R. L. Strack, D. E. Strongin, L. Mets, B. S. Glick, R. J. Keenan, Chromophore formation in DsRed occurs by a branched pathway. *J. Am. Chem. Soc.* **132**, 8496–8505 (2010).

38. D. P. Barondeau, C. J. Kassmann, J. A. Tainer, E. D. Getzoff, Understanding GFP posttranslational chemistry: structures of designed variants that achieve backbone fragmentation, hydrolysis, and decarboxylation. *J. Am. Chem. Soc.* **128**, 4685–4693 (2006).

39. G. S. Baird, D. A. Zacharias, R. Y. Tsien, Biochemistry, mutagenesis, and oligomerization of DsRed, a red fluorescent protein from coral. *Proc. Natl. Acad. Sci. U.S.A.* **97**, 11984–11989 (2000).

40. A. Terskikh *et al.*, "Fluorescent timer": Protein that changes color with time. *Science*. **290**, 1585–1588 (2000).

41. L. A. Gross, G. S. Baird, R. C. Hoffman, K. K. Baldridge, R. Y. Tsien, The structure of the chromophore within DsRed, a red fluorescent protein from coral. *Proc. Natl. Acad. Sci. U.S.A.* **97**, 11990–11995 (2000).

42. M. F. Garcia-Parajo, M. Koopman, E. M. H. P. van Dijk, V. Subramaniam, N. F. van Hulst, The nature of fluorescence emission in the red fluorescent protein DsRed, revealed by single-molecule detection. *Proc. Natl. Acad. Sci. U.S.A.* **98**, 14392–14397 (2001).

43. V. V Verkhusha, D. M. Chudakov, N. G. Gurskaya, S. Lukyanov, K. A. Lukyanov, Common pathway for the red chromophore formation in fluorescent proteins and chromoproteins. *Chem. Biol.* **11**, 845–854 (2004).

44. D. M. Chudakov, M. V Matz, S. Lukyanov, K. A. Lukyanov, Fluorescent proteins and their applications in imaging living cells and tissues. *Physiol. Rev.* **90**, 1103–1163 (2010).

45. M. Prescott *et al.*, The 2.2 Å crystal structure of a pocilloporin pigment reveals a nonplanar chromophore conformation. *Structure*. **11**, 275–284 (2003).

46. J. Petersen *et al.*, The 2.0-Å crystal structure of eqFP611, a far red fluorescent protein from the sea Anemone Entacmaea quadricolor. *J. Biol. Chem.* **278**, 44626–44631 (2003).

47. J. N. Henderson, H. Ai, R. E. Campbell, S. J. Remington, Structural basis for reversible photobleaching of a green fluorescent protein homologue. *Proc. Natl. Acad. Sci. U.S.A.* **104**, 6672–6677 (2007).

48. V. V Verkhusha *et al.*, An enhanced mutant of red fluorescent protein DsRed for double labeling and developmental timer of neural fiber bundle formation. *J. Biol. Chem.* **276**, 29621–29624 (2001).

49. B. J. Bevis, B. S. Glick, Rapidly maturing variants of the Discosoma red fluorescent protein (DsRed). *Nat. Biotechnol.* **20**, 83–87 (2002).

50. A. V Terskikh, A. F. Fradkov, A. G. Zaraisky, A. V Kajava, B. Angres, Analysis of DsRed Mutants: Space around the fluorophore accelerates fluorescence development. *J. Biol. Chem.* **277**, 7633–7636 (2002).

51. G. N. Phillips Jr, Structure and dynamics of green fluorescent protein. *Curr. Opin. Struct. Biol.* **7**, 821–827 (1997).

52. D. A. Zacharias, J. D. Violin, A. C. Newton, R. Y. Tsien, Partitioning of lipid-modified monomeric GFPs into membrane microdomains of live cells. *Science*. **296**, 913–916 (2002).

53. W. Zeng *et al.*, Resonance energy transfer between green fluorescent protein variants: complexities revealed with myosin fusion proteins. *Biochemistry*. **45**, 10482–10491 (2006).

54. D. Yarbrough, R. M. Wachter, K. Kallio, M. V Matz, S. J. Remington, Refined crystal structure of DsRed, a red fluorescent protein from coral, at 2.0-Å resolution. *Proc. Natl. Acad. Sci. U.S.A.* **98**, 462–467 (2001).

55. R. E. Campbell *et al.*, A monomeric red fluorescent protein. *Proc. Natl. Acad. Sci. U.S.A.* **99**, 7877–7882 (2002).

56. S. J. Remington *et al.*, zFP538, a yellow-fluorescent protein from Zoanthus, contains a novel three-ring chromophore. *Biochemistry*. **44**, 202–212 (2004).

57. S. Karasawa, T. Araki, T. Nagai, H. Mizuno, A. Miyawaki, Cyan-emitting and orange-emitting fluorescent proteins as a donor/acceptor pair for fluorescence resonance energy transfer. . *Biochem. J.* **381**, 307–312 (2004).

58. A. Kikuchi *et al.*, Structural characterization of a thiazoline-containing chromophore in an orange fluorescent protein, monomeric Kusabira orange. *Biochemistry*. **47**, 11573–11580 (2008).

59. H. Ai, N. C. Shaner, Z. Cheng, R. Y. Tsien, R. E. Campbell, Exploration of new chromophore structures leads to the identification of improved blue fluorescent proteins. *Biochemistry*. **46**, 5904–5910 (2007).

60. L. Wang, W. C. Jackson, P. A. Steinbach, R. Y. Tsien, Evolution of new nonantibody proteins via iterative somatic hypermutation. *Proc. Natl. Acad. Sci. U.S.A.* **101**, 16745–16749 (2004).

61. P. Abbyad, W. Childs, X. Shi, S. G. Boxer, Dynamic Stokes shift in green fluorescent protein variants. *Proc. Natl. Acad. Sci. U.S.A.* **104**, 20189–20194 (2007).

62. T. Kogure *et al.*, A fluorescent variant of a protein from the stony coral Montipora facilitates dual-color single-laser fluorescence cross-correlation spectroscopy. *Nat. Biotechnol.* **24**, 577–581 (2006).

63. J. N. Henderson *et al.*, Excited state proton transfer in the red fluorescent protein mKeima. *J. Am. Chem. Soc.* **131**, 13212–13213 (2009).

64. D. Razansky *et al.*, Multispectral opto-acoustic tomography of deep-seated fluorescent proteins in vivo. *Nature Photon.* **3**, 412–417 (2009).

65. S. Ganesan, S. M. Ameer-beg, T. T. C. Ng, B. Vojnovic, F. S. Wouters, A dark yellow fluorescent protein (YFP)-based Resonance Energy-Accepting Chromoprotein (REACh) for Förster resonance energy transfer with GFP. *Proc. Natl. Acad. Sci. U.S.A.* **103**, 4089–4094 (2006).

66. A. Pettikiriarachchi, L. Gong, M. A. Perugini, R. J. Devenish, M. Prescott, Ultramarine, a chromoprotein acceptor for Förster resonance energy transfer. *PLoS One*. **7**, e41028 (2012).

67. R. Ando, H. Mizuno, A. Miyawaki, Regulated fast nucleocytoplasmic shuttling observed by reversible protein highlighting. *Science*. **306**, 1370–1373 (2004).

68. X. X. Zhou, H. K. Chung, A. J. Lam, M. Z. Lin, Optical control of protein activity by fluorescent protein domains. *Science*. **338**, 810–814 (2012).

69. G. Patterson, M. Davidson, S. Manley, J. Lippincott-Schwartz, Superresolution imaging using single-molecule localization. *Annu. Rev. Phys. Chem.* **61**, 345–367 (2010).

70. G. H. Patterson, J. Lippincott-Schwartz, A photoactivatable GFP for selective photolabeling of proteins and cells. *Science*. **297**, 1873–1877 (2002).

71. R. E. Campbell, Fluorescent-protein-based biosensors: modulation of energy transfer as a design principle. *Anal. Chem.* **81**, 5972–5979 (2009).

72. D. V Lim, J. M. Simpson, E. A. Kearns, M. F. Kramer, Current and developing technologies for monitoring agents of bioterrorism and biowarfare. *Clin. Microbiol. Rev.* **18**, 583–607 (2005).

73. B. Valeur, M. N. Berberan-Santos, in *Molecular Fluorescence: Principles and Applications* (Wiley-VCH, 2012), pp. 213–261.

74. A. Miyawaki, O. Griesbeck, R. Heim, R. Y. Tsien, Dynamic and quantitative Ca^{2+} measurements using improved cameleons. *Proc. Natl. Acad. Sci. U.S.A.* **96**, 2135–2140 (1999).

75. M. T. Kunkel, Q. Ni, R. Y. Tsien, J. Zhang, A. C. Newton, Spatio-temporal dynamics of protein kinase B/Akt signaling revealed by a genetically encoded fluorescent reporter. *J. Biol. Chem.* **280**, 5581–5587 (2005).

76. J. Zhang, Y. Ma, S. S. Taylor, R. Y. Tsien, Genetically encoded reporters of protein kinase A activity reveal impact of substrate tethering. *Proc. Natl. Acad. Sci. U.S.A.* **98**, 14997–15002 (2001).

77. J. Zhang, C. J. Hupfeld, S. S. Taylor, J. M. Olefsky, R. Y. Tsien, Insulin disrupts beta-adrenergic signalling to protein kinase A in adipocytes. *Nature*. **437**, 569–573 (2005).

78. M. D. Allen, J. Zhang, Subcellular dynamics of protein kinase A activity visualized by FRET-based reporters. *Biochem. Biophys. Res. Commun.* **348**, 716–721 (2006).

79. Y. Wang *et al.*, Visualizing the mechanical activation of Src. *Nature*. **434**, 1040–1045 (2005).

80. K. Aoki, M. Matsuda, Visualization of small GTPase activity with fluorescence resonance energy transfer-based biosensors. *Nat. Protoc.* **4**, 1623–1631 (2009).

81. R. Heim, R. Tsien, Engineering green fluorescent protein for improved brightness, longer wavelengths and fluorescence resonance energy transfer. *Curr. Biol.* **6**, 178–182 (1996).

82. H. Ai, K. L. Hazelwood, M. W. Davidson, R. E. Campbell, Fluorescent protein FRET pairs for ratiometric imaging of dual biosensors. *Nat. Methods*. **5**, 401–403 (2008).

83. Y.-C. Hwang, J. J.-H. Chu, P. L. Yang, W. Chen, M. V Yates, Rapid identification of inhibitors that interfere with poliovirus replication using a cell-based assay. *Antiviral Res.* **77**, 232–236 (2008).

84. A. W. Nguyen, P. S. Daugherty, Evolutionary optimization of fluorescent proteins for intracellular FRET. *Nat. Biotechnol.* **23**, 355–360 (2005).

85. D. Sinnecker, P. Voigt, N. Hellwig, M. Schaefer, Reversible photobleaching of enhanced green fluorescent proteins. *Biochemistry*. **44**, 7085–7094 (2005).

86. N. C. Shaner *et al.*, Improving the photostability of bright monomeric orange and red fluorescent proteins. *Nat. Methods*. **5**, 545–551 (2008).

87. D. F. Reiff *et al.*, In vivo performance of genetically encoded indicators of neural activity in flies. *J. Neurosci.* **25**, 4766–4778 (2005).

88. M. K. Raarup *et al.*, Enhanced yellow fluorescent protein photoconversion to a cyan fluorescent protein-like species is sensitive to thermal and diffusion conditions. *J. Biomed. Opt.* **14**, 34012–34039 (2009).

89. R. Dixit, R. Cyr, Cell damage and reactive oxygen species production induced by fluorescence microscopy: effect on mitosis and guidelines for non-invasive fluorescence microscopy. *Plant J.* **36**, 280–290 (2003).

90. P. E. Hockberger *et al.*, Activation of flavin-containing oxidases underlies light-induced production of H_2O_2 in mammalian cells. *Proc. Natl. Acad. Sci. U.S.A.* **96**, 6255–6260 (1999).

91. A. J. Lam *et al.*, Improving FRET dynamic range with bright green and red fluorescent proteins. *Nat. Methods*. **9**, 1005–1012 (2012).

92. S. Tang *et al.*, Design and application of a class of sensors to monitor Ca^{2+} dynamics in high Ca^{2+} concentration cellular compartments. *Proc. Natl. Acad. Sci. U.S.A.* **108**, 16265–16270 (2011).

93. H. Østergaard, A. Henriksen, F. G. Hansen, J. R. Winther, Shedding light on disulfide bond formation: engineering a redox switch in green fluorescent protein. *EMBO J.* **20**, 5853–5862 (2001).

94. G. T. Hanson *et al.*, Investigating mitochondrial redox potential with redox-sensitive green fluorescent protein indicators. *J. Biol. Chem.* **279**, 13044–13053 (2004).

95. J. Akerboom *et al.*, Crystal structures of the GCaMP calcium sensor reveal the mechanism of fluorescence signal change and aid rational design. *J. Biol. Chem.* **284**, 6455–6464 (2009).

96. Q. Wang, B. Shui, M. I. Kotlikoff, H. Sondermann, Structural basis for calcium sensing by GCaMP2. *Structure*. **16**, 1817–1827 (2008).

97. I. Ghosh, A. D. Hamilton, L. Regan, Antiparallel leucine zipper-firected protein reassembly: application to the green fluorescent protein. *J. Am. Chem. Soc.* **122**, 5658–5659 (2000).

98. Y. J. Shyu, C.-D. Hu, Fluorescence complementation: an emerging tool for biological research. *Trends Biotechnol.* **26**, 622–630 (2014).

99. J. Chu *et al.*, A novel far-red bimolecular fluorescence complementation system that allows for efficient visualization of protein interactions under physiological conditions. *Biosens. Bioelectron.* **25**, 234–239 (2009).

100. C. G. M. Wilson, T. J. Magliery, L. Regan, Detecting protein-protein interactions with GFP-fragment reassembly. *Nat. Methods*. **1**, 255–262 (2004).

101. I. Remy, S. W. Michnick, Regulation of apoptosis by the Ft1 protein, a new modulator of protein kinase B/Akt. *Mol. Cell. Biol.* **24**, 1493–1504 (2004).

102. Z. Ding *et al.*, A retrovirus-based protein complementation assay screen reveals functional AKT1-binding partners. *Proc. Natl. Acad. Sci. U.S.A.* **103**, 15014–15019 (2006).

103. I. Remy, S. W. Michnick, A cDNA library functional screening strategy based on fluorescent protein complementation assays to identify novel components of signaling pathways. *Methods*. **32**, 381–388 (2004).

104. T. Kojima, S. Karasawa, A. Miyawaki, T. Tsumuraya, I. Fujii, Novel screening system for protein–protein interactions by bimolecular fluorescence complementation in Saccharomyces cerevisiae. *J. Biosci. Bioeng.* **111**, 397–401 (2011).

105. M. Morell, A. Espargaro, F. X. Aviles, S. Ventura, Study and selection of in vivo protein interactions by coupling bimolecular fluorescence complementation and flow cytometry. *Nat. Protoc.* **3**, 22–33 (2008).

106. J. E. Grotzke, Q. Lu, P. Cresswell, Deglycosylation-dependent fluorescent proteins provide unique tools for the study of ER-associated degradation. *Proc. Natl. Acad. Sci. U.S.A.* **110**, 3393–8 (2013).

107. M. Z. Lin, J. S. Glenn, R. Y. Tsien, A drug-controllable tag for visualizing newly synthesized proteins in cells and whole animals. *Proc. Natl. Acad. Sci. U.S.A.* **105**, 7744–7749 (2008).

108. M. T. Butko *et al.*, Fluorescent and photo-oxidizing TimeSTAMP tags track protein fates in light and electron microscopy. *Nat. Neurosci.* **15**, 1742–1751 (2012).

109. S. C. Alford, A. S. Abdelfattah, Y. Ding, R. E. Campbell, A fluorogenic red fluorescent protein heterodimer. *Chem. Biol.* **19**, 353–60 (2012).

110. S. C. Alford, Y. Ding, T. Simmen, R. E. Campbell, Dimerization-dependent green and yellow fluorescent proteins. *ACS Synth. Biol.* **1**, 569–575 (2012).

111. B. I. Dahiyat, S. L. Mayo, De novo protein design: fully automated sequence selection. *Science*. **278**, 82–87 (1997).

112. B. Kuhlman *et al.*, Design of a novel globular protein fold with atomic-level accuracy. *Science*. **302**, 1364–1368 (2003).

113. J. Reina *et al.*, Computer-aided design of a PDZ domain to recognize new target sequences. *Nat. Struct. Mol. Biol.* **9**, 621–627 (2002).

114. D. Rothlisberger *et al.*, Kemp elimination catalysts by computational enzyme design. *Nature*. **453**, 190–195 (2008).

115. J. B. Siegel *et al.*, Computational design of an enzyme catalyst for a stereoselective bimolecular Diels-Alder reaction. *Science*. **329**, 309–313 (2010).

116. L. Jiang *et al.*, De novo computational design of Retro-Aldol enzymes. *Science*. **319**, 1387–1391 (2008).

117. L. Yuan, I. Kurek, J. English, R. Keenan, Laboratory-directed protein evolution. *Microbiol. Mol. Biol. Rev.* **69**, 373–392 (2005).

118. J. H. Campbell, J. A. Lengyel, J. Langridge, Evolution of a second gene for β-galactosidase in Escherichia coli. *Proc. Natl. Acad. Sci. U.S.A.* **70**, 1841–1845 (1973).

119. J. D. Bloom, F. H. Arnold, In the light of directed evolution: pathways of adaptive protein evolution. *Proc. Natl. Acad. Sci. U.S.A.* **106**, 9995–10000 (2009).

120. D. A. Estell, T. P. Graycar, J. A. Wells, Engineering an enzyme by site-directed mutagenesis to be resistant to chemical oxidation. *J. Biol. Chem.* **260** , 6518–6521 (1985).

121. C. von der Osten *et al.*, Protein engineering of subtilisins to improve stability in detergent formulations. *J. Biotechnol.* **28**, 55–68 (1993).

122. F. J. Ghadessy, J. L. Ong, P. Holliger, Directed evolution of polymerase function by compartmentalized self-replication. *Proc. Natl. Acad. Sci. U.S.A.* **98**, 4552–4557 (2001).

123. C. R. Sclimenti, B. Thyagarajan, M. P. Calos, Directed evolution of a recombinase for improved genomic integration at a native human sequence. *Nucleic Acids Res.* **29**, 5044–5051 (2001).

124. K. Murashima, A. Kosugi, R. H. Doi, Thermostabilization of cellulosomal endoglucanase EngB from Clostridium cellulovorans by in vitro DNA recombination with non-cellulosomal endoglucanase EngD. *Mol. Microbiol.* **45**, 617–626 (2002).

125. H. Ai, J. N. Henderson, S. J. Remington, R. E. Campbell, Directed evolution of a monomeric, bright and photostable version of Clavularia cyan fluorescent protein: structural characterization and applications in fluorescence imaging. *Biochem. J.* **400**, 531–540 (2006).

126. R. N. Day, M. W. Davidson, The fluorescent protein palette: tools for cellular imaging. *Chem. Soc. Rev.* **38**, 2887–2921 (2009).

127. C. A. Hutchison *et al.*, Mutagenesis at a specific position in a DNA sequence. *J. Biol. Chem.* **253**, 6551–6560 (1978).

128. P. Cirino, K. Mayer, D. Umeno, in *Directed Evolution Library Creation (Arnold, F. H., and Georgiou, G., Eds.)* (Humana Press, Totowa, New Jersey, 2003), pp. 3–9.

129. R. A. Beckman, A. S. Mildvan, L. A. Loeb, On the fidelity of DNA replication: manganese mutagenesis in vitro. *Biochemistry*. **24**, 5810–5817 (1985).

130. T. A. Kunkel, L. A. Loeb, On the fidelity of DNA replication. Effect of divalent metal ion activators and deoxyrionucleoside triphosphate pools on in vitro mutagenesis. *J. Biol. Chem.* **254**, 5718–5725 (1979).

131. M. Zaccolo, E. Gherardi, The effect of high-frequency random mutagenesis on in vitro protein evolution: a study on TEM-1 β-lactamase. *J. Mol. Biol.* **285**, 775–783 (1999).

132. D. A. Drummond, B. L. Iverson, G. Georgiou, F. H. Arnold, Why high-error-rate random mutagenesis libraries are enriched in functional and improved proteins. *J. Mol. Biol.* **350**, 806–816 (2005).

133. W. P. C. Stemmer, Rapid evolution of a protein in vitro by DNA shuffling. *Nature*. **370**, 389–391 (1994).

134. H. Zhao, L. Giver, Z. Shao, J. A. Affholter, F. H. Arnold, Molecular evolution by staggered extension process (StEP) in vitro recombination. *Nat. Biotechnol.* **16**, 258–261 (1998).

135. A. Crameri, S.-A. Raillard, E. Bermudez, W. P. C. Stemmer, DNA shuffling of a family of genes from diverse species accelerates directed evolution. *Nature*. **391**, 288–291 (1998).

136. S. Chapman *et al.*, The photoreversible fluorescent protein iLOV outperforms GFP as a reporter of plant virus infection. *Proc. Natl. Acad. Sci. U.S.A.* **105**, 20038–20043 (2008).

137. W. P. Stemmer, DNA shuffling by random fragmentation and reassembly: in vitro recombination for molecular evolution. *Proc. Natl. Acad. Sci. U.S.A.* **91**, 10747–10751 (1994).

138. Z. Shao, H. Zhao, L. Giver, F. H. Arnold, Random-priming in vitro recombination: an effective tool for directed evolution. *Nucleic Acids Res.* **26**, 681–683 (1998).

139. H. Zhao, F. H. Arnold, Combinatorial protein design: strategies for screening protein libraries. *Curr. Opin. Struct. Biol.* **7**, 480–485 (1997).

140. H. Lin, V. W. Cornish, Screening and selection methods for large-scale analysis of protein function. *Angew. Chemie Int. Ed.* **41**, 4402–4425 (2002).

141. M. I. Kotlikoff, Genetically encoded Ca^{2+} indicators: using genetics and molecular design to understand complex physiology. *J. Physiol.* **578**, 55–67 (2007).

142. C. Grienberger, A. Konnerth, Imaging calcium in neurons. *Neuron*. **73**, 862–85 (2012).

143. C. M. L. Barrett, N. Ray, J. D. Thomas, C. Robinson, A. Bolhuis, Quantitative export of a reporter protein, GFP, by the twin-arginine translocation pathway in Escherichia coli. *Biochem. Biophys. Res. Commun.* **304**, 279–284 (2003).

144. Y. Zhao *et al.*, An expanded palette of genetically encoded Ca^{2+} indicators. *Science*. **333**, 1888–1891 (2011).

145. J. Akerboom *et al.*, Optimization of a GCaMP calcium indicator for neural activity imaging. *J. Neurosci.* **32**, 13819–40 (2012).

146. J. Akerboom *et al.*, Genetically encoded calcium indicators for multi-color neural activity imaging and combination with optogenetics. *Front. Mol. Neurosci.* **6**, 2 (2013).

147. M. D. Resh, Fatty acylation of proteins: new insights into membrane targeting of myristoylated and palmitoylated proteins. *Biochim. Biophys. Acta*. **1451**, 1–16 (1999).

148. A. Berndt *et al.*, High-efficiency channelrhodopsins for fast neuronal stimulation at low light levels. *Proc. Natl. Acad. Sci. U.S.A.* **108**, 7595–7600 (2011).

149. T. S. Vihtelic, C. J. Doro, D. R. Hyde, Cloning and characterization of six zebrafish photoreceptor opsin cDNAs and immunolocalization of their corresponding proteins. *Vis. Neurosci.* **16**, 571–585 (1999).

150. M. Ohkura, T. Sasaki, C. Kobayashi, Y. Ikegaya, J. Nakai, An improved genetically encoded red fluorescent Ca^{2+} indicator for detecting optically evoked action potentials. *PLoS One*. **7**, e39933 (2012).

151. G. Jung, S. Mais, A. Zumbusch, C. Bräuchle, The role of dark states in the photodynamics of the green fluorescent protein examined with two-color fluorescence excitation spectroscopy. *J. Phys. Chem. A*. **104**, 873–877 (2000).

152. M. Andresen *et al.*, Structural basis for reversible photoswitching in Dronpa. *Proc. Natl. Acad. Sci. U.S.A.* **104**, 13005–13009 (2007).

153. V. Adam *et al.*, Structural characterization of IrisFP, an optical highlighter undergoing multiple photo-induced transformations. *Proc. Natl. Acad. Sci. U.S.A.* **105**, 18343–18348 (2008).

154. X. Shu, N. C. Shaner, C. A. Yarbrough, R. Y. Tsien, S. J. Remington, Novel chromophores and buried charges control color in mFruits. *Biochemistry*. **45**, 9639–9647 (2006).

155. Z. Cheng, R. E. Campbell, Assessing the structural stability of designed β-hairpin peptides in the cytoplasm of live cells. *ChemBioChem*. **7**, 1147–1150 (2006).

156. N. S. Makarov, M. Drobizhev, A. Rebane, Two-photon absorption standards in the 550-1600 nmexcitation wavelength range. *Opt. Express*. **16**, 4029–4047 (2008).

157. S. Minobe *et al.*, Rac is involved in the interkinetic nuclear migration of cortical progenitor cells. *Neurosci. Res.* **63**, 294–301 (2009).

158. B. R. Conklin, Z. Farfel, K. D. Lustig, D. Julius, H. R. Bourne, Substitution of three amino acids switches receptor specificity of Gq alpha to that of Gi alpha. *Nature*. **363**, 274–276 (1993).

159. T. Saito, N. Nakatsuji, Efficient gene transfer into the embryonic mouse brain using in vivo electroporation. *Dev. Biol.* **240**, 237–246 (2001).

160. H. Tabata, K. Nakajima, Labeling embryonic mouse central nervous system cells by in utero electroporation. *Dev. Growth Differ.* **50**, 507–511 (2008).

161. T. Miyata, A. Kawaguchi, H. Okano, M. Ogawa, Asymmetric inheritance of radial glial fibers by cortical neurons. *Neuron*. **31**, 727–741 (2001).

162. J. Wu *et al.*, Improved orange and red Ca^{2+} indicators and photophysical considerations for optogenetic applications. *ACS Chem. Neurosci.* **4**, 963–972 (2013).

163. A. S. Walker, J. Burrone, M. P. Meyer, Functional imaging in the zebrafish retinotectal system using RGECO. *Front. Neural Circuits*. **7**, 34 (2013).

164. U. Pech *et al.*, Mushroom body miscellanea: transgenic Drosophila strains expressing anatomical and physiological sensor proteins in Kenyon cells. *Front. Neural Circuits*. **7**, 147 (2013).

165. H. Li, Y. Li, Z. Lei, K. Wang, A. Guo, Transformation of odor selectivity from projection neurons to single mushroom body neurons mapped with dual-color calcium imaging. *Proc. Natl. Acad. Sci. U.S.A.* **110**, 12084–12089 (2013).

166. I. Benjumeda *et al.*, Uncoupling of EphA/ephrinA signaling and spontaneous activity in neural circuit wiring. *J. Neurosci.* **33**, 18208–18218 (2013).

167. K. A. Schenkman, D. R. Marble, E. O. Feigl, D. H. Burns, Near-infrared spectroscopic measurement of myoglobin oxygen saturation in the presence of hemoglobin using partial least-squares analysis. *Appl. Spectrosc.* **53**, 325–331 (1999).

168. B. J. Tromberg *et al.*, Non-invasive in vivo characterization of breast tumors using photon migration spectroscopy. *Neoplasia*. **2**, 26–40 (2000).

169. J. Chu *et al.*, Non-invasive intravital imaging of cellular differentiation with a bright red-excitable fluorescent protein. *Nat. Methods*. **11**, 572–578 (2014).

170. W. Denk, J. H. Strickler, W. W. Webb, Two-photon laser scanning fluorescence microscopy. *Science*. **248**, 73–76 (1990).

171. M. Drobizhev, N. S. Makarov, S. E. Tillo, T. E. Hughes, A. Rebane, Two-photon absorption properties of fluorescent proteins. *Nat. Methods*. **8**, 393–399 (2011).

172. X. Soto *et al.*, Inositol kinase and its product accelerate wound healing by modulating calcium levels, Rho GTPases, and F-actin assembly. *Proc. Natl. Acad. Sci. U.S.A.* **110**, 11029–11034 (2013).

173. B. Enyedi, S. Kala, T. Nikolich-Zugich, P. Niethammer, Tissue damage detection by osmotic surveillance. *Nat. Cell Biol.* **15**, 1123–1130 (2013).

174. I. Llorente-Folch *et al.*, Calcium-regulation of mitochondrial respiration maintains ATP homeostasis and requires ARALAR/AGC1-malate aspartate shuttle in intact cortical neurons. *J. Neurosci.* **33**, 13957–13971 (2013).

175. K. D. Piatkevich *et al.*, Monomeric red fluorescent proteins with a large Stokes shift. *Proc. Natl. Acad. Sci. U.S.A.* **107**, 5369–5374 (2010).

176. K. D. Piatkevich, V. N. Malashkevich, S. C. Almo, V. V Verkhusha, Engineering ESPT pathways based on structural analysis of LSSmKate red fluorescent proteins with large Stokes shift. *J. Am. Chem. Soc.* **132**, 10762–10770 (2010).

177. M. Maravall, Z. F. Mainen, B. L. Sabatini, K. Svoboda, Estimating intracellular calcium concentrations and buffering without wavelength ratioing. *Biophys. J.* **78**, 2655–2667 (2000).

178. C. P. J. Glover, A. S. Bienemann, D. J. Heywood, A. S. Cosgrave, J. B. Uney, Adenoviral-mediated, high-level, cell-specific transgene expression: a SYN1-WPRE cassette mediates increased transgene expression with no loss of neuron specificity. *Mol. Ther.* **5**, 509–516 (2002).

179. S. Kugler, E. Kilic, M. Bahr, Human synapsin 1 gene promoter confers highly neuron-specific long-term transgene expression from an adenoviral vector in the adult rat brain depending on the transduced area. *Gene Ther.* **10**, 337–347 (2003).

180. J. N. Betley, S. M. Sternson, Adeno-associated viral vectors for mapping, monitoring, and manipulating neural circuits. *Hum. Gene Ther.* **22**, 669–677 (2011).

181. S. Thümmler, T. V Dunwiddie, Adenosine receptor antagonists induce persistent bursting in the rat hippocampal CA3 region via an NMDA receptor-dependent mechanism. *J. Neurophysiol.* **83**, 1787–1795 (2000).

182. B. Panaitescu *et al.*, Methylxanthines do not affect rhythmogenic preBotC inspiratory network activity but impair bursting of preBotC-driven motoneurons. *Neuroscience*. **255**, 158–176 (2013).

183. A. Klishin, T. Tsintsadze, N. Lozovaya, O. Krishtal, Latent N-methyl-D-aspartate receptors in the recurrent excitatory pathway between hippocampal CA1 pyramidal neurons: Ca^{2+}-dependent activation by blocking A1 adenosine receptors. *Proc. Natl. Acad. Sci. U.S.A.* **92**, 12431–12435 (1995).

184. J. M. Brundege, T. V Dunwiddie, Modulation of excitatory synaptic transmission by adenosine released from single hippocampal pyramidal neurons. *J. Neurosci.* **16**, 5603–5612 (1996).

185. T. Sugimoto, M. Sugimoto, I. Uchida, T. Mashimo, S. Okada, Inhibitory effect of theophylline on recombinant GABA(A) receptor. *Neuroreport*. **12**, 489–493 (2001).

186. T.-W. Chen *et al.*, Ultrasensitive fluorescent proteins for imaging neuronal activity. *Nature*. **499**, 295–300 (2013).

187. C. Grienberger *et al.*, Sound-evoked network calcium transients in mouse auditory cortex in vivo. *J. Physiol.* **590**, 899–918 (2011).

188. O. Garaschuk, R.-I. Milos, A. Konnerth, Targeted bulk-loading of fluorescent indicators for two-photon brain imaging in vivo. *Nat. Protoc.* **1**, 380–386 (2006).

189. M. K. Shelton, K. D. McCarthy, Mature hippocampal astrocytes exhibit functional metabotropic and ionotropic glutamate receptors in situ. *Glia*. **26**, 1–11 (1999).

190. G. Carmignoto, L. Pasti, T. Pozzan, On the role of voltage-dependent calcium channels in calcium signaling of astrocytes in situ. *J. Neurosci.* **18**, 4637–4645 (1998).

191. L. Pasti, A. Volterra, T. Pozzan, G. Carmignoto, Intracellular calcium oscillations in astrocytes: a highly plastic, bidirectional form of communication between neurons and astrocytes in situ. *J. Neurosci.* **17**, 7817–7830 (1997).

192. M. E. Harris-White, S. A. Zanotti, S. A. Frautschy, A. C. Charles, Spiral intercellular calcium waves in hippocampal slice cultures. *J. Neurophysiol.* **79**, 1045–1052 (1998).

193. L. Venance, N. Stella, J. Glowinski, C. Giaume, Mechanism involved in initiation and propagation of receptor-induced intercellular calcium signaling in cultured rat astrocytes. *J. Neurosci.* **17**, 1981–1992 (1997).

194. I. Latour, C. E. Gee, R. Robitaille, J.-C. Lacaille, Differential mechanisms of Ca^{2+} responses in glial cells evoked by exogenous and endogenous glutamate in rat hippocampus. *Hippocampus*. **11**, 132–145 (2001).

195. M. Megías, Z. Emri, T. F. Freund, A. I. Gulyás, Total number and distribution of inhibitory and excitatory synapses on hippocampal CA1 pyramidal cells. *Neuroscience*. **102**, 527–540 (2001).

196. M. Clark, M. S. Dar, Release of endogenous glutamate from rat cerebellar synaptosomes: interactions with adenosine and ethanol. *Life Sci.* **44**, 1625–1635 (1989).

197. P. D. Nieuwkoop, J. Faber, in *Normal table of Xenopus laevis (Daudin)* (North-Holland, Amsterdam, 1956), pp. 164–188.

198. E. S. Ruthazer *et al.*, Bulk Electroporation of Retinal Ganglion Cells in Live Xenopus Tadpoles. *Cold Spring Harb. Protoc.* **8**, 771–775 (2013).

199. M. J. Berridge, P. Lipp, M. D. Bootman, The versatility and universality of calcium signalling. *Nat. Rev. Mol. Cell Biol.* **1**, 11–21 (2000).

200. H. Hoi, T. Matsuda, T. Nagai, R. E. Campbell, Highlightable Ca^{2+} indicators for live cell imaging. *J. Am. Chem. Soc.* **135**, 46–49 (2012).

201. H. J. Carlson, R. E. Campbell, Circular permutated red fluorescent proteins and calcium ion indicators based on mCherry. *Protein Eng. Des. Sel.* **26**, 763–772 (2013).

202. K. Horikawa *et al.*, Spontaneous network activity visualized by ultrasensitive Ca^{2+} indicators, yellow Cameleon-Nano. *Nat. Methods*. **7**, 729–732 (2010).

203. A. E. Palmer, C. Jin, J. C. Reed, R. Y. Tsien, Bcl-2-mediated alterations in endoplasmic reticulum Ca^{2+} analyzed with an improved genetically encoded fluorescent sensor. *Proc. Natl. Acad. Sci. U.S.A.* **101**, 17404–17409 (2004).

204. A. E. Palmer *et al.*, Ca^{2+} indicators based on computationally redesigned calmodulin-peptide pairs. *Chem. Biol.* **13**, 521–530 (2006).

205. A. E. Palmer, R. Y. Tsien, Measuring calcium signaling using genetically targetable fluorescent indicators. *Nat. Protoc.* **1**, 1057–1065 (2006).

206. R. Rudolf, P. J. Magalhães, T. Pozzan, Direct in vivo monitoring of sarcoplasmic reticulum Ca^{2+} and cytosolic cAMP dynamics in mouse skeletal muscle. *J. Cell Biol.* **173**, 187–93 (2006).

207. E. a Sobie, W. J. Lederer, Dynamic local changes in sarcoplasmic reticulum calcium: physiological and pathophysiological roles. *J. Mol. Cell. Cardiol.* **52**, 304–311 (2012).

208. D. Burdakov, O. H. Petersen, A. Verkhratsky, Intraluminal calcium as a primary regulator of endoplasmic reticulum function. *Cell Calcium*. **38**, 303–310 (2005).

209. N. Demaurex, C. Distelhorst, Apoptosis--the Calcium Connection. *Science*. **300**, 65–67 (2003).

210. S. Arnaudeau, W. L. Kelley, J. V Walsh, N. Demaurex, Mitochondria recycle Ca^{2+} to the endoplasmic reticulum and prevent the depletion of neighboring endoplasmic reticulum regions. *J. Biol. Chem.* **276**, 29430–29439 (2001).

211. G. Csordás *et al.*, Imaging interorganelle contacts and local calcium dynamics at the ER-mitochondrial interface. *Mol. Cell*. **39**, 121–32 (2010).

212. L. Fliegel, K. Burns, D. H. MacLennan, R. A. Reithmeier, M. Michalak, Molecular cloning of the high affinity calcium-binding protein (calreticulin) of skeletal muscle sarcoplasmic reticulum. *J. Biol. Chem.* **264**, 21522–21528 (1989).

213. J. M. Kendall, R. L. Dormer, A. K. Campbell, Targeting aequorin to the endoplasmic reticulum of living cells. *Biochem. Biophys. Res. Commun.* **189**, 1008–1016 (1992).

214. M. T. Hasan *et al.*, Functional fluorescent Ca^{2+} indicator proteins in transgenic mice under TET control. *PLoS Biol.* **2**, e163 (2004).

215. N. Heim, O. Griesbeck, Genetically encoded indicators of cellular calcium dynamics based on Troponin C and green fluorescent protein. *J. Biol. Chem.* **279**, 14280–14286 (2004).

216. X. R. Sun *et al.*, Fast GCaMPs for improved tracking of neuronal activity. *Nat. Commun.* **4**, 2170 (2013).

217. L. Tian *et al.*, Imaging neural activity in worms, flies and mice with improved GCaMP calcium indicators. *Nat. Methods*. **6**, 875–881 (2009).

218. S. A. Thayer, Y. M. Usachev, W. J. Pottorf, Modulating Ca^{2+} clearance from neurons. *Front. Biosci.* **7**, d1255–79 (2002).

219. S. Marchi, P. Pinton, The mitochondrial calcium uniporter complex: molecular components, structure and physiopathological implications. *J. Physiol.* **592**, 829–839 (2014).

220. M. P. Mattson, M. Gleichmann, A. Cheng, Mitochondria in neuroplasticity and neurological disorders. *Neuron*. **60**, 748–766 (2008).

221. D. G. Nicholls, S. L. Budd, Mitochondria and neuronal survival. *Physiol. Rev.* **80**, 315–360 (2000).

222. D. D. Friel, Mitochondria as regulators of stimulus-evoked calcium signals in neurons. *Cell Calcium*. **28**, 307–316 (2000).

223. J. D. Ulrich *et al.*, Distinct activation properties of the nuclear factor of activated T-cells (NFAT) isoforms NFATc3 and NFATc4 in neurons. *J. Biol. Chem.* **287**, 37594–37609 (2012).

224. K. Schnizler *et al.*, Protein kinase A anchoring via AKAP150 is essential for TRPV1 modulation by forskolin and prostaglandin E2 in mouse sensory neurons. *J. Neurosci.* **28**, 4904–4917 (2008).

225. B. S. Meldrum, Glutamate as a neurotransmitter in the brain: review of physiology and pathology. *J. Nutr.* **130**, 1007–1015 (2000).

226. R. M. De Lorimier *et al.*, Construction of a fluorescent biosensor family. *Protein Sci.* **11**, 2655–2675 (2002).

227. B. D. Bennett *et al.*, Absolute metabolite concentrations and implied enzyme active site occupancy in Escherichia coli. *Nat. Chem. Biol.* **5**, 593–599 (2009).

228. D. Yu *et al.*, An improved monomeric infrared fluorescent protein for neuronal and tumour brain imaging. *Nat. Commun.* **5**, 3626 (2014).

229. D. M. Shcherbakova, V. V Verkhusha, Near-infrared fluorescent proteins for multicolor in vivo imaging. *Nat. Methods*. **10**, 751–754 (2013).